Finite Element Analysis of Fretting Wear

Eindige-elementenanalyse van frettingslijtage

Tongyan Yue

Promotor: prof. dr. ir. M. Abdel Wahab
Proefschrift ingediend tot het behalen van de graad van
Doctor in de ingenieurswetenschappen: werktuigkunde-elektrotechniek

UNIVERSITEIT
GENT

Vakgroep Elektrische Energie, Systemen en Automatisering
Voorzitter: prof. dr. ir. L. Dupré
Faculteit Ingenieurswetenschappen en Architectuur
Academiejaar 2016 - 2017

ISBN 978-90-8578-940-6
NUR 978
Wettelijk depot: D/2016/10.500/72

Promoter

Prof. dr. ir. Magd Abdel Wahab, Ghent University, Belgium

Examination Committee

Prof. Rik Van de Walle (chair)	Ghent University, Belgium
Prof. Joris Degrieck	Ghent University, Belgium
Dr. Jacob Sukumaran	Ghent University, Belgium
Dr. Phuc Phung Van	Ton Duc Thang University, Vietnam
Prof. Timon Rabczuk	Bauhaus University Weimar, Germany

Research Institute

Laboratory Soete
Department of Electrical Energy, Systems and Automation
Faculty of Engineering and Architecture
Ghent University

Technologiepark 903
B-9052 Zwijnaarde
Belgium

Email: tongyan.yue@UGent.be, yuetongyan@gmail.com
http://www.soetelaboratory.ugent.be

Acknowledgements

Firstly, I would like to express my great appreciation to my supervisor Prof. Magd Abdel Wahab, Soete Laboratory, Ghent University, for accepting me as his PhD student and continuously helping me on the related research. I could not finish my PhD work without his patient guidance and generous support.

I would also like to thank China Scholarship Council (CSC) for its final support on this work. This work is funded by CSC No. 201206150077.

This work combines finite element (FE) technique and tribology, which would not have been easier without the help of my colleagues. I would like to express my sincere gratitude to members of finite element research group: Reza Hojjati Talemi, Chen Xin, Phuc Phung Van, Tran Vinh Loc, Ni Junyan and Nadeem Ali Bhatti. I could not forget the constructive suggestions and feedback in both group meetings and general discussions. Thanks for Jacob Sukumaran and Saosometh Chhith, for sharing their professional knowledge on experiments of wear and fretting fatigue.

It has been fortunate for me to have lovely girls near my work: Hanan Alali, Kyvia Pereira and Kannaki Pondicherry. The walking time and lunch time we spent are really effective way to release the pressure of work, which makes life much easier. My special thanks go to Hanan Alali, for always accompany with me from the first day I arrived in Ghent. Her perseverance, diligence and endeavour inspirit me during my PhD life, and will encourage me in the future.

I appreciate the friendly atmosphere of Soete Laboratory created by nice colleagues: Georgette D'Hondt, Diego Belato Rosado, Jules Bossert, Timothy Galle, Nahuel Micone, Kaveh Samadian, Koen Van Minnebruggen, Zhang Jie, Stijn Hertelé, Wouter Ost, Jonathan Vancoillie, Dieter Fauconnier, Sameera Naib, Levente Ferenc Tóth, Yeczain Perez, Vanessa Rodriguez, Matthias Verstraete and Chris Bonne. Special thanks to Jan De Pauw for sharing Belgium tradition and culture with me.

I could not forget the selfless support and company from my friends in Ghent: Sun Yihua, Qu Xiaoxia, Gao Junling; Xu Tao and Li Tao. I really enjoyed the time we spend together in both Ghent and outside. Living abroad far away from home would have been tougher without them.

I would like to express my sincere thanks to Gao Zhen, for his support and patience in the last four years, and also for bringing positive energy in my life.

Finally, I would like to express my deepest gratitude to my parents: Yue Wei and Chen Ying for their endless support and encouragement during my life, which is too much to describe by any languages. This thesis is for my beloved parents.

Yue Tongyan

Ghent, 2016

English summary

Fretting wear is a type of surface damage occurring at contact interfaces due to a micro relative displacement. Owning to this micro displacement, one characteristic of fretting wear phenomenon is that most of the wear debris is trapped in the contact surfaces, and participates the subsequent fretting wear process.

Generally, in fretting wear, the micro slip between contact surfaces is less than 300 μm. Thus, fretting happens when contact surfaces are not supposed to move relative to each other. In practice, it takes place in almost every tribosystem experiencing the oscillatory condition. Fretting wear causes unwanted results such as:

1. The contact between two bodies may become loose, due to the evolution of contact surface profiles that is induced by fretting wear.
2. The relative sliding of two contact bodies may be stuck, since the debris from the contact surfaces may stay in the interfaces.
3. The stress concentration and the micro cracks may occur at the contact surfaces, which may accelerate the failure of the structure.

Particularly, the fretting wear problem of engineering applications, such as the blade/disk, fretted wires, electronic/electrical connectors, and hip joint replacement has been widely studied by worldwide researchers.

As a long-term accumulated surface damage for tens of thousands cycles due to micro displacement, fretting wear is not easy to take parametric study by experimental method. Furthermore, contact stress distributions and the evolution of wear scar are also not very straightforward to measure during experiments. Therefore, Finite Element Method (FEM) technique is employed in this thesis.

In this thesis, FEM of fretting wear based on energy model is developed for simulating and analysing the fretting wear process in the line contact (2 Dimensional) and the point contact (3 Dimensional) configurations. The present study makes several contributions as follows:

1. Firstly, a FE fretting wear model taking into account a variable Coefficient of Friction (CoF) is presented. Two different normal loading conditions are employed. The evolution of CoF as a function of number of cycles is described by the best fitting curve. In order to capture the change of CoF in the running-in stage, the jump cycle used is 100 and increases up to 1000 in the subsequent wear cycles for saving computation time. FE results show that the wear depth, wear width and the peak contact pressure during the running-in stage in the case of variable CoF model are much different from those in the case of constant CoF model. The differences in these variables between the two models decrease with increasing the number of wear cycles. At the final fretting wear cycle, minor difference in wear scar could be found between these two models. Therefore, whether or not choosing variable CoF has little influence of predicting the final wear scar in loading conditions presented in this thesis.
2. Secondly, the mesh sensitivity and singularity problem of fretting wear simulation is evaluated by a method named singularity signature. In this study various loading conditions are implemented, such as applied displacement, CoF and fretting wear cycles. Two types of loading histories are implemented in this study: one is a quarter of the first fretting cycle, and the other is the full fretting cycles, *i.e.* 20,000 cycles. Based on the stress singularity signature, it is found that stress singularity has a close relation with the fretting regime. There is no stress singularity neither in partial slip nor in gross sliding after one fourth of a fretting wear cycle for lower CoF condition. However, stress singularity exits for higher CoF case, in which condition the contact surfaces are almost sticking with each other. After 20,000 cycles, stress singularity exists in the partial slip situation, while there is no stress singularity for gloss sliding condition. Results reveal that more attention should be paid to the mesh size at contact interface of the FE model, when the fretting condition is under partial slip regime.
3. Thirdly, the effects of debris layer on fretting wear process are investigated by the FE model with a debris layer. In this model, the thickness and the Young's modulus of the layer are considered. The debris layer is imported at different time stages during the fretting wear process. Thus, the time stage of importing the debris layer is another parameter in this model, since the thickness of the layer is changing as a function of the number of fretting cycles. The FE results show that Young's modulus of a given thickness debris layer has little influence on the contact pressure distribution, between pad/debris layer and

debris layer/specimen contact surfaces. However, the thickness of a certain debris layer does have an effect on the contact distribution of the contact surface between debris layer/specimen, where fretting wear happens. Increasing the thickness of the debris layer, the maximum contact pressure is reduced and the contact width is increased. After certain number of cycles, the contact pressure distribution changes significantly, *i.e.* the contact pressure at the centre of the contact surface decreases, and increases dramatically at the layer edge due to the stress concentration. Meanwhile, the contact width is also enlarged comparing to the contact width without the debris layer. Furthermore, the time stage of importing debris layer is also a key factor that affects the contact pressure distribution. Thus, the FEA of fretting wear with a debris layer confirms that debris could change the shape and dimensions of wear scar greatly in fretting wear.

4. Finally, the FE fretting wear prediction tool is implemented to a 3D fretted wire model. The fretted wires contact is simplified to a configuration of crossed cylinders with right angle according to the relevant experimental setup. In this study, the influence of the material behaviour, *i.e.* the elastic deformation and elastic-perfectly-plastic deformation, on fretting wear is studied. Firstly, FE results are validated with analytical solution and experimental results. Then, the fretting loops and wear depth after 1000 cycles under different material behaviours are analysed. The results show that under elastic material behaviour, FEM has a good agreement with Hertzian solution. In addition, the wear depth obtained by FEM is close to the experimental one. However, the fretting loop obtained by FE simulation is a typical gross sliding shape in contrast to the experimental findings. For elastic perfectly plastic condition, the shape of fretting loop after 1,000 cycles is the same as that for elastic one, but the dissipated energy is higher. Moreover, the wear depth and wear scar calculated by plasticity are different from the elastic condition.

Nederlandstalige samenvatting

Frettingslijtage is een soort oppervlakteschade op contactpunten als gevolg van relatieve microverplaatsingen. Specifiek aan het frettingslijtagefenomeen is dat, als gevolg van deze microverplaatsingen, het merendeel van het slijtagegruis komt vast te zitten in de contactoppervlakken en zo bijdraagt aan het verdere verloop van het frettingslijtageproces.

In het algemeen is bij frettingslijtage de microslip tussen contactoppervlakken minder dan 300 µm. De wrijving vindt dus plaats wanneer de contactoppervlakken verondersteld worden niet te bewegen ten opzichte van elkaar. In de praktijk vindt het in bijna elk tribosysteem plaats onder oscillerende condities.

Frettingslijtage heeft ongewenste gevolgen, zoals:

1. Het contact tussen twee entiteiten kan losser worden door de evolutie van het contactoppervlakprofiel.
2. De entiteiten kunnen geblokkeerd raken doordat het gruis van het contactoppervlak in het raakvlak vastzit, waardoor ze niet meer kunnen glijden.
3. Er kunnen concentratie van druk en microscheuren plaatsvinden op het contactoppervlak die de uitval van het systeem kunnen versnellen.

Er is wereldwijd al veel onderzoek gedaan naar het probleem van frettingslijtage in verschillende technische applicaties, zoals lemmeten/schijven, fretdraad of kruisdraad, elektronische/elektrische connectoren en vervangingen van heupgewrichten. Frettingslijtage is oppervlakteschade die op lange termijn (tienduizenden cycli) geaccumuleerd wordt, wat betekent dat het veel tijd kost om experimentele studies uit te voeren. Bovendien gebeurt de relatieve verplaatsing tussen de contactoppervlakken op microschaal, wat de metingen in het experiment bemoeilijkt. Ook de verdeling van contactdruk en de evolutie van de slijtage zijn niet gemakkelijk te meten tijdens een experiment. Vandaar dat in deze thesis de eindige-elementenmethode wordt toegepast.

In deze thesis wordt een eindige-elementenmethode voor frettingslijtage ontwikkeld, gebaseerd op het energiemodel. Met deze methode kan het proces van frettingslijtage gesimuleerd en geanalyseerd worden. Het onderzoek levert de volgende bijdragen:

1. Ten eerste wordt een eindige-elementenmodel voor frettingslijtage voorgesteld, dat rekening houdt met een variabele wrijvingscoëfficiënt. Twee verschillende normale beladingsomstandigheden worden toegepast. De evolutie van de wrijvingscoëfficiënt in functie van het aantal cycli wordt beschreven als de meest gepaste curve. Om de veranderingen in wrijvingscoëfficiënt in de inloopfase te meten, zijn de toegepaste jumpcycli 100 en worden die opgedreven naar 1000 in de daaropvolgende slijtagecycli om zo de metingstijd te beperken.

   De eindige-elementenresultaten tonen aan dat de slijtagediepte, de slijtagebreedte en de piek van contactdruk gedurende de inloopfase volledig verschillend zijn bij een model dat een variabele wrijvingscoëfficiënt gebruikt dan bij een model dat een constante wrijvingscoëfficiënt gebruikt. De verschillen in deze variabelen tussen de twee modellen verkleinen wanneer het aantal wrijvingscycli opgedreven wordt. Bij de laatste wrijvingscyclus waren er slechts heel kleine verschillen in slijtageschade tussen deze twee modellen. Dit betekent dat de keuze voor een al dan niet variabele wrijvingscoëfficiënt weinig invloed heeft op het voorspellen van de uiteindelijke slijtageschade in de beladingsomstandigheden onderzocht in deze thesis.

2. Ten tweede wordt een eindige-elementenmodel ontwikkeld om de singulariteit van de belasting te bestuderen bij contact, op basis van verschillende variabelen, zoals toegepaste verplaatsing, wrijvingscoëfficiënt, en frettingslijtagecycli. Twee types beladingsgeschiedenis worden geïmplementeerd in dit onderzoek: bij de ene gaat het om een kwart van de eerste wrijvingscycli, en bij de andere gaat het om de volledige wrijvingscycli, namelijk 20.000 cycli. Vertrekkend vanuit een signatuurmethode van belastingsingulariteit wordt ontdekt dat deze singulariteit nauw verbonden is met het wrijvingsregime. Er is, noch bij gedeeltelijk schuiven, noch bij grof glijden, belastingsingulariteit na één vierde van een wrijvingscyclus bij een lagere wrijvingscoëfficiënt. Er is wel belastingsingulariteit bij een hogere wrijvingscoëfficiënt, waarbij de contactoppervlakken bijna altijd aan elkaar vastkleven. Na 20.000 cycli is er belastingsingulariteit in het regime van gedeeltelijk schuiven, terwijl er geen belastingsingulariteit is in het regime van grof glijden. De resultaten tonen aan dat er meer aandacht moet worden besteed aan de maaswijdte op het raakvlak van het eindige-elementenmodel bij wrijvingsomstandigheden onder het regime van gedeeltelijk schuiven.

3. Ten derde wordt een eindige-elementenmodel met een laag van gruis ontwikkeld om het effect van gruis te bestuderen op het frettingslijtageproces. In dit model wordt rekening gehouden met de dikte en met elasticiteitsmodulus van de laag. De gruislaag wordt in verschillende stadia geïmporteerd gedurende het frettingslijtageproces. Het stadium waarin de gruislaag wordt geïmporteerd is dus een andere parameter in dit model, gezien de dikte van de laag wijzigt in functie van het aantal wrijvingscycli. De eindige-elementenresultaten tonen aan dat Youngs modulus van een laag van zekere dikte weinig invloed heeft op de verdeling van contactdruk in de raakvlakken tussen blok/laag en laag/specimen. De dikte van een bepaalde materiaallaag heeft echter wel een invloed op de verdeling van contactdruk op het contactoppervlak tussen laag/specimen wanneer de frettingslijtage plaatsvindt. Door de dikte van de laag te vergroten, verlaagt de maximale contactdruk en verhoogt de contactbreedte. Na een zeker aantal cycli, wijzigt de verdeling van contactdruk aanzienlijk: de contactdruk vermindert in het midden van het contactoppervlak, en verhoogt dramatisch aan de rand van de laag als gevolg van de concentratie van de druk. Tegelijkertijd is de contactbreedte groter vergeleken met de contactbreedte zonder gruislaag. Ook het stadium waarin de gruislaag wordt geïmporteerd is een sleutelfactor voor de verdeling van contactdruk. Dit betekent dat het in rekening brengen van de gruislaag een aanzienlijke impact zou kunnen hebben op de vorm en dimensies van slijtageschade.
4. Ten slotte wordt het eindige-elementen voorspellingsmodel voor frettingslijtage omgezet in een 3D-fretdraadmodel. Het contact tussen de fretdraden wordt gesimplificeerd tot een configuratie van gekruiste cilinders in een rechte hoek, volgens de relevante experimentele opstelling. Deze studie onderzoekt de invloed van het gedrag van materialen, namelijk elastische vervorming en elastische volplastische vervorming, op frettingslijtage.

   De eindige-elementenresultaten worden ten eerste gevalideerd met analytische oplossingen en experimenten. Daarna worden de wrijvingsloops en de slijtagediepte geanalyseerd na 1.000 cycli bij verschillend materiaalgedrag.

   Bij elastisch materiaalgedrag, tonen de resultaten aan dat de eindige-elementenmethode goed overeenkomt met de oplossing van Hertz. Bovendien ligt de slijtagediepte die bekomen wordt op basis van de eindige-elementenmethode dicht die van bij het experiment. Het wrijvingscircuit dat bekomen wordt door eindige-elementensimulatie is echter, in tegenstelling tot

de experimentele resultaten, een typische grof-glijden vorm. Bij elastische volplastische omstandigheden is de vorm van het wrijvingscircuit na 1.000 cycli dezelfde als die bij elastische omstandigheden, maar de afgevoerde energie is hoger. Bovendien zijn de slijtagediepte en de slijtageschade berekend bij plasticiteit anders dan die bij elastische omstandigheden.

Table of contents

List of symbols

a	Contact radius	mm
R	The effective radius of curvature of the two bodies	mm
R_1, R_2	The radius of deformable body 1 and body 2, respectively	mm
δ	Relative slip between contact surfaces	mm
δ_E	Relative slip measured from experiment	mm
L	The length of the cylinder	mm
b	The half width of contact area in line contact	mm
P	Normal force applied in the contact model	N
D	The tangential displacement applied	µm
p	Contact pressure	MPa
E_1, E_2	The Young's modulus of deformable body 1 and body 2, respectively	MPa
ν_1, ν_2	The Poisson ratio of deformable body 1 and body 2, respectively	-
p_{max}	Maximum contact pressure	MPa
Q	Tangential force applied in the sliding contact model	N
q	Tangential traction	MPa
q'	Tangential traction on the sliding point in partial slip condition	MPa
q''	The additional tangential traction in the stick regime under partial slip condition	MPa
c	The half width of the stick regime	mm
r_c	The radius of stick region in partial slip condition of point contact	mm
δ_T	The threshold of relative slip for grossing	mm
P_m	Flow pressure	MPa
H	Hardness of the softer material of contact coupling	MPa

V	Wear volume	mm^3
K_A	Archard wear coefficient	MPa^{-1}
E_d	Accumulated dissipated energy	J
E_{di}	Accumulated dissipated energy in the i^{th} cycle	J
Q_i	The friction force in the i^{th} cycle	N
δ_i	The measured relative slip in the i^{th} fretting wear cycle	µm
K_E	Energy wear coefficient	MPa^{-1}
N	Total number of fretting wear cycles	-
µ	Coefficient of friction	-
μ_i	Coefficient of friction in the i^{th} fretting wear cycle	-
p_i	Normal load in the i^{th} fretting wear cycle	N
σ	The local stress	MPa
r_s	The distance from the singular point	mm
σ_0	The applied stress	MPa
γ	The singularity exponent	-
Δh_i	Increment of wear depth during the i^{th} fretting wear cycle	mm
K_{El}	Local energy wear coefficient	MPa^{-1}
T	The time period of the i^{th} fretting cycle	s
N_{int}	The number of increments for one FE fretting wear cycle	-
j	The j^{th} increment of one fretting cycle	-
k	The k^{th} sweep by Umeshmotion	-
ΔN	Jump cycle in FE simulation	-
z	The mesh size of the fine mesh	µm
λ	The scale factor of scaling mesh size	-
t	Thickness of layer debris	mm
h	Wear depth	mm

List of abbreviation

CoF	Coefficient of friction
FEA	Finite element analysis
FEM	Finite element method
THR	Total hip replacement
KI-COF	Kinematic isotropic coefficient of friction
LDC	Large displacement case
SDC	Small displacement case

List of figures

List of tables

Chapter 1

Introduction

1.1 Wear and Fretting wear

Wear is a common material damage phenomenon in contact surfaces. During wear process, material is removed from one or both contact surfaces because of sliding, rolling, impact or relative motion.

Based on ASTM Committee G02 [1], wear could be categorized into two main classes: abrasive and nonabrasive, as shown in Figure 1-1. Fretting is categorized in the non-abrasive section and is defined as a type of wear due to sliding.

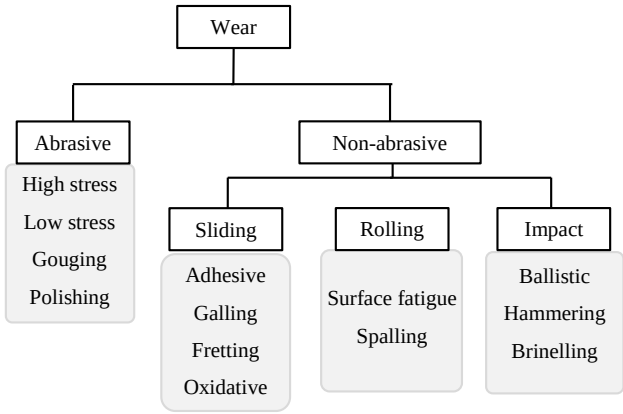

Figure 1-1. Types of wear and some specific modes in each type [1]

Fretting, in tribology field, is a small oscillatory motion between contact surfaces. Depending on the relative movement at the contact interface, the fretting regime is categorized into three types: stick regime (no movement at the interface), partial slip regime (sticking at the centre of the interface with sliding approaching contact edges) and gross sliding regime (sliding alone the whole contact interface). Unlike rolling or reciprocating, usually, fretting happens where the contact surfaces are not supposed to move relatively to each other. This movement is attributed to the deflection of machine components with clamped joints or press fits. Occasionally, this movement is very small as in the case of gear couplings and spline couplings [2].

Fretting wear, namely, is wear induced by fretting [3]. Due to its micro scale movement, the debris generated from contact surfaces is difficult to jump out of the interfaces during wear process. In practical applications, fretting wear causes some undesired results:

1. The jointed parts may become loose.
2. The sliding parts may be stuck with each other.
3. The stress concentration and the micro cracks may occur at the contact surfaces, which may accelerate the failure of the structure.

Fretting wear could be found in every tribosystem in the oscillatory condition. The most typical occasions of fretting wear are introduced in the subsequent section.

1.2 Fretting wear problems

1.2.1 **Blade/disk contact**

The blade/disc dovetail connection is an important element in the fan and compressor rotor assemblies of an aero-engine [4]. Figure 1-2 shows that this connection is subjected to fretting when the engine is rotating. This fretting is induced by the centrifugal blade load and the aero-dynamical high frequency vibrations acting on the blade. Due to this wide range of the vibration, both gross sliding and partial slip may happen at the blade/disk contact. For instance, the stroke is 200 μm when the engine starts and stops, while during the fight the micro-sliding induced by the aerodynamic perturbation is usually less than 10 μm [5-7].

In application, titanium alloy Ti-6Al-4V is widely used for both blade and disk because of its high strength to weight ratio and corrosion resistance. However, due to its poor tribological properties, coating is employed to minimize fretting wear. Therefore, in such a case, it is necessary to understand the fretting wear process including the evolution of worn surfaces and the service life of the coating.

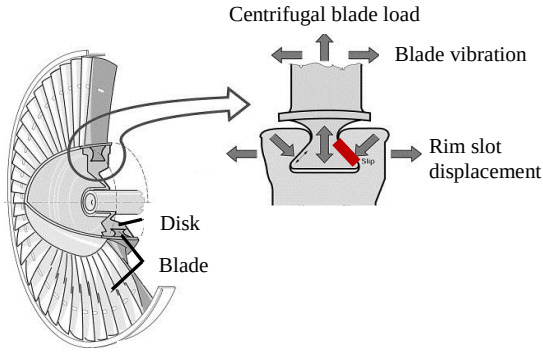

Figure 1-2. The blade/disk contact of a turbine engine [6]

1.2.2 **Ropes contact**

Rope contact is another classic example of fretting problems in practical applications. Ropes have wide applications in the industrial field due to their high axial strength and bending flexibility. Structurally, as shown in Figure 1-3, one rope consists of strands of wires wound together in a variety of arrangements, generating plenty of contact interfaces between wire/wire and strands/strands. The mechanical properties of the rope not only depend on the material properties of wires and the core, but also rely on the size of wires, the number of wires in one strand and the wind pattern of wires in the strand.

Based on different work environments, ropes could be divided into two groups: ropes for overhead conductors and hoisting ropes. The fretting wear of overhead conductors is introduced in this section, while the latter case will be explained in section 2.8 and Chapter 5 as an application of the fretting wear FE calculation.

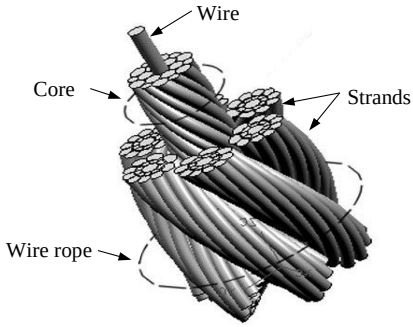

Figure 1-3. Schematic of a wire rope composed of different strands [8]

Overhead conductor is extensively used for the electric power transmission and the distribution to transmit the electrical energy along long distance. The Aluminium-Conductor Steel-Reinforced cable (ACSR) is a classical stranded conductor for overhead transmission with its high-capacity and high-strength. It consists of a solid or stranded steel in the core surrounded by strands of aluminium. The function of steel as a core is to improve the mechanical properties of the rope by means of its high strength and lower thermal expansion coefficient under the current loading [9].

Fretting wear in overhead conductor is mainly due to the wind and the atmospheric corrosion caused by the pollution. Both mixed and gross sliding region have been reported in reference [10] investigating the failure of the ACSR conductor. This fretting damage could lead to the strand failure, even to a blackout and a collapse of the power transition line [11].

In January of 2002, a blackout happened in the southern part of Brazil, reaching approximately 67 million inhabitants. By investigation reported in [10], two possible reasons of the failure of this 29 year-old ACSR conductor have been found, as shown in Figure 1-4. For the ACSR conductor, the rupture of the cable was caused by fretting wear, originating under gross sliding condition due to the wind-induced oscillation. The intense wear of the internal surface in clamp No. 4 reduced the clamping contact pressure, promoting higher displacement amplitude. Thus, the wear of clamp led to more fretting wear of aluminium strand. The superficial degradation of strands was induced by the high cyclic tangential load with the oxidation of the metallic detached particles [10], while steel strands were failed by ductile damage due to the microstructural thermal destabilization and the overload. As mentioned in reference [10], the middle age of the transmission line is 25-40 years. The corrupt rope of the transmission line has worked for 29 years before failure. Therefore, it is approximate 26% to 40% reduction of lifetime.

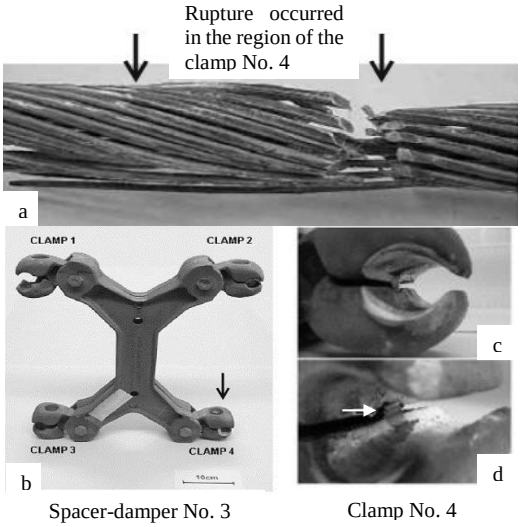

Figure 1-4. (a) The general view of the ACSR conductor adjacent to the spacer damper No.3, (b) The general view of the quad spacer damper No. 3, the ruptured ACSR conductor passed through the clamp No. 4 (see arrow), (c) and (d) details of the internal surface of the clamp No. 4, showing intense wear (see arrow) [10].

1.2.3 **Electronic/electrical connectors**

Nowadays, electronic and electrical connectors are widely used in electronic and control systems of transport, machining and other industrial applications. Unfortunately, as reported in [12], more than 60% of the electronic problems in cars are related to the fretting contact problems. When these connectors are subjected to vibration, and heating and/or environmental changes, fretting wear may occur. The metallic contact of them may become the weak link of the whole devices, since the oxide debris between electronic connectors causes the conductive failure due to the high conduct resistance. Usually, fretting wear under the gross sliding condition generates more debris than in partial slip condition. In addition, the research of [12] revealed that the electrical lifetime in partial slip regime was infinite due to the unworn sticking was at the contact centre. Therefore, the fretting wear under the gross sliding regime has higher risk to cause in the electronic failure.

An example of these is the embarked connector presented in Figure 1-5. The oxide debris generated in fretting wear covers the contact interface and induces high electrical contact resistance. In order to solve this problem, various coatings, such as

non-noble (Sn), semi-noble (Ag) and noble (Au), are applied on contact surfaces depending on the loading intensity [13]. Although applying these coating materials could avoid the generation of oxide debris, fretting damage still occurs when these protective coatings are worn out.

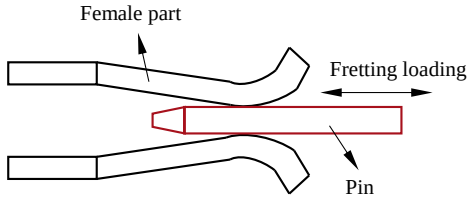

Figure 1-5. The schematic representation of a embarked component under the fretting condition [12]

Besides inducing electrical contact failures, fretting wear is also a possible reason for the failure of Hard Disk Drivers (HDD). When the HDD is working, a suspension spring with a spherical protrusion (dimple) is loaded against a flat gimbal spring. The structure shown in Figure 1-6, allows the roll and pitch motion of the slider in addition to a vertical degree of freedom [14, 15]. Thus, the magnetic head, which is attached to this gimbal, is reading/writing data by rotating around recording tracks. During this process, a micro slip occurs between the surface of the dimple and the surface of the gimbal, by positioning of the suspension arm. Moreover, a small-scale motion also happens in the loading/unloading process, track seeking, and during the axial motion of the slider to disk run-out. Due to these undesirable slip motions, wear debris is generated by fretting wear and causes the failure of HDD.

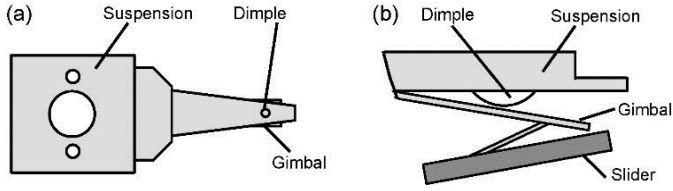

Figure 1-6. The suspension assembly of HDD: (a) top view, and (b) side view [15]

1.2.4 **Contacts in the Total Hip Replacement (THR)**

THR is a surgical procedure that relieves pains from most kinds of hip arthritis for the large majority of patients [16]. Figure 1-7 is a good illustration that clearly shows the

structure of a total hip joint and the position of implants in the hip. When assembling components and inserting them to the hip, many contacts are generated, such as acetabular cup/plastic line/femoral head contacts and femoral stem/bone contacts.

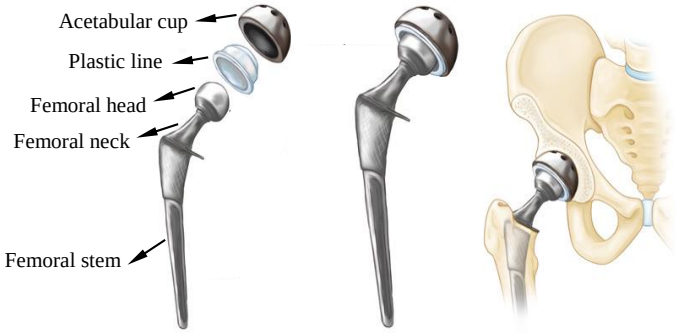

Figure 1-7. Left: Individual component of a total hip artificial prosthesis, centre: The assembly, right: The implant as it fits into the hip [16]

Among these contact surfaces, by the reason of different material properties and geometries, fretting occurs when patients suffer stresses during walking. In this condition, two critical issues limit the service life of an artificial hip joint, namely the fixation/loosening related to the implant/bone interaction, and the wear of the articulating surfaces [17]. If the metallic debris from fretting wear and corrosion is in and around the hip joint, patients may experience inflammation, Adverse Local Tissue Reactions (ALTRs), hypersensitivity/allergic reactions and the bone loss. For a metal-UHMWPE artificial hip joint, the normal mechanistic life can reach 40 years, but its maximum biological life is reduced to no more than 10-15 years that is 25%-40% of the service life [18].

Due to the potential fretting and corrosion existing in the joint between the femoral stem and the neck component of an ABGII Modular System, on 12 July 2012, the Therapeutic Goods Administration (TGA) of Australia advised that Stryker Australia Pty Ltd was recalling the ABGII Modular Femoral Stem and Modular Neck system used in hip replacements [19].

1.3 Advantages of using finite element method (FEM)

Cases of fretting wear listed in section 1.2 reveal the importance of predicting fretting wear and reducing wear damage in our real life before failures occur. However, these cases also indicate two features of fretting wear problems in engineering, which increase difficulties in the research of fretting wear:

1. It occurs in all quasi-static loaded assemblies under vibration, from traditional industry, such as aerospace industry, to biomedicine as in case of the artificial hip joint replacement or the knee implant.
2. It is a complex damage phenomenon involving material properties, working environment, loading conditions, *etc*.

For the first aspect, it is not easy to create a general test rig to reproduce and study practical fretting wear problems in the laboratory. In addition, owing to the complexity of fretting wear, parametric study raises higher requirements for the test rig design and selection. Besides, contact variables, which are essential to calculate wear damage, and evolutions of wear scars are not easy to measure during experiments.

In order to solve these difficulties encountered in the experimental fretting wear study, numerical methods attract researchers' attention, taking advantage of the fast development and the more popularity of computer science. Among these numerical methods, FEM is extensively employed to solve complicated physical problems. As a numerical method, FEM makes continuous domain discretization to calculate approximation and analyse behaviours of objects. This method has been implemented to different practical applications under fretting condition, for instance, the aero-engine blade/disc dovetail [4, 20] and the total hip replacement [21, 22].

1.4 Motivation the thesis

Although research on fretting wear has been carried out for years, factors influencing fretting wear and simulation results are still needed to be studied. This dissertation seeks to extend our knowledge on fretting wear using FEM, especially on the effects of a variable Coefficient of Friction (CoF), the role played by the debris layer and the singularity problem on fretting wear, which have not been investigated previously. The specific objectives of this thesis will be presented in section 2.9.

1.5 Outline of the thesis

This thesis consists of six chapters, which are arranged as:

Chapter 1: Firstly, fretting wear and its problems in different practical applications are introduced. Next, the advantages of FEM for fretting wear simulation are presented. Following the motivation of the thesis, the organization of the thesis is described at the end of this chapter.

Chapter 2: The theoretical foundation for the wear calculation is presented. Contact mechanics is introduced followed by the definition and discussion of "fretting" and "fretting wear" based on literature review. Then, experimental study of the fretting wear process is described in detail for a better understanding of wear mechanisms. Next, the two main wear models: Archard model and energy model are introduced. Then, the literature review on FEM of fretting wear is discussed including the debris models. After a brief introduction of the singularity study in FEM and fretting wear problems in fretted ropes, the specific objectives of the thesis are presented.

Chapter 3: FEM of fretting wear in the line contact is described including: the contact model, the fretting wear model with and without a debris layer. Meanwhile, the evolution of CoF in running-in stage is expressed. The singularity signature is also introduced to study the mesh sensitivity of the fretting contact. Simulation parameters of various objectives are listed at the end of this chapter.

Chapter 4: The results of fretting wear in the line contact are presented. Firstly, the verification using Hertzian solution and the validation with experimental results are conducted. Then the mesh sensitivity in fretting wear simulation is studied. Different displacements applied, CoFs and wear cycles are used to choose the suitable mesh size for fretting wear simulation. Based on different fretting wear models, the influence of evolution of CoF on the final wear scar and the wear scar of running-in stage are compared. The impact of the debris layer on fretting wear is also discussed at the end of this chapter.

Chapter 5: The fretting wear problem of fretted wires as an application is investigated based on FEM. In this chapter, the influence of material behaviour on the fretting wear calculation is considered. The wear coefficient is calculated based on two material models, namely elastic and elastic-perfectly-plastic.

Chapter 6: Concluding remarks and some recommendations for future work are presented.

1.6 Concluding remarks

In this chapter, a short introduction of fretting wear and several typical fretting wear problems are presented. Meanwhile, the advantages of FEM for studying fretting wear are listed. In the end, the motivation of the thesis and its outline are introduced. This chapter is summarized by the frame illustrated in Figure 1-8.

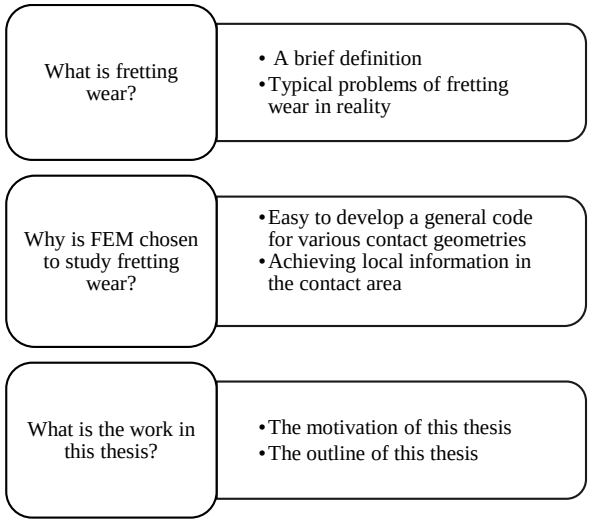

Figure 1-8. Summary of Chapter 1

Chapter 2

Literature review

2.1 Overview

This chapter starts with the introduction of contact mechanics, which is the theoretical foundation for the wear analysis. Next, the definition of "fretting" with different criterion and fretting wear, which is the predominant damage in gross sliding regime, are described. Then, the literature review on experimental studies of fretting wear is discussed from two aspects: a) debris effects and b) evolution of CoF in fretting wear. Based on these experimental studies, two wear models for the wear volume calculation, namely Archard model and energy model, are presented. Both models could be employed for the fretting wear modelling. Various FE models for fretting wear proposed in last ten years are reviewed. In addition, the singularity problem is also introduced as the theoretical base for studying the mesh sensitivity in fretting contact simulations. In addition, the study on fretted wires is briefly introduced. In the end, objectives of the thesis are listed.

2.2 Contact mechanics

As Popov wrote in the book of [23] "the subject of contact mechanics and friction is ultimately about our ability to control friction, adhesion, and wear and to mold them to our wishes", before explaining the definition of "fretting" and "fretting wear", contact mechanics is briefly introduced.

When two bodies touch each other, very high stresses are generated at the contact surfaces. These stresses could cause damage in the form of fracture, yielding, surface fatigue and wear. In order to avoid or reduce these damages, predicting stresses with high accuracy is necessary. However, in reality, it is difficult to obtain accurate contact stresses due to rough surfaces and complicated geometries. Therefore, one question arises: could we achieve approximation of contact problems?

Contact mechanics is the study of the stresses and the deformation of bodies touching each other. This topic focuses on computations involving elastic, viscoelastic, and plastic bodies in static or dynamic contact problems. Among these wide range of calculations, Hertzian contact may be the most popular and widely used solution [24]. It is the fundamental theory for analysing the contact area and contact stress distributions in deformable frictionless contact interfaces.

2.2.1 **Hertzian contact**

In 1882, Heinrich Hertz's classical paper "On the contact of elastic bodies (written in German)" was published, which is "the first satisfactory analysis of the stressed at the contact of two elastic solids" as mentioned in the well-known contact mechanics tutorial "contact mechanics"[25]. During the last more than one hundred years, Hertz theory is extensively used in the engineering field to calculate contact variables though it is restricted to following assumptions:

1. Contact surfaces are continuous and non-conforming (*i.e.* initial contact is a line or point);
2. Strains due to contact are small;
3. Each contact body can be considered as in perfectly elastic half-space;
4. The surfaces of contact are frictionless.

With the exception of assumption 4, these assumptions imply that $a \ll R$, where a is the contact radius and R is the effective radius of curvature of the two contact bodies, which is given by:

$$\frac{1}{R} = \frac{1}{R_1} + \frac{1}{R_2} \qquad (2\text{-}1)$$

where R_1 and R_2 are the radii of contact bodies 1 and 2, respectively.

In the following two sub-sections, Hertzian line contact and point contact, which are 2D and 3D contact problems, respectively, are briefly introduced based on [25] and [23].

The line contact configuration:

The contact between two cylinders with parallel axes is a typical line contact configuration. This line contact problem is a plane strain problem, since the strains by contact is much smaller comparing to the lateral length of the deformable block. As shown in Figure 2-1, two elastic cylinders 1 and 2, with same length L and radii R_1 and R_2, respectively, are pressed into contact with the imposed normal force P. Due to this normal load, the contact is generated as a long strip with the area of $2bL$ lying

parallel to *y*-axis, where b is the half width of this rectangular contact area. Moreover, b is determined by:

$$b = \sqrt{\frac{4PR}{\pi E^* L}} \qquad (2\text{-}2)$$

where R is defined by Equation (2-1), and E^* is defined by Young's modulus of E_1, E_2 and Poisson ratio ν_1, ν_2 of body 1 and body 2, respectively, as:

$$\frac{1}{E^*} = \frac{1-\nu_1^2}{E_1} - \frac{1-\nu_2^2}{E_2} \qquad (2\text{-}3)$$

Thus, the contact pressure distribution along *x*-axis is given as:

$$p(x) = \frac{2P}{\pi L b^2}(b^2 - x^2)^{1/2} \qquad (2\text{-}4)$$

which decreases to zero at the contact edge and the maximum pressure p_{max} is achieved at the centre of the contact line, which equals to:

$$p_{max} = \left(\frac{PE^*}{\pi LR}\right)^{1/2} \qquad (2\text{-}5)$$

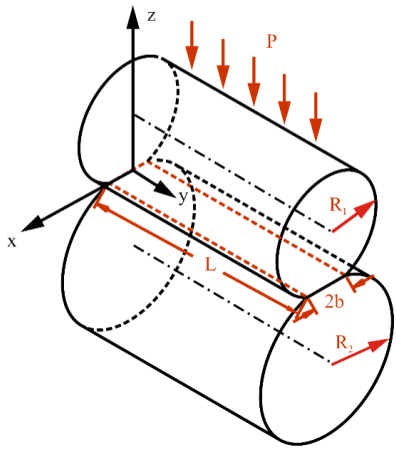

Figure 2-1. Two cylindrical bodies lying parallel to *y*-axis having contact with each other under *P*

The point contact configuration:

If two elastic spheres 1 and 2 with radii R_1 and R_2, respectively, are pressed into contact with the normal force P, as depicted in Figure 2-2, it is a typical point contact. Thus, the contact area is circular and the contact radius a of the contact area could be expressed as:

$$a = \left(\frac{3PR}{4E^*}\right)^{1/3} \quad (2\text{-}6)$$

Thereby, the contact pressure distribution along the contact radius direction r is:

$$p(r) = p_{max}(1 - r^2/a^2)^{1/2} \quad (2\text{-}7)$$

where

$$r^2 = x^2 + y^2 \quad (2\text{-}8)$$

The contact pressure distribution is semi-elliptical and decreases to zero at the edge of the contact. The maximum pressure p_{max} is in the middle of contact area as the line contact, which equals:

$$p_{max} = \left(\frac{6PE^{*2}}{\pi^3 R^2}\right)^{1/3} \quad (2\text{-}9)$$

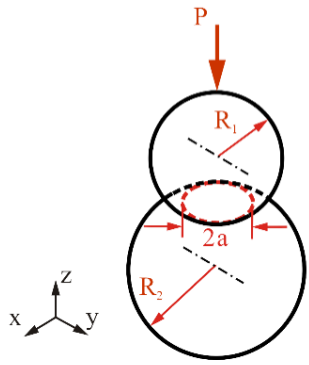

Figure 2-2. Two spheres contact each other

The contact pressure distribution calculated from Hertzian solution is widely used for the verification of FEM contact problems, as presented later in Chapter 4, section 4.2 and Chapter 5, section 5.4.1 .

2.2.2 **Sliding contact**

Since fretting wear occurs under oscillatory situation, the contact condition with the tangential load *Q* and the sliding should be considered. Meanwhile, in this case, CoF plays an important role in the stress distribution and the relative slip between contact surfaces, which are not taken into account in Hertzian solution. Therefore, in this section, the stress distribution and the relative slip under sliding motion are introduced. Besides assumptions of 1, 2 and 3 for Hertzian solution, assumptions of the sliding contact problem also include:

1. The deformation induced by the normal load and the tangential force are independent of each other;

   According to [25], this assumption could be explained as:

   a) The normal displacement u_z at the contact surface due to the tangential force *Q* is proportional to the elastic constant *(1-2v)/G*, where *G* is the shear modulus.
   b) The tangential tractions of each contact surface are equal in magnitude and the opposite in direction, *i.e.*:
   $$q_1(x) = -q_2(x)$$
   c) Based on a) and b),
   $$\frac{G_1}{1-2\nu_1}u_{z1}(x) = -\frac{G_2}{1-2\nu_2}u_{z2}(x)$$

   Therefore, if two contact bodies have the same elastic constants, equal normal displacement with opposite direction are induced by the tangential traction. The warping of the one contact surface conforms exactly to that of the other contact surface. Thereby, the tangential force does not affect the distribution of the contact pressure. If the bodies have different elastic constant, the tangential traction influences the contact pressure. However, this influence is very small. Therefore, the deformation due to the contact pressure and the tangential traction could be assumed that they are independent.

2. Coulomb's friction law is applied at the contact surfaces.

The line contact:

If the applied tangential force *Q* is:

$$Q > \mu P \qquad (2\text{-}10)$$

where μ is the CoF at the interface, a sliding motion occurs at the contact surfaces. This case is called “gross sliding” in fretting range or “reciprocating” in general wear.

Due to the independency of the applied normal load *P* and tangential force *Q*, the contact pressure distribution is given by Hertzian theory as in Equation (2-9). Then, the shear stress distribution could be calculated by Coulomb's friction law as:

$$q(x) = \mp \frac{2\mu P}{\pi L b^2}(b^2 - x^2)^{1/2} \qquad (2\text{-}11)$$

However, if *Q* is less than the limiting friction force, the tangential surface tractions induced by the combination of *P* and *Q* cause “partial slip” since only part of the contact surfaces slides with each other. This partial slip problem is solved by Cattaneo-Mindlin solution proposed by Cattaneo in 1938 [26] and Mindlin [27] in 1949 independently as:

When the bodies are on the point of sliding, the tangential traction is:

$$q'(x) = \mp \frac{2\mu P}{\pi L b^2}(b^2 - x^2)^{1/2} \qquad (2\text{-}12)$$

which follows the same formula as in gross sliding condition as Equation (2-11).

If *Q* does not reach the limiting friction force, the stick area $-c<x<c$ exists at the contact area, where *c* is the half width of the stick area. An additional distribution of the tangential traction over this stick region is given by:

$$q''(x) = -\frac{c}{b}\frac{2\mu P}{\pi L b^2}(c^2 - x^2)^{1/2} \qquad (2\text{-}13)$$

Hence, the overall tangential stress along the contact surface is obtained by the superposition of $q'(x)$ and $q''(x)$. As shown in Figure 2-3, a small relative motion

occurs near to the contact edge, and a stick region exists in the centre of the contact interface.

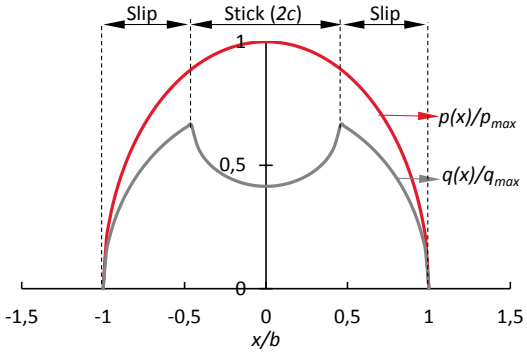

Figure 2-3. The contact pressure and the shear stress distribution in the partial slip condition. *CoF*=0.75, *Q/P*=0.6.

The half width of the stick area is calculated as:

$$\frac{c}{b} = (1 - \frac{Q}{\mu P})^{1/2} \qquad (2\text{-}14)$$

Based on Equation (2-14), it could be found that the combination of the tangential force *Q* and the normal force *P* plays a significant role for the tangential relative motion of the contact.

The Point contact:

When a tangential force *Q* is applied on the sphere in the configuration shown in Figure 2-2, the shear stress distribution could be computed analogously as the line contact case.

If *Q* reaches the limiting friction force, the shear stress is given by Coulomb's friction law as:

$$q(r) = \mu p_{max}(1 - r^2/a^2)^{1/2} \qquad (2\text{-}15)$$

In partial slip condition, the stick region is circular with radius of r_c and concentric with a contact circle. On the point of sliding, the tangential traction distribution is similar to the case of gross sliding:

$$q'(r) = \mu p_{max}(1 - r^2/a^2)^{1/2} \quad (2\text{-}16)$$

And the additional traction distribution in stick region $-r_c < r < r_c$ is given by:

$$q''(r) = -\frac{r_c}{a} p_{max}(1 - r^2/{r_c}^2)^{1/2} \quad (2\text{-}17)$$

The radius of the stick region, r_c, is also calculated by the tangential force Q and the normal load P as:

$$\frac{r_c}{a} = (1 - Q/\mu P)^{1/3} \quad (2\text{-}18)$$

The relative tangential slip δ_c at a radius r within the slip area of the contact surface is computed by:

$$\delta_c = \frac{3\mu P}{16aG}(2-\nu)\left[\left(1 - \frac{2}{\pi}\sin^{-1}\frac{r_c}{r}\right)\left(1 - 2\frac{{r_c}^2}{r^2}\right) + \frac{2}{\pi}\frac{r_c}{r}\left(1 - \frac{{r_c}^2}{r^2}\right)^{1/2}\right] \quad (2\text{-}19)$$

If the tangential force Q reaches the limiting friction force, r_c decreases to 0. Thus, if the normal force P keeps constant, the threshold of the relative tangential slip for gross sliding could be calculated by:

$$\delta_T = \frac{3\mu P}{16aG}(2-\nu) \quad (2\text{-}20)$$

Equation (2-20) will be used for verification of the FE model in chapter 5, section 5.4.2.

Cattaneo-Mindlin solution argues that the tangential loading is the reason for the evolution of a contact region under the constant normal load condition, based on the assumption of the elastic deformation and smooth surfaces of two bodies. However, through experimental results on the very early stage of fretting wear, Ovcharenko and Etsion [28] found that the relative slip δ_c was due to the residual tangential plastic

deformation other than the interfacial slip. Later, Etsion [29] pointed that Cattaneo-Mindlin solution is too idealistic and the practical applicability should be considered.

2.3 Fretting

2.3.1 **Fretting regime**

When talking "fretting wear", the first question jumping into one's mind may be what is "fretting"? According to the definition of ASTM standard G40-13 [3], "fretting" is described as "small amplitude oscillatory motion, usually tangential, between two solid surfaces in contact". Besides the tangential motion, three more fretting motion modes exist [30] in the point contact as described in Figure 2-4:

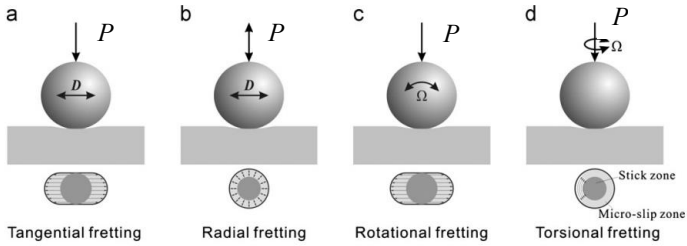

Figure 2-4. Fretting wear motion modes on point contact [30]

1. The **radial fretting** is mainly induced by a variable normal load or thermal cycling. During this process, two surfaces remain in contact and no impact effect occurs. In this fretting motion, micro-slip occurs due to dissimilar elastic constants when the materials of counter-bodies are different.
2. The **torsional fretting** occurs when oscillatory vibration causes reciprocating torsion.
3. The **rotational fretting** is the relative motion of reciprocating rotation also induced by the oscillatory vibration.

In this thesis, only the tangential fretting motion is investigated. Thereby, what is the range of "small amplitude" in tangential fretting? Various criteria exist to distinguish "fretting" and common "reciprocating".

In the 1970s, based on different experimental data, it was generally accepted that the upper transition threshold from fretting to reciprocation is a largely wide interval from 50 μm [31] to 300 μm [32] without considering the effect of the normal load *P*.

However, as shown in Figure 2-5, both the applied normal load *P* and displacement amplitude *D* are the most important parameters that govern the fretting behaviour in theoretical analysis and experiments. Therefore, researchers attempt to generate a criterion combining both the normal load and displacement amplitude, which could be measured in experiments.

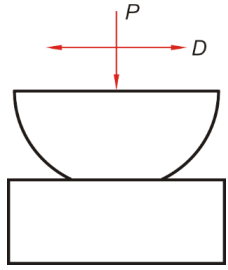

Figure 2-5. Schematic diagram of the fretting contact

Vingsbo *et al.* in 1988 [33] firstly mapped the fretting regime from the measured values: friction force *Q* and displacement amplitude measured in experiment δ_E according to the shape of a hysteresis loop named fretting loop. As depicted in Figure 2-6, a fretting loop is a closed cycle of *Q* versus δ_E plot. According to the shape of the fretting loop, the fretting regime is categorized into three types:

1. **Stick regime** (Figure 2-6 (a)): The Q-δ_E relation is a quasi-closed curve in the contact surface, suggesting that the relative slip is accommodated by the elastic deformation. In this case, two contact surfaces are fully sticking with each other and no energy is dissipated.
2. **Mixed stick and slip regime** (partial slip regime) (Figure 2-6 (b)): The Q-δ_E relation is a quasi-ellipse shape with a transition from an elastic shear-strain relation to a plastic stress-strain relation. After this transition, the evolution of *Q* decreases as the shear stress is relaxed due to the slip near the contact edge. Therefore, in this case the centre of contact surfaces is adhesive, while they slip at the edge of contact. This transition represents the boundary between the stick regime and the slip regime. The dissipated energy could be calculated by the area of this quasi-ellipse shape.

3. **Gross sliding regime** (Figure 2-6 (c)): The Q-δ_E relation exhibits a quasi-rectangular relation. The constant dynamic friction force indicates occurring of the gross sliding at the interface. In this case, the whole contact surfaces slide against each other.

It should be mentioned that the displacement amplitude δ_E in the fretting loop is measured from experiments, *i.e.* δ_E is larger than the displacement amplitude at the contact δ due to containing the limited rigidity of the test rig and the elastic deformation of contact bodies. In addition, during fretting cycles, δ is continuously changing according to the evolution of the contact surface profile. Thus, the fretting regime can change during wear process.

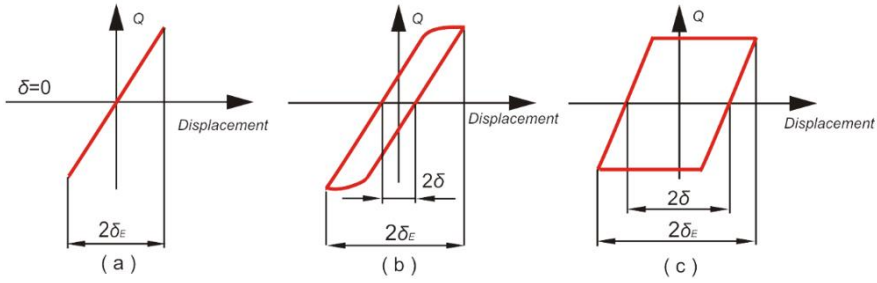

Figure 2-6. Typical fretting loops in different fretting regimes: (a) stick, (b) partial slip, (c) gross sliding [28, 33].

The fretting loop is an effective method to study the fretting behaviours of fretting couples, especially to distinguish the partial slip regime and gross sliding regime. However, the boundary between fretting and reciprocation was still not clear. While as Figure 2-7 shown, the normal load does affect both thresholds of partial slip to gross sliding and gross sliding to reciprocating.

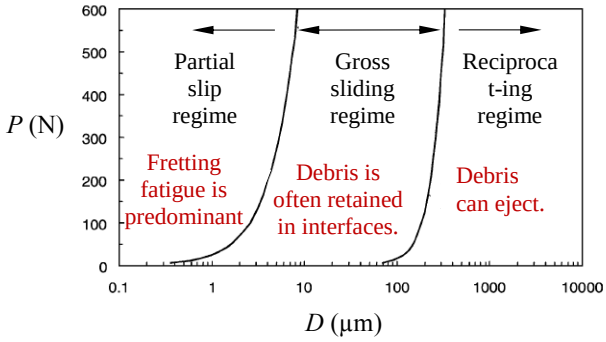

Figure 2-7. The Generalized running condition fretting map (SC652/100C6, R = 12.7 mm) [34]

Therefore, the next question is how can we differentiate "fretting" from "reciprocating" by considering the imposed normal load and the displacement amplitude?

In 1996, Fouvry *et al.* [35] suggested that to determine the boundary between fretting and reciprocating, the comparison of relative slip between two contact surfaces δ and the contact radius a of point contact or the half contact width b of line contact should be considered. They proposed a parameter, e, which is given by:

$$\text{Point contact: } e = \frac{\delta}{a} \qquad (2\text{-}21)$$

Or

$$\text{Line contact: } e = \frac{\delta}{b} \qquad (2\text{-}22)$$

The parameter e is an index to distinguish fretting and reciprocating. When $e < 1$, an unexposed area exists in the contact surface and it is in the fretting regime. While if $e > 1$, all the contact surface is exposed to the surrounding atmosphere and it is in the reciprocating condition. Due to difficulties for measuring δ, a and b during experiments, this index is usually employed to determine the initial experimental parameters, for instance, the applied displacement amplitude D could be decided by parameter a or b calculated from the Hertzian solution.

However, by investigating the characteristics of wear before and after the transition of fretting and reciprocating experimentally, G.X. Chen [36] in 2001 found that the

criterion presented by Fouvry *et al.* [35] was not consist with experimental results. In this work, the wear coefficient and the wear volume after a constant sliding distance, CoF, the wear scar profile and the wear debris were studied. They found that: 1) Over a constant sliding distance, the wear coefficient was greater with increasing the applied displacement amplitude in fretting wear, while it is kept constant in reciprocating wear; and 2) the extend and sizes of non-oxidized metallic debris in reciprocating wear are larger than in the fretting wear condition. They also pointed out that transition between fretting wear and reciprocating wear strongly relied on the testing conditions and material properties.

In 2004, M. Varenberg *et al.* [37, 38] introduced a criterion termed slip index. This index is defined by:

$$Slip\ Index = DS_C/P \qquad (2\text{-}23)$$

where S_C is the elastic slope of the fretting loop, combining the tangential stiffness of the contact interface and the machine support.

Based on the evolution of CoF with the slip index as shown in Figure 2-8, the reciprocating wear occurs when $Slip\ Index > 11$. When $Slip\ Index < 10$, it is in the fretting regime. Gross sliding happens at $0.8 < Slip\ Index < 10$, and partial slip occurs in $0.5 < Slip\ Index < 0.6$. The threshold between gross sliding and reciprocating is identical in both conventional fretting and nano-scale fretting, confirmed by experiments by the conventional test rig and Atomic Force Microscopy (AFM).

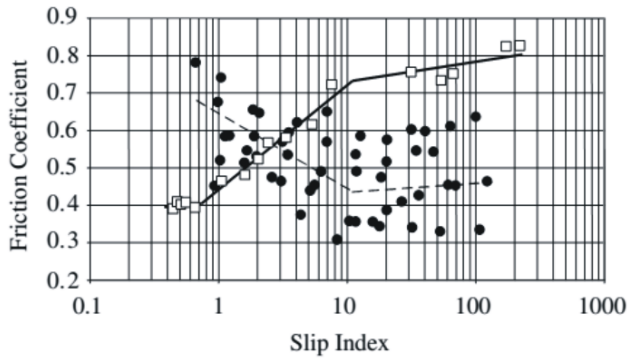

Figure 2-8. The relation between friction coefficient and slip index obtained by experiments (□ conventional fretting test rig and ● the AFM) [37]

Ten years later, Pearson *et al.* [39] argued that no clear evidence had been found that the wear coefficient was dependent on the slip amplitude δ in the contact surface. They proposed that the true wear coefficient k_{true} was larger than the nominal wear coefficient $k_{nominal}$, due to ignoring the elastic deformation of the system and the threshold energy for fretting wear. In fact, $k_{nominal}$ is the wear coefficient presented in [36], where mentioned that $k_{nominal}$ strongly relies on the applied displacement amplitude.

In summary, the transition from partial slip to gross sliding in fretting is widely agreed on whether or not the stick regime exists in the contact surface. This transition could by easily detected by the fretting loop. However, the threshold between fretting and reciprocating still needs more investigation.

2.3.2 **Impact variables in fretting**

The nature of fretting involves a large number of factors including both material properties and the working environment of fretting couples. The main variables affecting fretting are listed in Figure 2-9. Depending on combinations of these parameters, different fretting damages may occur in fretting couples.

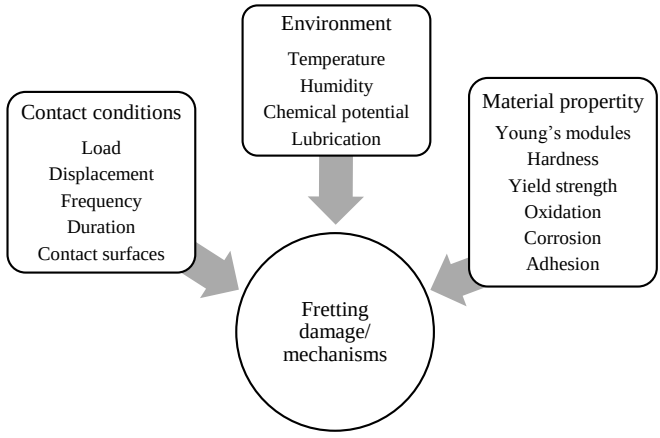

Figure 2-9. Impact factors in fretting [40]

2.3.3 **Fretting damage**

Fretting damage in fretting regime can be grouped as three types [41]:

Fretting wear: That is wear due to fretting [3]. It occurs in both partial slip and gross sliding conditions. However, it is the predominant damage in the gross sliding condition. Figure 2-10 (a) presents a typical annular worn surface in sphere/plane contact under the partial slip condition: the stick zone is in the contact centre with little wear damage surrounded by the slip zone of severer wear. Figure 2-10 (b) shows the wear scar of the gross sliding condition. In this case, the stick zone vanishes, and the wear damage is prevalent in the whole contact zone [42].

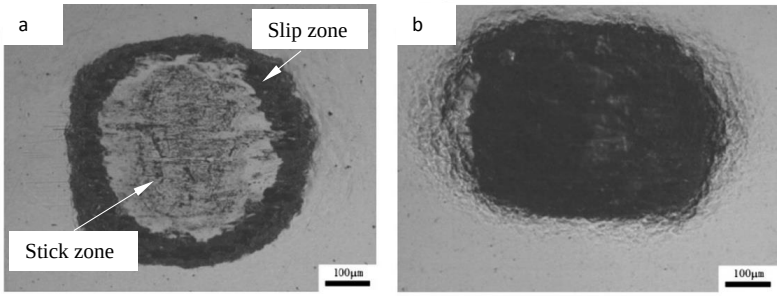

Figure 2-10. The optical microscopic images of worn surfaces with displacement amplitudes of (a) 60 μm, partial slip, and (b) 120 μm, gross sliding [42].

Fretting fatigue: That is fatigue failure induced by fretting, which usually occurs at partial slip condition. It happens at stress levels below the fatigue limit of the material. Figure 2-11 displays the fretting fatigue failure occurring at the blade and disk connection of a turbine engine [43].

Figure 2-11. Fretting fatigue of the blade and disk connection [43]

Fretting corrosion (shown as Figure 2-12**):** That is the deterioration at the contact interface as a result of corrosion and the micro oscillatory slip [44], in which case a chemical reaction rules the extent of the damage during the fretting process.

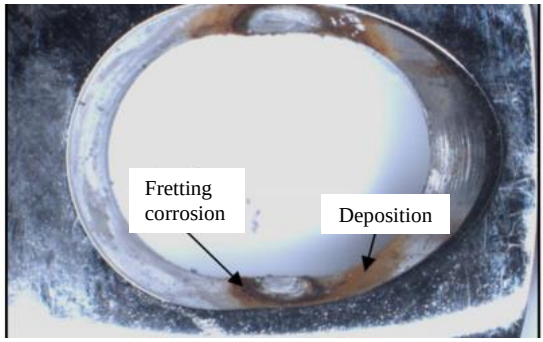

Figure 2-12. Fretting corrosion in the plate hole of a plate-screw connection. Solution: 0.90% NaCl, rocking motion amplitude: 1.70 mm, frequency: 1.0 Hz, and axial load: about 670 N. Total number of cycles: 1×10^6 cycles [45]

Although both fretting wear and fretting fatigue often coexist at the same time [46] and come out as competing process, fretting wear and fretting fatigue are predominant in gross sliding and partial slip, respectively. The main reason of this is that the micro superficial crack generated in gross sliding condition could be eliminated by the material removal. While due to less wear and high velocity of cracking in partial slip condition, cracks initiated on the contact surface have more opportunity to propagate to the inner of the specimen.

2.4 What happens during fretting wear process?

2.4.1 **Wear mechanism in fretting wear**

Classical wear mechanisms have been classified into six wear modes: abrasion, adhesion, fatigue wear, corrosive wear, melt and diffusive wear [47].

Although fretting wear is classified as non-abrasive wear in ASTM Committee G02 [1], it is a very complicated process related to fretting couples. Since debris stays more easily in the contact surfaces during the process of fretting wear, the description of fretting wear process emphasized on the importance of debris was proposed by Hurricks [48] in 1970. This process between metallic surfaces was divided into three

stages: (a) initial adhesion and metal transfer, (b) generation of debris and (c) steady-state wear.

Based on experimental studies, material properties and loading conditions affect the wear mechanisms of fretting wear significantly. One certain mechanism could not explain all different fretting wear processes. To date, abrasive wear [49] and delamination [50] have been found in fretting wear process depending on various loading conditions and fretting couples.

Abrasive wear: Abrasive wear is wear due to the indentation of harder asperities or particles to the softer surface under relative sliding condition. It usually happens when two contact surfaces have different hardnesses. Usually, debris trapped in the fretted contact surfaces is oxide that is harder than the matrix material. In this case, abrasion process, precisely three-body abrasion happens in the fretting couples even between similar materials. Researchers have studied abrasive wear in fretting on material of fretting couples and loading conditions.

1. Material of fretting couples: Colombié *et al.* [49] carried out fretting wear tests of different materials, *i.e.* steel/steel and chalk/glass. They found that the generation and maintenance of the debris layer with abrasion of debris layer governed the wear of the matrix material. This demonstrates abrasion wear is a wear mechanism for fretting wear. Varenberg *et al.* [51] investigated the role of oxide debris in fretting couples of steel/bronze and steel/steel. They found that the wear mechanisms were different according to different types of fretting couples. For the combination of steel/bronze, the adhesive wear mechanism was predominant and the debris acted as a kind of lubricant, which could reduce the damage of fretting wear. While, for the pair of steel/steel, the abrasive mechanism was prevailing, the debris could accelerate the damage. The recent paper of J. D. Lemm [52] presented findings that for fretting couples of steel/steel, of which they had different hardness by heat treatment, a critical hardness differential threshold existed. Above this threshold, the oxide-based fretting debris was trapped on the surface of softer body of fretting couple and protected the softer body, as shown in Figure 2-13. In this case, the wear was predominantly related to the harder specimen, since this retention of debris results in the abrasion wear of the harder counter-face due to the oxide debris.

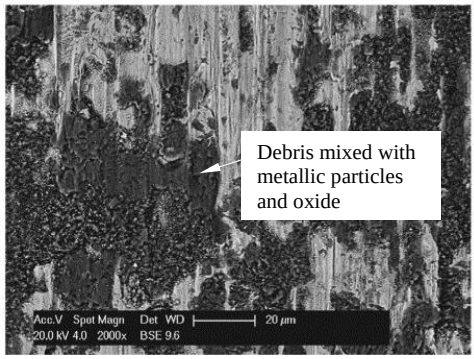

Figure 2-13. SEM of debris trapped in the matrix of the homo-hardness fretting couples [52]

2. Loading conditions: K. Elleuch and S. Fouvry [53] studied the fretting behaviour of aluminium alloy (A357)/52100 steel under different displacement amplitudes. They found that the form and composition of the debris were related to the displacement amplitude threshold that was independent of the sliding velocity and temperature. Besides displacement amplitude, the effect of the normal load and the frequency were also studied on Ti–6Al–4V contact [54]. The normal force sequence governed the interface structure of the contact and the oxidation process, and the frequency controled the wear rate.

Delamination: In 1973, the delamination theory of wear was proposed by Suh [50]. The delamination theory argues that adhesive wear and fatigue wear are caused by the delamination. These wear processes explained by this theory can be summarized in four steps:

1. The dislocations at the surface of the soft material are driven into sub-surface;
2. Subsurface cracks and voids appear;
3. Cracks are joined by the shear deformation of the surface;
4. The wear sheet is generated.

This mechanism considers actual micro-mechanism based on the failure and damage processes, which is closer to the practical situation. The next year Waterhouse and Taylor [55] studied fretted surfaces of 0.7 carbon steel, commercially pure titanium and Al-Zn-Mg alloy. They found that the wear mechanism was adhesion and abrasion when the applied displacement amplitude were higher than 70 µm. Lower than 70 µm,

results showed that loose wear debris was caused by the propagation of sub-surface cracks. This was similar to that postulated in the delamination theory of wear. Recently, Li *et.al.* [42] investigated the effect of the applied displacement amplitude on fretting wear of Inconel 600 alloy. It is found that increasing the applied displacement amplitude to the gross sliding regime, the wear mechanisms changed to the oxidation and delamination. As shown in Figure 2-14, the crack occurs at the subsurface of the contact. Hence, delamination wear is proved as one of wear mechanisms happens in the fretting wear.

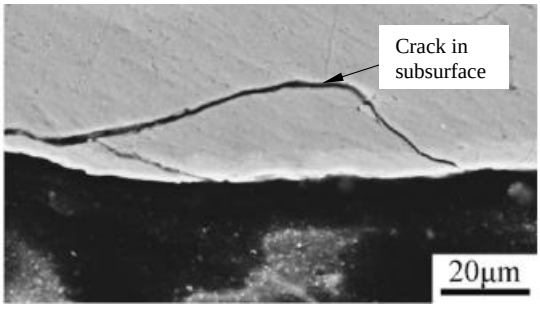

Figure 2-14. SEM of the crack formation at the subsurface of the contact under the gross sliding condition: D = 120 μm, P =100 N [42]

These experimental studies provide important insights into the mechanisms of fretting wear and the important role of the debris. Meanwhile, the mechanical parameters of fretting experiments for the given fretting couples should be carefully controlled in fretting wear studies.

2.4.2 **Evolution of CoF in fretting wear**

Friction is the resistance encountered by two contact bodies sliding on each other, which could cause energy loss and wear in the contact surface. Usually, friction force is described by the CoF and normal load.

CoF is a systems-dependent parameter rather than an intrinsic property of a material or combination of materials. It is sensitive to the sliding distance and the environment, such as the contact pressure and the surface quality [56]. Blau [57] grouped factors impacting the friction behaviour as: the contact geometry, fluid properties and flow, lubricant chemistry, the relative motion, applied forces, third-bodies, temperature, stiffness and vibrations.

In the process of fretting wear, both the applied normal load and the displacement amplitude have significant influences. Figure 2-15 shows that CoF of the steady stage decreases with increasing the normal load for a given displacement amplitude. Similar tendency could also be found in the fretting couple of the high strength alloy steel [58] and steel wires [59]. This tendency may be explained by that when the normal load is small, the elastic deformation causes asperities of contact surfaces to interlock with each other, inducing high CoF. When increasing the normal load to activate the plastic deformation of asperities, CoF becomes lower due to less effect of interlock [60]. Figure 2-16 shows that the applied displacement amplitude does affect CoF under both dry and lubricated contact for a given normal load. Besides the continuous changing of the contact pressure attributed to the evolution of contact geometries, debris also plays a significant role. Depending on the composition of the debris, a critical contact pressure exists at which a transition to a higher CoF occurs [61].

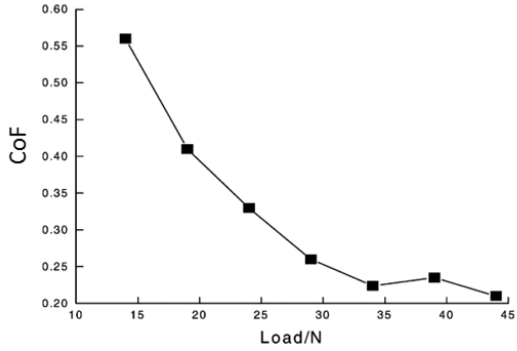

Figure 2-15. The evolution of CoF of the steady stage for different normal loads, D = 75 μm [60]

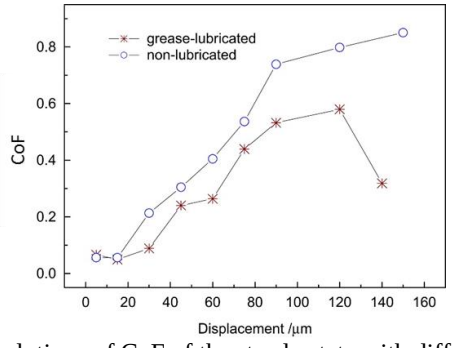

Figure 2-16. The evolutions of CoF of the steady state with different displacement amplitudes under friction-increasing grease and dry friction conditions, P = 24 N [59]

For a given fretting couple, the evolution of CoF with the number of fretting wear cycles usually could be divided into 3 stages, as shown in Figure 2-17. In the initial running-in stage, CoF is low since contact surfaces are covered by the oxide and the 'nature pollution' film weakening the adhesion between contact surfaces. Later on, CoF increases gradually due to the removing of this film and more adhesion and abrasion appearing in substrate interfaces. Then, the balance between generation and ejection of debris is reached. Therefore, CoF keeps stable at the last stage [60].

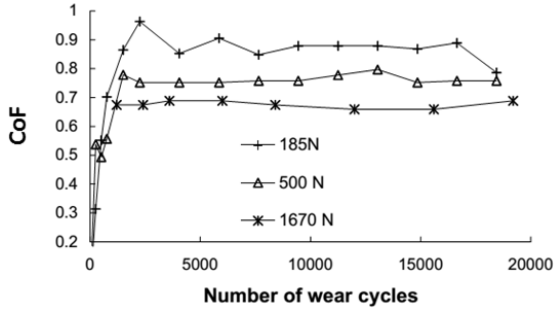

Figure 2-17. The evolution of CoF during fretting wear tests [58]. R = 6 mm and D = 25 μm

Based on experimental results presented above, it could be concluded that fretting wear is a very complex phenomenon of the surface damage and that debris plays an important role. It depends on materials of fretting couples (types, hardness), loading conditions (the normal load and the displacement amplitude) and environmental conditions.

2.5 Wear models

As mentioned in section 1.2 fretting wear problems reduce service lives of applications dramatically. Hence, it is necessary to predict the fretting wear behaviour based on materials of the fretting couple and the work environment. Thus, a wear model linking working conditions and the wear damage for a given fretting couple is necessary.

Among last ten years literature, there are two main wear models to simulate fretting wear, namely, Archard model and energy model. Both of them are contact-mechanics-based models [62]. In the following sections, both models are introduced briefly.

2.5.1 **Archard model**

Archard model is firstly proposed by Archard in 1953 [63] and validated by Archard and Hirst in 1956 [64]. In this model, the wear volume per unit sliding distance $\frac{V}{s}$, named wear rate of a given sliding system, is calculated by the normal load P and the flow pressure P_m as:

$$\frac{V}{s} = k\frac{P}{P_m}, \qquad (2.24)$$

P_m is approximately equivalent to the hardness of the soft material H, *i.e.* $P_m = H$. The physical meaning of $\frac{P}{P_m}$ is the real contact area for fully plastic asperities [65].

k is called wear coefficient related to the probability of each contacting asperity contributed to the loosened particle leaving the system. From experimental observations, the stead-state wear rate is constant for the duration of the wear test. Thus, k of a specific sliding system is also constant and could be obtain from experiments. The formula for the calculation of k is:

$$k = \frac{HV}{Ps}, \qquad (2.25)$$

For engineering applications, the ratio k/H named Archard wear coefficient or dimensional wear coefficient is more useful for comparing wear rates of different classes of materials. Therefore, Archard equation could be rewritten as:

$$\frac{V}{s} = K_A P, \qquad (2.26)$$

where K_A is the Archard wear coefficient, $K_A = k/H$.

2.5.2 **Energy model**

Introducing energy concept to predict wear kinetics and geometrical changes of the wear scar is another method. This dissipated energy method can be dated back to 1960s. Matveevsky [66] firstly proposed that friction power intensity (frictional energy dissipated per unit area) is related to wear when studying oil-lubricated Hertzian point and line contacts.

Fouvry and co-workers investigated fretting wear based on energy concept further. In their fundamental work [35], they suggested that the frictional work was the global energy dissipated in initiation, stimulating and activating various processes related to wear. This concept is presented in Figure 2-18.

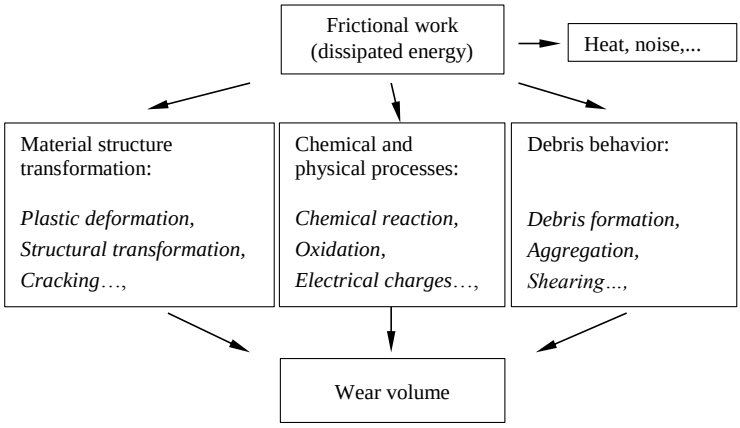

Figure 2-18. Dissipated energy concept on the wear process

Summation of the frictional work of each wear cycle of the whole duration is the accumulated dissipated energy E_d. This dissipated energy could be calculated from experiments by fretting loops formed from the friction force and the relative slip (Figure 2-19) as:

$$E_d = \sum_{i=1}^{N} E_{di} = \sum_{i=1}^{N} 4Q_i\delta_i, \qquad (2\text{-}27)$$

Where E_{di} is the area of the fretting loop in the i^{th} fretting wear cycle and N is the total number of fretting wear cycles in the experiment. Q_i is the shear force and δ_i is the relative slip at the interfaces in the i^{th} fretting wear cycle.

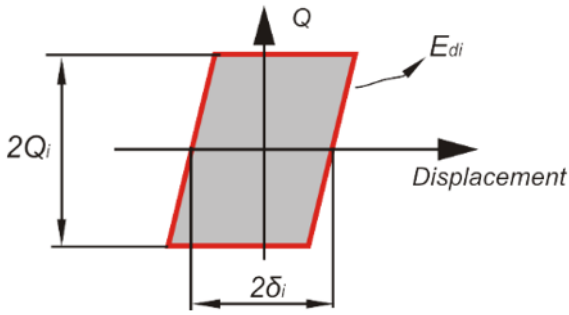

Figure 2-19. Calculation of the dissipated energy in one fretting wear cycle

Meanwhile, linear relationships between the wear volume and the dissipated energy as presented in Figure 2-20 were observed [67]. These results were from experiments of different steels (DC1 and SC652)/Alumina and different hard TiN, TiC coatings with substrate of a high-speed steel (SC652)/Alumina under the fretting and reciprocating sliding condition.

Therefore, based on the Coulomb's friction law, the energy model could be written as:

$$V = K_E \sum_{i=1}^{N} E_{di} = K_E \sum_{i=1}^{N} 4Q_i\delta_i = K_E \sum_{i=1}^{N} 4\mu_i P_i \delta_i \qquad (2\text{-}28)$$

where K_E is the energy wear volume coefficient of the studied interface for a given displacement amplitude, which can relate the evolution of wear volume to the additional energy dissipated during fretting wear process. μ_i and P_i are the CoF and the normal load of the i^{th} fretting wear cycle, respectively.

The group of Fouvry also explained the formation of Tribologically Transformed Structure (TTS) in fretting wear and demonstrated that there was a specific threshold dissipated energy E_{dth} before starting wear (Figure 2-20) [68, 69].

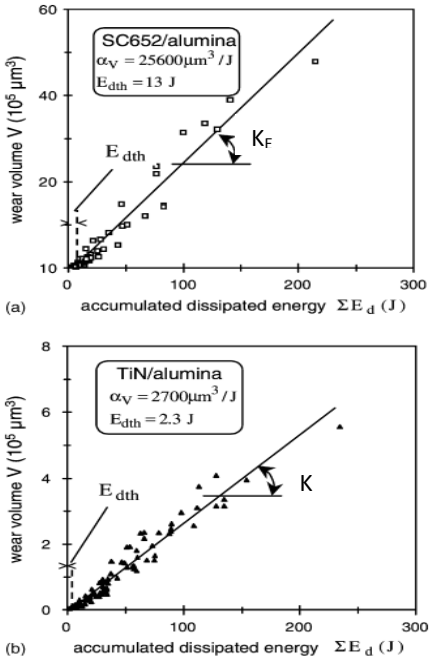

Figure 2-20. The linear relations between the accumulated energy and the wear volume. (P = 50-200 N, D = 25-200 µm, room humidity = 50%) [67]: (a) SC652/alumina; (b) TiN/alumina.

Archard model links the wear volume to the normal load and the sliding distance of the given tribology system. The main shortcoming of it is without explicitly considering the influence of CoF on the fretting wear process. In contrast, energy model is based on the conservation of energy, *i.e.* part of the frictional work is consumed by the wear process. The evolution of CoF in the duration of fretting wear is explicitly involved in the calculation of fretting wear volume, which makes it possible to investigate the effects of CoF on fretting wear by FEM. In addition, the wear process may consist of the material structure transformation, chemical and physical processes, and debris behaviour. Energy model is also convenient to explain different wear mechanisms. Therefore, energy model is used in this thesis to simulate the fretting wear process.

2.6 Fretting wear simulation of line contact by FEM

By means of wear models introduced in section 2.5 and FEM, it is possible to predict the fretting wear process. To date a number of studies have been examined this problem in various aspects. Main research and findings are reviewed in this section. This review is divided into two sections: FE models with and without debris effects.

2.6.1 Fretting wear simulation without considering debris effects

Loading conditions:

As loading conditions, such as the imposed normal load and the tangential displacement amplitude, affect fretting behaviour significantly, the early study of fretting wear by FEM focused on the effects of loading conditions on fretting damage. In 2003, McColl *et al* [58] firstly proposed a FE model to predict the evolution of contact geometry, surface contact variables and sub-surface stresses under various normal load conditions based on Archard model. They compared the predicted results with experimental results and found an underestimation of wear volume in higher normal load cases. They also proposed that possible reasons of this disparity were using global wear coefficient and ignoring debris effects. Besides normal loads, influences of tangential displacement amplitudes were also studied in [70] under partial slip and gross sliding conditions, and in [71] for only the gross sliding condition. Research in [70] confirms that fretting wear is the predominant damage in the gross sliding condition, while the risk of crack initiation in fretting fatigue is greater in the partial slip regime.

Material properties:

Wear mechanisms during fretting also depend on material properties of fretting couples. Several studies have attempted to explain the role of plasticity playing in fretting wear. Research in [72] found that elasto-plasticity could not explain the sliding dependence of the wear rate, by simulating five wear cycles of fretting wear with a Prager linear kinematics hardening model in a A357 aluminium alloy/AISI 52100 steel contact. For Ti-6Al-4V fretting couples, studies of Dick *et. al.* in [73, 74], by predicting fretting wear of 100 cycles with a cyclic plasticity model, indicted that ratcheting induced stress redistribution, geometry evolution and the formation of residual stress. An elastic-plastic FEA model employed to investigate the evolution of the fretting variables in surface and subsurface was presented by Mohd *et al* [75]. In this study,

special attention was given to the evolution of plastic variables and effects of plasticity during fretting wear, using a kinematic hardening plasticity model to describe the cyclic plasticity behaviour. In addition, the lifetime of coatings was predicted in [76] and [77].

Fretting wear and fretting fatigue:

Madge *et al.* in [78] and [79] introduced a FEA tool integrating wear modelling with fretting fatigue analysis to predict the effects of fretting wear on fretting fatigue life. This method can predict the fretting wear-induced evolution of contact profile, contact stresses and a multi-axial fatigue damage parameter with cumulative damage effects, as a function of slip amplitude, for a laboratory fretting fatigue test arrangement. Zhang *et al.* [80] presented a FEA model based on energy method to compare fretting behaviour of different contact geometries, *i.e.* cylinder/flat contact and rounded punch /flat contact. This method was able to predict the evolution of contact geometry, wear, salient surface and surface variables, such as plasticity and fatigue damage parameters. They found that the fatigue crack initiation was more sensitive in case of the cylinder/flat contact configuration to the effects of slip regime and wear, comparing to the case of rounded punch /flat contact configuration.

CoF

As explained in section 2.4.2 CoF is not a constant during fretting wear process. However, all the FE fretting wear models introduced above contains a constant CoF. In 2007, Cheikh [81] proposed a new friction model, named KI-COF (Kinematic Isotropic Coefficient Of Friction) to describe the evolution of COF governed by the local history of the contact and the amount of slip at the contact surface. Although the difference of fretting loops between experiments and simulations decreased with this model, the information of wear scar was not presented. In 2014, KI-COF model was implemented to simulate deformation behaviour during torsional fretting in [82], which was focused on fretting fatigue and only ten cycles of fretting wear were simulated.

To date, fretting wear by FEM have been investigated intensively including loading conditions, material properties and fretting fatigue. However, the effects of variable CoF in running-in stage (first thousands cycles) and final stage of fretting wear have not been studied. Therefore, studying the influence of variable CoF on fretting wear process simulation is an objective of this thesis.

2.6.2 **Debris models in fretting wear simulation**

Owing to the critical impact of debris in fretting wear process, several numerical models of fretting wear with debris have been developed by researchers.

Based on the experimental observations, Elleuch and Fouvry [72] argued that the debris ejection controlled fretting wear as shown in Figure 2-21 and proposed a modified Archard model considering the ejection process. This modified model could describe a parabolic evolution between applied displacement amplitude and wear volume. Although this model took into account the debris ejection by introducing PSD parameter, debris itself was not included to the fretting wear FE model explicitly. Hence, this model could not specifically capture the stresses or wear evolutions due to debris.

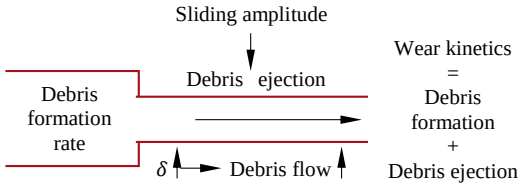

Figure 2-21. The debris flow of wear kinetics under gross sliding condition [72]

In 2007, Ding *et al.* [83] firstly integrated a debris layer explicitly to a FE tool of fretting wear developed by McColl in [58]. Figure 2-22 shows two contact interfaces existing in this model. For the interface between the bottom of debris and the top surface of the flat specimen Γ_1, the contact constraint was assumed to be rigid connection. While for the interface between the bottom surface of cylinder Γ_2 and the top surface of the debris Γ_3, the basic Coulomb's friction law was applied. In this study, geometry evolutions of the debris such as the thickness and the width, and the normal movement of the debris layer, were investigated. This simulation tool predicted debris effects on wear damage by redistributing the contact pressure and the relative slip between contact surfaces based on Archard wear model and Hill's yield model.

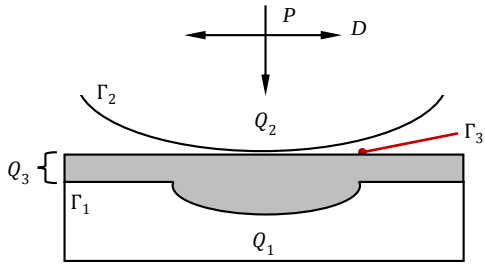

Figure 2-22. The simplified fretting wear contact model with a debris layer, Q_1 and Q_2: the contacting bodies, Q_3: debris. Γ_1: top surface of Q_1, Γ_2: bottom surface of Q_2, Γ_3: top surface of debris[83]

Two years later, the authors presented a multi-scale modelling method for fretting wear simulation [84]. The macro model is a global wear simulation based on Archard model, and the micro model is an asperity contact model based on the roughness characteristics. As shown in Figure 2-23, λ is the wavelength of the asperity spacing, which is estimated by the roughness information of the contacting surfaces. d_{sub} is the instantaneous thickness of the debris layer. Both the normal load p^{sub} and the displacement with amplitude $\lambda/2$ were applied to the micro model. This micro model was used to determine the local plastic deformation under the debris layer and furthermore to gain insightful understanding of fretting wear mechanics. Although some assumptions were made, *i.e.* a) asperities were distributed uniformly, b) asperities were spherical with uniform radius, which were determined by the roughness information and c) asperities were rigid, this multi-scale model successfully predicted the fretting wear simulation with evolution of interface between the debris and the substrate, which was closer to the realistic situation.

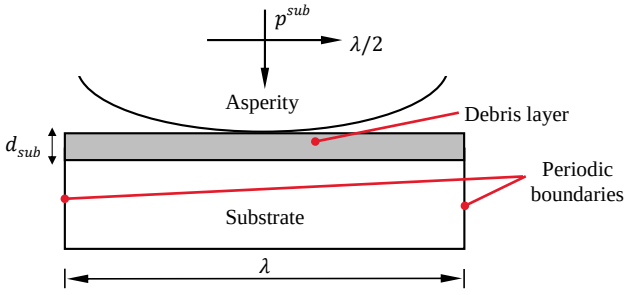

Figure 2-23. The micro model-asperity model used in multiscale modelling of fretting wear presented in [84]

Besides assuming the debris as a layer, the particle-shape debris is also imported to FE models of fretting wear. In 2011, Basseville *et al.* [85] presented a fretting wear model, explicitly including rectangular particles with fixed number as the third body, shown in Figure 2-24. The wear model implemented for both substrate and particles were based on dissipated energy method, and the link between substrate and particles was based on the conservation of matter, *i.e.* the amount of matter lost due to wear was added to the debris. Although authors simplified fretting wear process for this model, *e.g.* neglecting the oxidation, choosing the fixed number of particles and only simulating 50 wear cycles, the predicted results showed that debris might be trapped in the contact interface in partial slip condition, while they ejected from the interface when gross sliding occurred. This model provided debris movement information of fretting wear from the physical aspect.

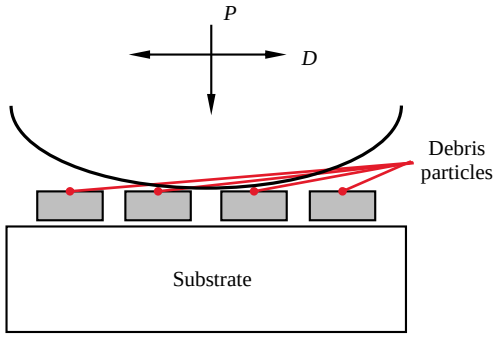

Figure 2-24. Schematic of the fretting wear model applied in [85]

More recently, an investigation of the effect of debris particles on fretting contact in partial slip was presented by Ghosh *et al.* [86]. A similar model as in Figure 2-24 but with sphere particles was used in this research. Comparing to the study of [85], they studied the effects of material properties, *i.e.* elastic plastic deformation, and number of debris particles on contact and fretting behaviours. They found that the debris particles were plastically deformed and underwent significant part of the load applied on the first bodies. In addition, they proposed that the fretting wear had no direct relation with the number of debris particles. Meanwhile, some assumptions were made for simplification, such as neglecting the evolution of fretting wear scar and keeping the stick zone size constant.

In addition to classical FEM, Benjamin D. Leonard *et al.* [87] developed a fretting wear model taking into account the effect of the third body by combining finite and

discrete element methods. In this model, FEM was employed for the calculation of substrate bodies, while the debris and contact interactions between debris and substrates were simulated by the discrete element method. In this research, they presented two geometries: a) the flow of the third body between flat rigid plates for analysing the viscous properties and b) a worn Hertzian contact due to partial slip with third body for studying contact variables of the interfaces. This model studied influence of wear particles on the stress distribution in the contact surface from particle shapes, number of cycles, *etc*. This model also made some simplifications, for instance, third body of this model was just imported in the worn surface without attending the process of fretting wear.

As it reveals from the above researches, the available studies have some limitations. For the debris model assumed as a layer, the contact interactions of interfaces between debris and first bodies are usually simplified as one rigid connection and one Coulomb's friction law, which both should be controlled by Coulomb's friction law. For the debris model with particles, the difficulty is predicting full cycles of fretting wear, *e.g.* 10,000 cycles.

Therefore, one objective of this thesis is to improve the FE model to take into account the effect of debris and to achieve better understanding of the fretting wear process. In this thesis, a FE fretting wear model with a debris layer is created, including two interfaces governed by Coulomb's friction law.

2.7 Singularity problem in contact simulation

FE simulations of fretting wear are time-consuming tasks due to its great number of cycles and high requirement of meshing in the contact zone. Therefore, it is worthy studying the optimization of computational cost without reducing accuracy of fretting wear simulations.

Most of researches employ an accelerating technique called jump cycle, firstly proposed by McColl [58] in 2004, to keep reasonable computational time. In this technique, the jump cycle factor ΔN is introduced representing that the contact variables for the wear calculation are kept constant during the next ΔN fretting wear cycles. This method have been widely used for FE fretting wear prediction, such as research of [70, 72, 80, 88].

Besides the jump cycle technique, mesh size should be another important aspect influencing simulation time and FE results. However, there is little research studying on the mesh sensitivity problem on FE fretting wear problems, investigating if the mesh size is fine enough to make stresses converged or divergence appears due to singularity.

Stress singularity is known as a phenomenon that the stress becomes infinite, which occurs due to concentrated loads or discontinuity, such as geometric discontinuity, boundary condition discontinuity or discontinuities in the material properties [89]. In fact, stress singularity does not exist in the real world, since no stress could be up to infinity. However, it could pretend as a specific value in FEM results. Therefore, it is important to recognize the presence of stress singularity in FEM results.

Sinclair in his review paper [90] grouped two types of singularity problems in elasticity: power singularity and logarithmic singularity. For power singularity, the relation between the local stress σ and the dimensionless radial distance r from a singular point can be written as:

$$\sigma = O(\sigma_0 r^{-\gamma}), as \quad r \to 0, \tag{2-29}$$

where γ is the singularity exponent.

For logarithmic singularity, this relation behaves like:

$$\sigma = O(\sigma_0 \ln r), \quad as\, r \to 0. \tag{2-30}$$

where in both Equations (2-29) and (2-30), σ_0 is the applied stress.

In order to identify stress singularity, there are two kinds of methods, namely asymptotic method and numerical method. Asymptotic method is an analytical method, which is focusing on special locations, such as the tip of a crack, the apex of a sharp notch or the corner of some slipping in complete contact. This method recognizes that the stress distribution in its adjacent zone may be the same as all other features having the same local geometry [91]. Numerical method is named as stress singularity signature proposed by Sinclair [90], identifying whether or not there is a stress singularity based on numerical results. These numerical results are checked by stress singularity signature, by which the divergence of peak stresses calculated from FE models with different mesh sizes. This numerical method have been applied in the

field of computational fluid dynamics [92] to confirm the local asymptotic identification of singularities induced by flow.

Asymptotic method has been employed in fretting fatigue problems to identify whether the threshold of stress intensity exists in order to find out whether or not fretting provides additional damage [93]. However, in the case of fretting wear, during which the contact surfaces are continuously changing, it is difficult to apply asymptotic method to distinguish stress singularity. Furthermore, as FEA is widely used in fretting wear, it will be very convenient in engineering analysis if the stress singularity could be detected by the results of numerical simulations.

Therefore, in this thesis, the singularity signature is implemented to analysis FE results of fretting and fretting wear, to improve our knowledge on mesh sensitivity and stress singularity problems in fretting and fretting wear. The detail of stress singularity signature will be discussed in chapter 3, section 3.4

2.8 Application: Fretting wear problems in fretted wires

As mentioned in section 1.2.2 , hoisting ropes is a typical example in reality suffering fretting wear.

In mine industry, during hoisting process, a hoisting rope is subjected to the cyclic axial tension load and bending stretch load on the drum and guide wheel, resulting in small relative sliding among the strands and wires[60]. Once fretting wear happens, the area of cross-section decreases and stresses increase, accelerating the wire failure of hoisting ropes. Zhang and his co-workers conducted fretting wear experiments of hoisting ropes in different displacement amplitudes [94], in dry and friction-increasing grease conditions [59] and in different corrosive mediums [95]. Based on these experimental results, it was found that fretting wear was very complex: fretting behaviour and wear mechanisms of wires were influenced by the applied displacement amplitude, normal load and mediums in interfaces.

Aiming to broaden the knowledge of fretting wear in fretted wires and further study the failure of them, researchers turn to numerical modelling, *i.e.* FEM, to investigate the detail of this process. Cruzado [8] firstly simulated the process of fretting wear in wires in a 90° crossed-cylinders configuration in 2012, then studied the influence of fretting wear on fatigue life of wires [96] in 2013. In his recent paper [97], crossed-

cylinder models of different angles under fretting condition were simulated, of which results presented good agreement with experimental data. Besides fretting model of wires, Wang [98] studied stress distribution and fretting fatigue parameters of two upscale structures, i.e. 6×19 + IWS rope and (1+6+12) strand with three layered strands to investigate the global response of ropes in axially load condition and the influence of fretting wear on fretting scar.

Although FEM could give a good agreement with experiments, the effect of material property on fretting wear has not been considered. However, assuming that the material is elastically deformed, which is usually defined in fretting wear simulations, underestimates the threshold of the relative displacement at the interface for gross sliding in theoretical value [33]. Also, due to the coupling between a high CoF and a typical tangential displacement, this high CoF is sufficient to induce plastic deformation in the contact surface [99]. Moreover, the wear coefficient calculation based on the wear scar after fretting tests and formula [98, 100] maybe not correct due to overestimating wear depth if plastic deformation occurs.

Hence, this thesis tries to fill in this research gap by investigating the effects of the elastoplastic behaviour of fretted wires on fretting wear. In particular, we attempt to compare the predicted fretting loops and fretting wear scars in the case of elastic and elastic-perfectly-plastic models.

2.9 Objectives of this thesis

Based on the introduction of Chapter 1 and the above literature review, the objectives of this thesis are briefly listed as follows:

1. Develop a general wear calculation code for FE fretting wear problems, which could be implemented in both the two dimensional (2D) line contact and the three dimensional (3D) point contact configurations.
2. Study the influence of variable CoF at the running-in stage of fretting wear.
3. Investigate debris effects of the fretting wear process. A FE fretting wear model with a debris layer is created, including two friction law controlled interfaces.
4. Study the singularity problem in fretting condition.

5. Application of this FE strategy to fretted wires, investigating effects of the elastoplastic behaviour of fretted wires in terms of fretting wear.

2.10 Concluding remarks

In this chapter, the background related to the topic "finite element analysis of fretting wear" is introduced. By this literature review, the wear model for FEM of fretting wear and the objectives of this thesis are determined. A brief summary of this chapter and its function to the work of this thesis are given in Table 2-1.

Table 2-1: Structure of this chapter and the objectives of this thesis

Topic	Content	Purpose
Contact mechanics	Hertzian contact	Verification
	Sliding contact	
Fretting	Fretting regime	Factors affecting fretting wear
	Fretting wear	
Wear model	Archard model	Selection of wear models integrated to FEM
	Energy model	
FEM in fretting wear in 2D	FEM without considering debris effects	Objective 1: effects of variable CoF on fretting wear
	FEM with debris effects	Objective 2: effects of debris layer with on the fretting wear process with two friction law controlled interfaces
Singularity	Singularity problem	Objective 3: singularity problem in fretting wear
Fretting wear in fretted wires	Fretting wear problems in fretting wires	Objective 4: study effects of elastoplastic behaviour on fretted wires in terms of fretting wear

Chapter 3 **FE modelling of fretting wear in line contact**

3.1 Overview

Due to fretting wear's micro displacement and contact area compared to the component size, and in order to investigate the details of the fretting wear behaviour, the real contact geometry is approximated to a 2D cylinder/flat line contact configuration. This configuration is widely used for studying the fretting wear behaviour of aero engine materials, such as Super S/CMV, AerMet®100 ultrahigh strength steel alloys, Inconel 718 nickel-base super alloys [58, 101] and Ti–6Al–4V [7, 102, 103].

The 2D cylinder/flat line contact FE models for fretting wear are presented in this chapter. Four models are generated:

1. Contact model
2. Basic fretting wear model
3. Fretting wear model with debris layer
4. Fretting wear model for singularity problem

Besides FE models, the evolution of CoF with fretting wear cycles and singularity signature are introduced. Meanwhile, simulation parameters of each model are listed at the end of relevant section. The FEA software ABAQUS/STANDARD was used to solve the contact fretting wear problems.

3.2 Contact model

3.2.1 **Geometry information**

Depending on different references in the literature, 2D cylinder/flat FE models with dissimilar dimensions were developed.

1. Contact model: This is the first step for fretting wear simulations and the contact pressure distribution of this step is extracted to verify FE results with Hertzian solution.
2. Basic fretting wear model: This is the simplified FE model for simulating fretting wear with a constant CoF and no debris effects.

3. Fretting wear model with debris layer: This is to analyse the effects of debris on fretting wear.
4. Fretting wear model for singularity problem: This is to study stress singularity in fretting wear.

Dimensions of cylinders and specimens are shown in Figure 3-1 (a) and listed in Table 3-1. The lateral contact length L is 10 mm for the basic model and is 3 mm for the singularity model. In order to achieve accurate stress distributions in the contact zone and efficient computational time, both cylinder and specimen of each FE model are partitioned into the contact zone and the non-contact zone for meshing. Figure 3-1 (b) shows the refined mesh of the contact zone. Four-node, plane strain linear elements (CPE4) are employed with the mesh size 5 μm × 10 μm in the contact zone of FE models, except models for singularity problems. The transition from fine mesh to coarse mesh of the non-contact zone is produced by controlling the seed density in a bias algorithm.

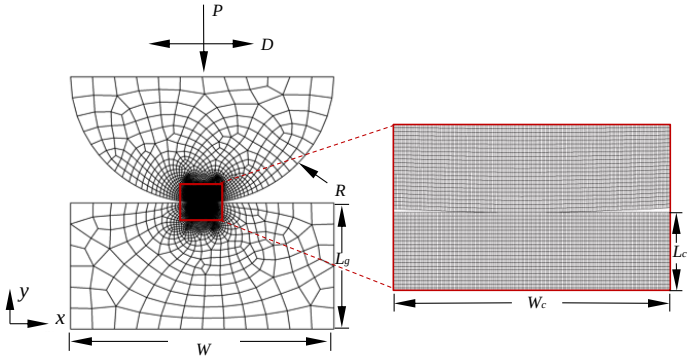

(a) (b)

Figure 3-1. The line contact model for fretting wear: (a) the global scale with dimensions and (b) the local refined mesh at the contact zone

Table 3-1: Dimensions for 2D models

Model	***R*** **[mm]**	***W*** **[mm]**	***L*** **[mm]**	L_g **[mm]**	W_c **[mm]**	L_c **[mm]**	**Reference**
Basic model	6	12	10	6	1.2	0.6	[58]
Singularity model	10	20	3	10	2	0.3	[71]

3.2.2 **Loading conditions**

As shown in Figure 3-1, a constant normal load *P/L* is applied on the mid-point of the top surface of the cylinder. This mid-point and the top surface are tied together by the Multi-Point Constraint (MPC) technique to make their active degree of freedom equal, avoiding the unrealistic excessive deformation due to the applied concentrated normal load [104].

For the contact model, only one loading step is required to exert the constant normal load at the mid-point at the top surface of the cylinder. At this step, only the vertical motion of the cylinder is allowed. Other global displacements and rotations are constrained. The contact pressure distribution is achieved after calculation of this step.

3.2.3 **Contact interaction**

Surface to surface, master-slave technique is used for the contact discretization. The bottom surface of the cylinder is defined as master surface, while the top surface of specimen is defined as slave surface. By this setting, the contact variables of specimen could be easily extracted and used for the subsequent wear calculation.

Contact properties of the interface are of great importance in fretting wear analysis. The Coulomb's friction law with isotropic friction is defined as the tangential behaviour. The hard contact is defined as the normal behaviour. The Lagrange multipliers is employed as the constraint enforcement to solve the contact problem. Alhough using the Lagrange multipliers increases the computational cost due to generating extra degrees of freedom in the contact calculation, it could achieve the exact relative slip in the contact surface rather than using penalty method. The finite sliding formulation is used for the contact tracking.

3.2.4 **Simulation parameters**

The parameters of the FE contact model for verification with Hertzian contact solution are listed in Table 3-2.

Table 3-2: Simulation parameters for the FE contact model

Material property			Loading condition	
E [GPa]	ν	σ_{yield} [MPa]	P [N]	μ
200	0.3	1240	185	0.9

3.3 Basic fretting wear model

3.3.1 **Energy model in FEM simulations**

As mentioned in section 2.5 , energy method is applied as the wear model for the fretting wear prediction in this thesis. In this section, the implementation of energy model to FEA is introduced.

The relationship between the fretting wear volume V of the specimen and the frictional work during the whole fretting wear process is defined as [68]:

$$V = K_E \sum_{i=1}^{N} 4\mu_i P_i \delta_i, \qquad (3\text{-}1)$$

where K_E is the energy wear volume coefficient of the studied interface for a given sliding amplitude, and N is the total number of fretting wear cycles. During the i^{th} fretting cycle, the increment of the wear depth, Δh_i, for the specimen at x position is given by:

$$\Delta h_i(x) = K_{El} E_{di}(x) = K_{El} \int_{t=0}^{T} q_i(x)\, ds_i(x) \qquad (3\text{-}2)$$

where K_{El} is a local energy wear coefficient, $E_{di}(x)$, $q_i(x)$, $ds_i(x)$ are the dissipated energy, the shear stress and the relative slip at x position at the i^{th} fretting cycle with a period T, respectively. K_{El} is a dimensional coefficient with the unit MPa^{-1}. Theoretically, it should be calculated from the transient contact pressure, relative slip of the contact δ and wear volume. However, from experiments, the position measuring relative displacement is far from contact surface. The measured δ_E contains the effect of stiffness of the test rig and the elastic deformation of contact bodies. Therefore, K_{El}

is called local wear coefficient due to the use of the local relative displacement δ at the contact instead of the measured δ_E.

In FE calculations, the discretization of a period T leads Equation (3-2) to:

$$\Delta h_i(x) = K_{El} E d_i(x) = K_{El} \sum_{j=1}^{N_{int}} q_{ij}(x) ds_{ij}(x), \quad (3\text{-}3)$$

where $q_{ij}(x)$ and $ds_{ij}(x)$ are the shear stress and the relative slip at the j^{th} increment of the i^{th} fretting wear cycle, and N_{int} is the number of increments of the i^{th} fretting wear cycle.

Given to tens of thousands fretting wear cycles in experiments, it is not efficient and practical to simulate each fretting wear cycle explicitly in FEM. In order to reduce computation time, jump cycle concept is employed here. Therefore, the incremental wear depth during the j^{th} increment of the i^{th} jump cycle could be calculated as:

$$\Delta h_{ij}(x) = \Delta N K_{El} q_{ij}(x) ds_{ij}(x), \quad (3\text{-}4)$$

Indeed, ΔN affects the convergence of a fretting wear simulation. The convergence problem exists with a higher ΔN, and the computation cost increases when decreasing ΔN. To balance the efficiency and accuracy of FE fretting wear models, ΔN is in a range between 100 and 1000 depending on the specific objective in this thesis.

Hereby, the updated vertical coordinate of the top surface of the specimen at x position at the j^{th} increment of the i^{th} jump cycle is:

$$y_{ij}(x) = y_{ij-1}(x) - \Delta h_{ij}(x), \quad (3\text{-}5)$$

where $y_{ij}(x)$ is the vertical coordinate of the top surface of specimen at position x at the j^{th} increment of this jump cycle. Equations (3-4) and (3-5) are repeated until the total number of wear cycles is reached.

3.3.2 **Fretting wear calculations in ABAQUS**

Surface evolution induced by fretting wear could be achieved by arbitrary Lagrangian-Eulerian (ALE) adaptive meshing method in ABAQUS. ALE is a technique that makes

it possible to maintain a high-quality mesh during an analysis, by allowing the mesh to move independently of the material [104].

For the fretting wear simulation, two regions should be defined: a) the node set of contact surface, called ALE nodes, which are directly controlled by the wear calculations and b) the ALE domain, of which domain the meshes are modified by the ALE method in ABAQUS. In all fretting wear models of this thesis, the surface nodes in the contact zone of the specimen are defined as ALE nodes and the contact zone of the specimen is assigned as ALE domain. This arrangement is shown in Figure 3-2.

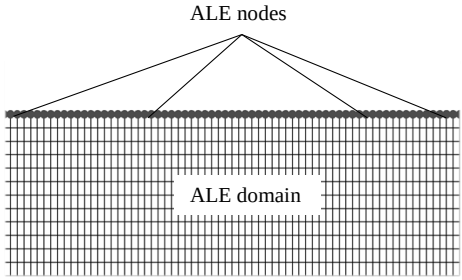

Figure 3-2. ALE nodes and the ALE domain of the specimen for fretting wear model in ABAQUS

UMESHMOTION subroutine of ABAQUS is called at the end of each increment of cycle jump to realize the evolution of the profile in contact surfaces. This subroutine constrains the motion of ALE nodes and ALE domain by two steps as following:

1. The local wear depth calculation: At the end of every increment of each jump cycle, the available nodal or material point information is obtained from the converged structural equilibrium equations. Based on Equation (3-4), the local incremental wear depth is calculated.
2. Motions of ALE nodes and nodes in the ALE domain governed by the adaptive meshing algorithm: This algorithm consists of two steps:
   a) Sweeping: adjust nodes to new positions depending on the adjacent nodes during the previous mesh sweep.
   i. For the ALE nodes, the vertical coordinates of the ALE nodes are updated by Equation (3-5).

ii. For nodes of the ALE domains and the horizontal coordinates of ALE nodes, the govern equation is:

$$x_{k+1} = N^N x_k^N \qquad (3\text{-}6)$$

where x_{k+1} is the new position of the node, x_k^N is the neighbouring nodal position obtained at the k^{th} sweeping. N^N is the weight function obtained from one or a weighted mixture using one of the following methods: original configuration projection (default in ABAQUS/Standard) and volume smoothing. In this thesis, the default method is employed.

b) Advection: solved variables are remapped from the old mesh to the new mesh.

After these two steps, the new profile is created and the program starts the FE calculation of the next increment, as shown in Figure 3-3.

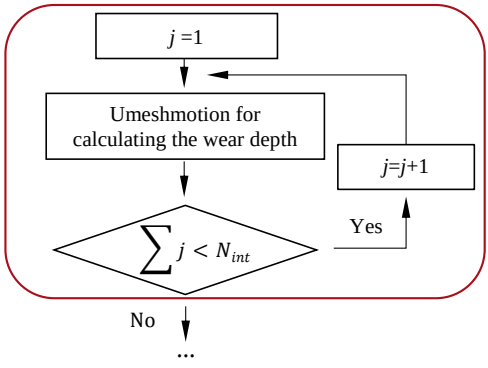

Figure 3-3. The wear depth calculation during one jump cycle by Umeshmotion

3.3.3 **Loading history**

Figure 3-4 illustrates the loading process in fretting wear FE models. The first step is the loading step, which is the same as the contact model described in section 3.2 . Subsequently, a horizontal reciprocated displacement with the amplitude *D* is exerted at the mid-point of the top surface of the cylinder, of which steps are defined as moving steps. During these moving steps, the motions along *x* and *y* directions of side edges and the bottom of the specimen are still constrained. The number of moving steps are

calculated from the total number of cycles N divided by the jump cycle ΔN. After finishing all moving steps, the constant normal load P is unloaded to remove the elastic deformation and extract the fretting wear profile as the result of the dissipated energy.

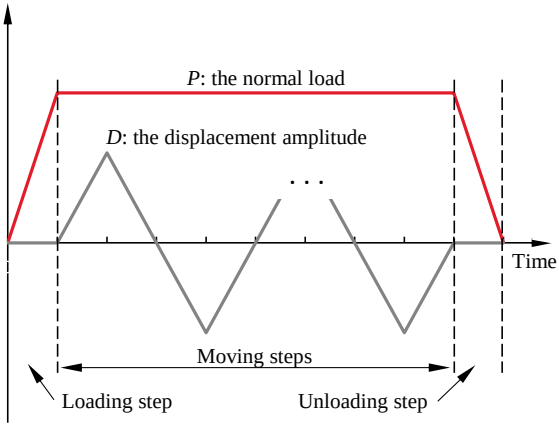

Figure 3-4. The loading history for 2D fretting wear models

3.3.4 **CoF curve**

In most FE simulations of fretting wear, CoF is assumed as a constant in which case both Archard and energy model bring out same results. However, as shown in Figure 3-5 taken from [58], at the beginning of fretting wear, it is running-in stage and CoF increases significantly with time during the first thousands cycles in both normal load cases, *i.e.* 185 N and 500 N. During the fretting wear experiment, the contact surface, relative displacement and the third body affect the evolution of CoF. Therefore, in order to study the fretting behaviour of the running-in stage, a variable CoF should be considered.

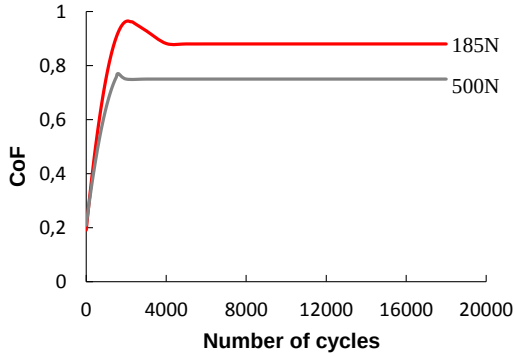

Figure 3-5. The evolution of CoF during the process of fretting wear under various normal loads, D = 25 μm [58]

To obtain the relation between CoF and the number of fretting wear cycles, CoFs of 185 N and 500 N were extracted and best-fit curves were constructed, as illustrated in Figure 3-6 (a) and Figure 3-6 (b), respectively. Since the purpose of the best-fit curves is to achieve the most accurate formulation describing this relation, the value of R^2 is the only factor considered. Thus, it is a polynomial relation in which case R^2 is most close to 1.

When the applied normal load is 185 N, the best fit function, $R^2 = 0.989$, is:

$$CoF = (-1.784) \times 10^{-7} N^2 + 0.000743N + 0.191266 \quad (3\text{-}7)$$

When the applied normal load is 500 N, the best fit function, $R^2 = 0.985$, is:

$$CoF = (-1.428) \times 10^{-7} N^2 + 0.000579N + 0.2094 \quad (3\text{-}8)$$

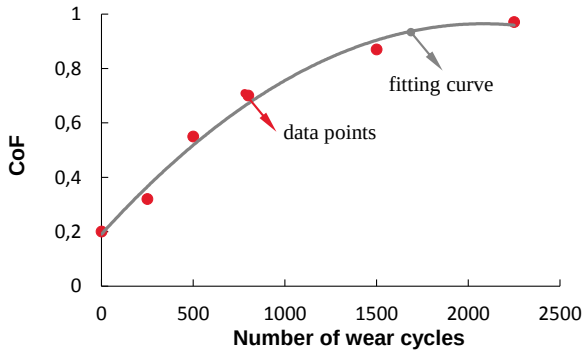

(a)

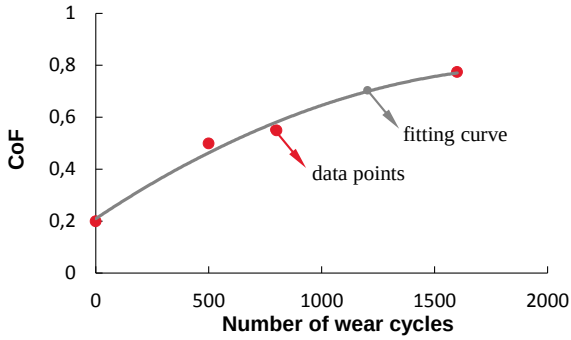

(b)

Figure 3-6. The best fit curves of CoF versus the number of cycles of 2D models: (a) P = 185 N and the number of cycles up to 2,500 cycles and (b) P = 500 N and the number of cycles up to 1,600 cycles, based on Figure 3-5

3.3.5 **The process of the fretting wear simulation**

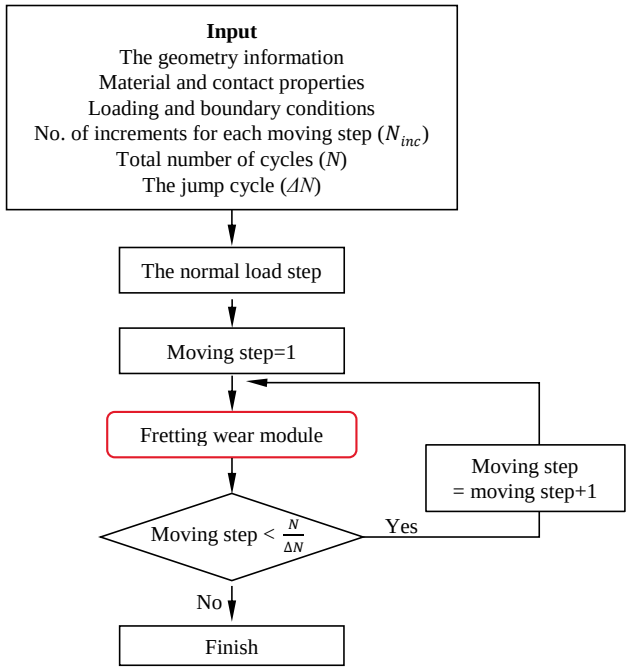

Figure 3-7. The flowchart for fretting wear simulations. The fretting wear model is described as Figure 3-3.

3.3.6 **Simulation parameters**

Both FE fretting wear models with a constant CoF and a variable CoF are created.

Same material as for the contact model presented in section 3.2.4 is used, of which E = 200 GPa and υ = 0.3. Only elastic deformation is considered here.

The total number of fretting wear cycles is 18,000. For the basic fretting wear model, the jump cycle is 1,000 with a fixed number of 100 increments in each moving cycle. For the study of the variable CoF, in order to capture the evolution of CoF as a function of the number of cycles in the running-in stage (the first 2,500 cycles), a jump cycle with 100 is used in both constant and variable CoF cases. In the subsequent stage, jump cycle of 1,000 is used. In both jump cycle cases, the number of increments for each moving step is fixed to 100 as the basic fretting wear model. Simulation parameters for the fretting wear calculation are shown in Table 3-3. K_A is the Archard wear coefficient taken from [58] and K_E is the energy wear coefficient calculated based on Coulomb's friction law. K_A and μ are taken from the steady stage of the fretting wear test in [58].

Table 3-3: Simulation parameters for basic fretting wear models

P [N]	μ	K_A [$\mathrm{MPa^{-1}}$]	K_E [$\mathrm{MPa^{-1}}$]
185	0.9	3×10^{-8}	3.33×10^{-8}
500	0.75	5.5×10^{-8}	7.33×10^{-8}
1670	0.68	3×10^{-8}	4.41×10^{-8}

3.4 Fretting wear model for singularity problem

3.4.1 **Singularity signature**

For numerical simulations, stress singularity is detected by the divergence of the peak stress values from numerical results. Evidence of the divergence requires a suitable refined sequence of discretization of modelling. As described in section 2.7, in elasticity, stress singularity can be divided into two types, namely power singularity and logarithmic singularity. According to results by models with different mesh sizes, types of singularity can be identified by the following formulas [105].

For power singularity, the relation between the local stress σ and the dimensionless radial distance r from a singular point can be written as:

$$\sigma = O(\sigma_0 r^{-\gamma}), as \quad r \to 0, \tag{3-9}$$

where σ_0 is an applied stress and γ is a singularity exponent. For numerical simulations, series of mesh sizes is defined based on the finest mesh size z and the scale factor λ of scaling mesh size as:

$$z, \lambda z, \lambda^2 z, \tag{3-10}$$

Employing the sequence of Equation (3-10) in (3-9) yields:

$$\frac{\sigma_m}{\sigma_c} \sim \frac{\sigma_f}{\sigma_m} \sim \lambda^{\gamma}, \quad as \quad z \to 0, \tag{3-11}$$

where c, m and f mean the coarse mesh, the middle mesh and the fine mesh, respectively. Therefore, the singularity exponent can be calculated as:

$$\gamma_c = \frac{[\ln \sigma_m/\sigma_c]}{\ln \lambda}, \quad \gamma_m = \frac{[\ln \sigma_f/\sigma_m]}{\ln \lambda} \tag{3-12}$$

The power singularity is present when:

$$\frac{2|\gamma_c - \gamma_m|}{\gamma_c + \gamma_m} < 0.1 \tag{3-13}$$

It means that a power singularity is present when the change of the singularity exponent is less than 10 % of its average value. Equation (3-12) has been demonstrated to be effective by numerical experiments of the stress analysis, of which 92% of power singularity problems have been identified based on this method as reported in [105].

For logarithmic singularity, the relation between the local stress σ and the dimensionless radial distance r from a singular point should be:

$$\sigma = O(\sigma_0 \ln r), \quad as\, r \to 0. \tag{3-14}$$

Successive estimates of the increment in the peak stress are written as:

$$\Delta\sigma_c = \sigma_m - \sigma_c, \Delta\sigma_m = \sigma_f - \sigma_m. \quad (3\text{-}15)$$

The singularity can be judged as logarithmic singularity when:

$$\frac{2|\Delta\sigma_c - \Delta\sigma_m|}{|\Delta\sigma_c + \Delta\sigma_m|} < 0.1, \quad (3\text{-}16)$$

which also has been verified by numerical experiments of the stress analysis presented in [105].

Based on the stress singularity signature, both power singularity and logarithmic singularity could be identified. Logarithmic singularity is the weakest type of stress singularity and separates the regions of no stress singularity and power stress singularity [106]. In the case of power singularity, the stresses are meaningless and further refinement of FE models will be useless, as no meaningful results will be produced. However, if a log singularity takes place, results of singular point location is not acceptable.

As fretting wear simulation is time consuming with high requirement of the mesh size, it is interesting to study the influence of the mesh size on the results of fretting wear. Therefore, the stress singularity signature is applied here to identify whether singularity occurs or not at fretting wear conditions.

The sequence of mesh sizes recommended is *z, 2z, 4z*. This means that at least three analyses are required using different mesh sizes for a given model. In this study, the mesh sizes: 5 μm, 10 μm and 20 μm in the contact zone are employed.

3.4.2 **Loading history**

Two types of loading history are introduced to investigate the mesh sensitivity of FE fretting wear models, as shown in Figure 3-8.

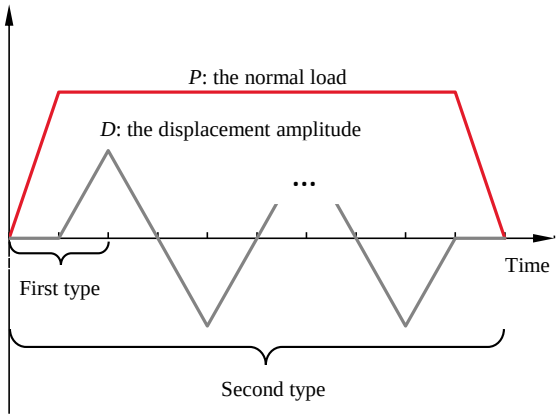

Figure 3-8. The loading history for the singularity study

1. In the first type of the loading history, two loading steps are defined. The first step is for imposing a constant normal load *P* and the second step is for exerting *x*-direction displacement of amplitude *D* on the cylinder to the right most. This type of loading history is only simulating a quarter of one fretting cycle in order to identify whether or not the applied displacement or CoF has influence on the mesh sensitivity.
2. The second type of loading history is simulating the whole process of fretting wear. A total number of 20,000 fretting wear cycles is considered and jump cycle of 2,000 is chosen to balance the efficiency and accuracy of FE calculation. This type of loading history consists of 12 loading steps (ten moving steps and the loading/unloading steps). The purpose of this loading type is to study whether the wear profile of contact surfaces is a significant factor to change the mesh sensitivity of FE fretting wear simulations.

3.4.3 **Simulation parameters**

In both loading histories, the normal load *P* was kept constant at 400 N. The applied displacement amplitude *D* and the used CoFs are listed in Table 3-4 according to loading history types.

Table 3-4. Loading conditions of FE fretting wear models for the singularity study

Loading history	***D* [μm]**	***μ***	**Parameters to study**
First type	4, 5, 6, 7, 15	0.8	Displacement
	7,15	0.6, 1	CoF
	4	1.5, 2, 2.5	CoF
Second type	4, 15	0.8	Number of cycles in fretting wear

For the first type of the loading history, three situations are considered:

1. CoF is kept constant at 0.8, while the displacement varies as 4 μm, 5 μm, 6 μm, 7 μm and 15 μm to cover partial slip and gross sliding regimes. In these conditions, the effects of displacement amplitude are studied.
2. In gross sliding regime, *i.e.* the applied displacement amplitude reaches 7 μm, μ = 0.6 and 1 are considered to study the effects of CoF.
3. Under the partial slip condition, the applied displacement amplitude is kept 4 μm. Higher CoFs of 1.5, 2, 2.5 are applied to identify how the stress singularity signature changes. It is worth mentioning that CoF depends strongly on the experimental conditions. It has been reported in [65] that: in high vacuum condition, CoF between contact of clean metals could be 2 to 10 or even more due to the strong metallic bonds forming across the contact surfaces. On other hand, large values of CoF are used to simulate large stick region and approach a fully stick condition.

In the second loading history, the CoF is kept as 0.8 and the applied displacement amplitudes are 4 μm and 15 μm, in which condition is partial slip and gross sliding regimes, respectively, in order to investigate which condition plays more important role in stress singularity during the fretting wear process.

Ti-6Al-4V is selected as material for both the cylinder and the specimen. Material properties for Ti-6Al-4V are: E = 121 GPa and ν = 0.29. Based on the experimental study, K_E is assumed to be 1.12×10^{-8} MPa^{-1} in all singularity simulations. All this material properties and the wear coefficient are taken from [71].

3.5 Fretting wear model with debris layer

In this section, an FE cylinder/flat model with a debris layer (debris layer model) is constructed to study its effects on the contact stress distribution and the wear profile during fretting wear.

The reasons of assuming a debris layer are listed as follows:

In the study of [107], fretting wear experiments of cylinder/flat contact for steel were implemented. It is found that the wear debris was flake-like and was mainly Fe_2O_3. It was also mentioned that the contact surface layer of the flat specimen contained an oxide layer and matrix material. Based on experimental results, authors of this work proposed that the oxidation on the contact surface was striped layer by layer during fretting wear.

In reference [61], fretting wear tests of steel sphere/flat contact were carried out. As discussed by authors, at the early stage of fretting wear, the high contact pressure led to the compaction of debris particles. Thereby, an oxidized debris layer was generated at the interface between the contact surface of ball and the bare metal surface of the specimen.

In reference [108], fretting tests were accomplished to study the effects of contact geometry on fretting wear rates and mechanisms for cylinder/flat contact. Figure 3-9 shows that the metallic debris layer exists at the contact surface of the cylindrical specimen, with imposed displacement amplitude of 100 μm. When imposed displacement amplitude decreasing to 25 μm, the debris layer contained two sub-layers, as shown in Figure 3-10. The contrast indicates the difference in oxygen content of these sub-layers. These images reveal that the magnitude of imposed displacement amplitude has impact on the composition of debris layer.

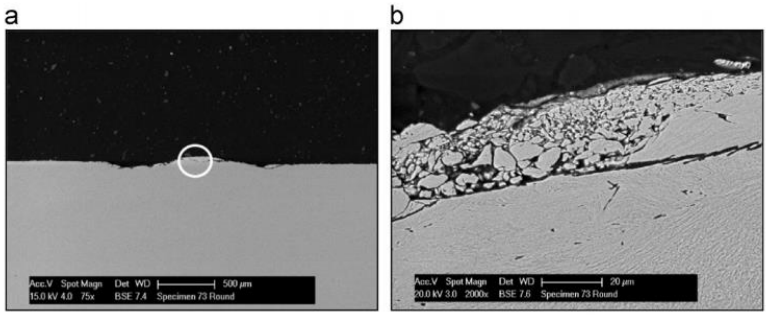

Figure 3-9. BSE images of a cross-section through the transferred material of the cylindrical specimen. P = 450 N, D =100 µm, R =160 mm, taken from [108]

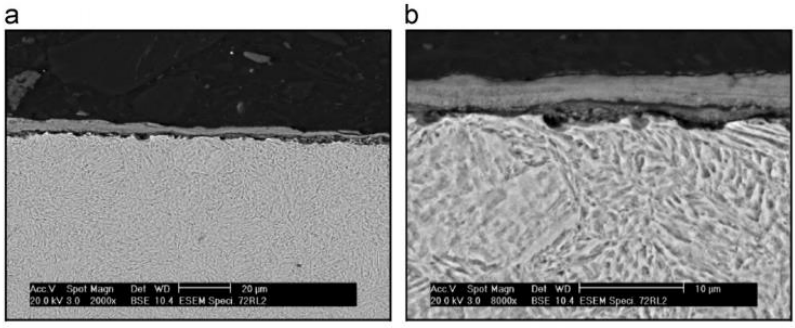

Figure 3-10. BSE images of a cross-section through the transferred material of the cylindrical specimen. P = 450 N, D =25 µm, R =160 mm, taken from [108]

Based on the experimental observation and discussion of [61, 107, 108], the debris particles are compacted as a layer due to the high contact pressure. Therefore, we assume that the debris is a layer of Fe_2O_3.

3.5.1 **Geometry information and contact interactions**

A FE fretting wear model without a debris layer presented in section 3.3 is used here for providing the wear profiles as the surface geometry of the debris layer in the debris layer model. The debris layer model is generated by importing the debris layer with the same profile as the relevant contact surface of the specimen after 500, 1,500 and 2,500 fretting wear cycles presented in Figure 3-11, respectively.

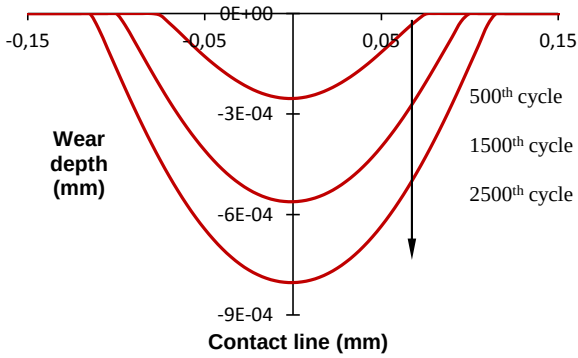

Figure 3-11. Top surfaces of the specimen used in the FE model with debris layer, after different number of cycles

Based on the experimental study in [101], the thickness of the debris layer is not kept constant or changes monotonically during the process of fretting wear. Therefore, the effect of thickness is also studied here. Since the evolution of thickness of the debris layer during fretting wear is difficult to measure during experiments. Hence, in this study, the thickness of the debris layer t is assumed 5 µm, 10 µm and 20 µm. Although these values of thickness are much larger than the predicted wear depth, two reasons of this thickness assumption are listed as follows:

1. The objective of this model is to investigate the influence of the debris thickness on fretting wear. In the experiment of reference [49], the artificial third body layer was deposited between the first bodies before experiments. After the experiments, the measured layer thickness is 10-15 µm.
2. Although no wear damage is assumed in the pad, the contribution of the pad to the debris layer is considered.

Same global dimensions are used in this debris layer model as show in Figure 3-12. The loading condition is: P = 185 N with the horizontal cyclic displacement amplitude D = 25 µm. The total fretting wear cycle is 18,000 cycles. The mesh size of contact surfaces in first bodies (the cylinder and the specimen) is 5 µm. The mesh sizes for the debris layer are 5 µm × 2.5 µm for t = 5 µm and 5 µm × 5 µm for the other two thickness cases, respectively.

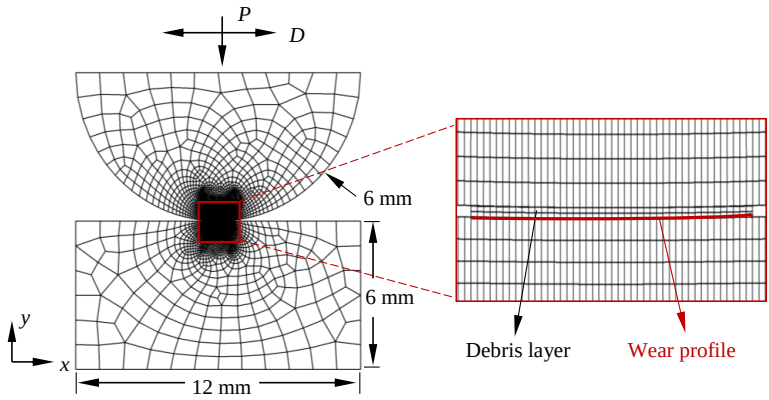

Figure 3-12. The fretting wear model with the debris layer: (a) the global scale with dimensions, (b) the local contact configuration at the contact zone

In this debris layer model, two contact interfaces are created: a) the contact surface between the cylinder and the debris layer, and b) the contact surface between the debris layer and the specimen. It is difficult to measure CoFs between these two interfaces separately by experimental measurements. However, CoF also is one of the most important parameters to determine the fretting behaviour and the wear extent. In this study, CoF between the cylinder/the debris layer (Top) interface is assumed 1 and CoF between the debris layer/the specimen (Bottom) interface is taken as 0.88 based on the experimental data from [58]. Usually, the debris of metallic fretting wear is metallic oxide that is harder than the first bodies; therefore, the top and bottom surfaces of the debris layer are defined as master surfaces for the Top interface and Bottom interface, respectively. These descriptions for contact interactions are also shown in Figure 3-13. For both interfaces, the tangential behaviour is constrained by the Lagrange multipliers method.

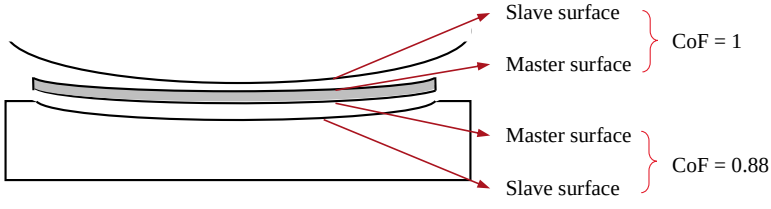

Figure 3-13. Contact interactions of the debris layer model

Several assumptions exist in this layer model:

1. Only elastic deformation of the debris layer is considered in this model. However, the elastic-perfectly-plastic deformation is taken into account for first bodies.
2. The debris layer covers the whole wear profile. Therefore, the width of the debris layer changes based on the wear width of wear scars. The thickness of it in a given debris layer model does not change during the simulation.
3. Material properties of the debris layer are homogeneous.

3.5.2 **Implementation of the fretting wear model with the debris layer**

The fretting wear process with a debris layer is simulated following a flowchart in Figure 3-14.

1. The wear profile predicted by the model without debris layer after certain cycles is imported as the initial geometry in the debris layer model.
2. The normal load *P* is applied at the mid-point of the top surface of the cylinder followed by the fretting wear simulation with a debris layer. The effect of debris is simulated explicitly only for the next 500 wear cycles of the debris layer model and the influence of the debris layer is recorded in the evolution of the wear scar of the specimen.
3. Finally, the wear profile calculated by the debris layer model is imported to the next wear simulation without debris layer. Then, fretting wear is calculated with a jump cycle of 1000 and 100 increments in every moving step, until the number of cycles reaches the final number of wear cycles, which is 18,000 cycles.

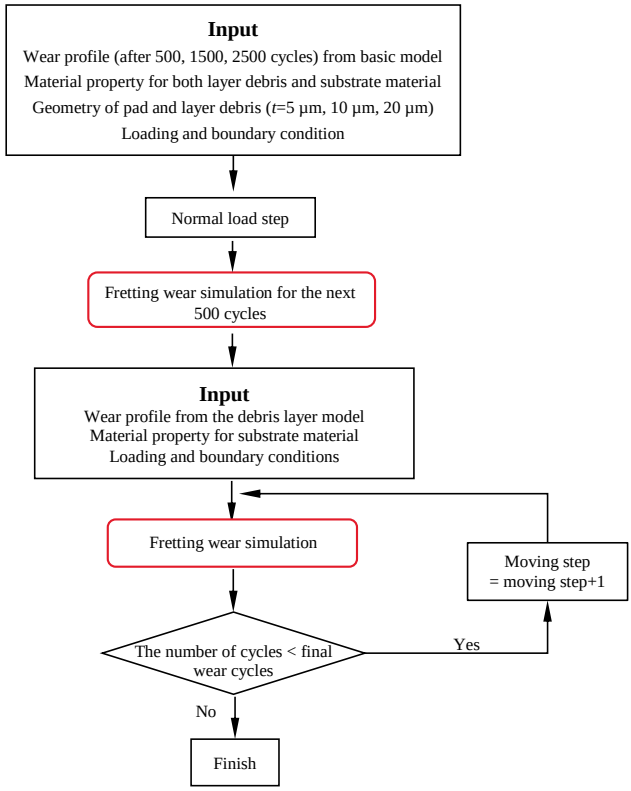

Figure 3-14. The flowchart of fretting wear simulations with effects of the debris layer

3.5.3 **Simulation parameters**

Before investigating effects of the debris layer on fretting wear, the layer contact problem without wear damage is solved. In this case, the influence of the debris layer's Young's modulus and thickness on contact pressure distribution is studied. Material properties for the debris layer are given in Table 3-5.

Table 3-5: Material properties for the debris layer

***E* of the debris layer [GPa]**	***t* [μm]**
120, 200, 280, 360	5, 10, 20

3.6 Concluding remarks

In this chapter, different cylinder/flat FE models are introduced, including the line contact model, the basic fretting wear model, the fretting wear model with a debris layer, and the fretting wear model for singularity study. For each model, the geometry information, loading histories and simulation parameters are presented. The study objectives of each model are listed in Figure 3-15.

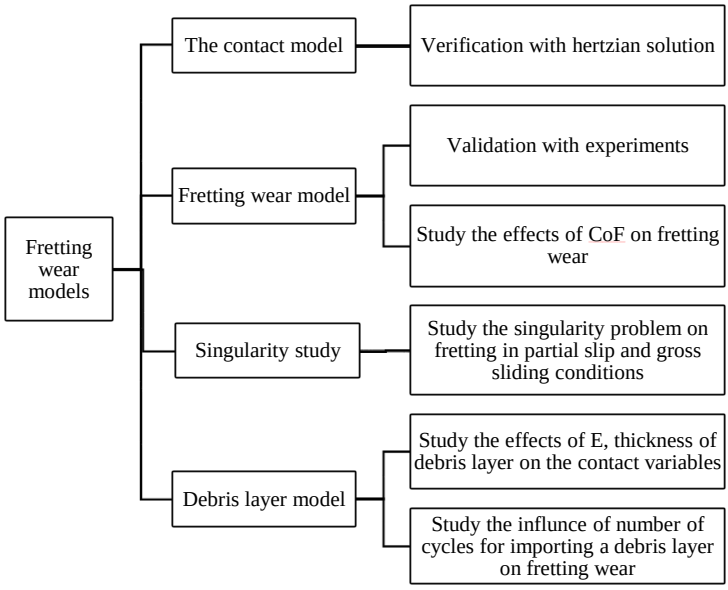

Figure 3-15. The FE models using for the fretting wear study of this thesis

Chapter 4

Numerical results of line contact configuration

4.1 Overview

In this chapter, we present the results of FE models described in Chapter 3. Firstly, the FE contact model is verified with Hertzian contact solution to ensure proper mesh size for the fretting analysis. Secondly, the results of the singularity signature are reported taking into account different applied displacements, CoF of the contact interface and fretting wear cycles. Then, the FE wear scars are compared with experimental ones [58]. Finally, the FE results of fretting wear model with variable CoF and a debris layer are presented, respectively.

4.2 Verification with Hertzian contact solution

A satisfactory converged FE model is the prerequisite of obtaining accurate stresses and relative slips in fretting wear calculation. Therefore, the theoretical solutions of Hertzian contact [25] were employed to verify the FE models presented in chapter 3 after the first loading step, *i.e.* the loading step shown in Figure 3-4. Based to Hertzian solution, the contact pressure distribution along the contact line is given by:

$$p(x) = \frac{2P}{\pi L b^2}(b^2 - x^2)^{1/2} \qquad (4\text{-}1)$$

where b is the half contact width which could be calculated by:

$$b^2 = \frac{4PR}{\pi EL} \qquad (4\text{-}2)$$

The peak contact pressure P_{max} appears at centre of the contact line, which could be expressed by:

$$P_{max} = \sqrt{\frac{PE}{\pi RL}} \qquad (4\text{-}3)$$

Figure 4-1 shows a comparison between Hertzian solution and unworn FE results of contact pressure distribution along the contact line, in which case P = 500 N and the mesh size of the contact zone is 5 μm in this FE model. For analytical results, $P_{max} = 539.9$ MPa , $b = 0.059$ mm ; while $P_{max} = 540.3$ MPa and $b = 0.06$ mm were calculated by FEA. It can be seen that FE results are in agreement with analytical

results. Since the initial contact width is as large as 24 times as the mesh size of the contact line, this FE model could capture the variation of contact stress accurately.

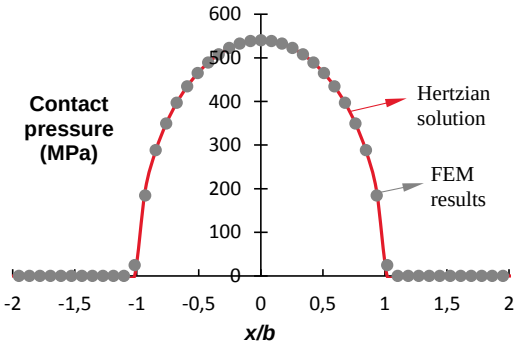

Figure 4-1. Verification with Hertzian solution, P = 500 N, R = 6 mm, L = 10 mm, E = 200 GPa and $\nu = 0.3$

4.3 Validation and verification of FE fretting wear models

4.3.1 **Validation with experimental results**

In this thesis, only the contact surface of the specimen is updated based on the wear calculation. There are two reasons:

1. According to experimental results from reference [58], more wear damage occurs at the specimen. A possible reason is that the nitrided surfaces of specimens were harder than surfaces of cylinders that were not nitrided. Thus, the oxidized debris was trapped at the contact surface of cylinders as a protection for a softer surface.
2. The wear profile obtained by the FE model presented in this thesis is compared with the results of reference [58] calculated by Archard model of both contact surfaces. The difference is limited, as shown in Figure 4-2.

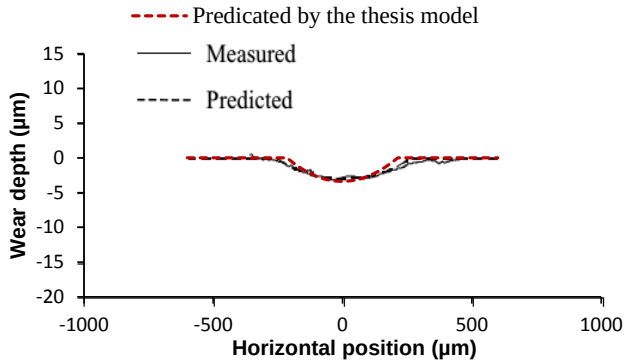

Figure 4-2. Comparison of wear scars predicted by different models and experiments, P = 185 N, D = 25 μm, N = 18,000 cycles. The original figure is taken from [58]

Next, the changes of contact profile during the wear process based on the loading condition presented in [58] are shown in Figure 4-3.

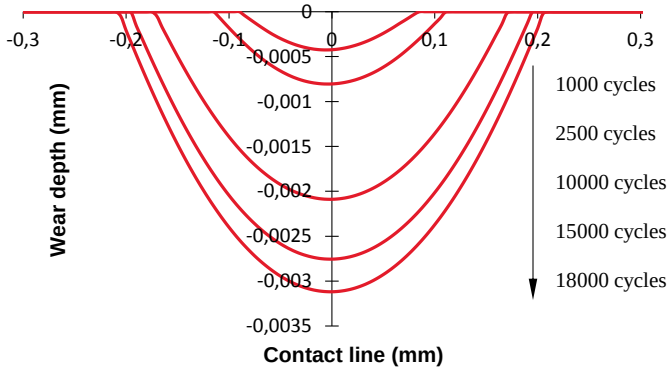

Figure 4-3. The evolution of the wear scar during the wear process. P = 185 N, D = 25 μm, ΔN = 500, K_E =$3.3 \times 10^{-8}\text{MPa}^{-1}$

Figure 4-4 illustrates the predicted values of the scar width and the maximum scar depth. FE results based on energy model are compared with experimental results. The results of experiments are taken from reference [58].

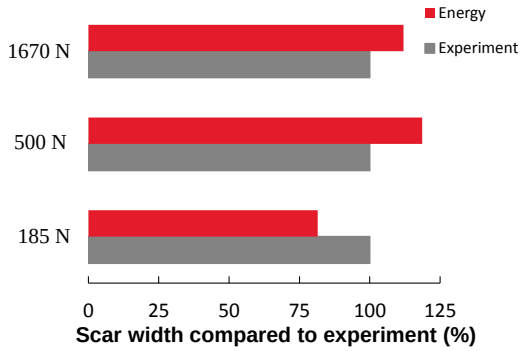

(a)

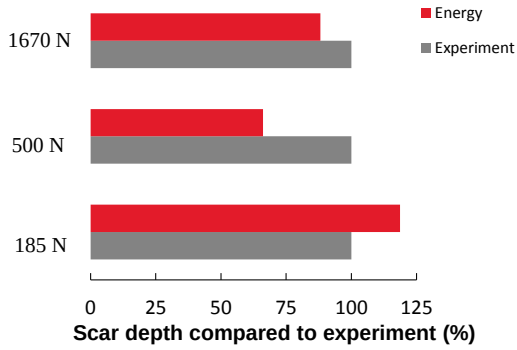

(b)

Figure 4-4. Comparison of wear scars between FE model and experiments, P = 185 N, 500 N and 1670 N, respectively. R= 6 mm, D = 25 μm. (a) scar width and (b) scar depth

When P = 185 N, wear width is 81% of the experimental one, and it is 18% more than the experimental wear depth. However, the comparison presents opposite tendency when P increases to 500 N and 1670 N. The wear width is overestimated by 18% and 12%, respectively, and the wear depth is less by 34% and 12%, respectively.

The reason for these significant differences between FE results and experiments is using global wear coefficient instead of local wear coefficient. The calculated global wear coefficient K_E is based on the relative slip δ_E between the cylinder and the specimen. Based on energy model, K_E could be obtained by:

$$K_E = \frac{V}{4N\mu\delta_E P} \quad (4\text{-}4)$$

δ_E was measured during the fretting wear experiment. However, the measuring point of δ_E is far from the contact surface comparing to the local deformation occurring in the contact surface. In this case, δ_E is the sum of the relative slip in the contact surface δ and the elastic deformation between the contact point and the measuring point of δ_E. Thus, the calculated K_E is less than the local wear coefficient K_{El}. When increasing the normal load P, δ_E may be kept constant, but δ is decreased since more contribution of δ_E is used for the system compliances. In this case, K_{El} in higher normal load condition is greater than that in the lower normal load condition. This is a possible reason. Meanwhile, the roughness of contact surfaces, effects of debris and also variable CoF are not considered in this model.

4.3.2 **Verification with other FE models**

The wear scar predicted by the FEM presented in this thesis is verified by the method described in the reference [80]. The contact configuration is same as the basic model listed in Table 3-1. The total number of wear cycles is 100,000 cycles and jump cycle is 2,000 with 100 increments of each moving step. As shown in Figure 4-5, with increasing the number of wear cycles, both the wear width and wear depth gradually enlarge. Meanwhile, the wear scar achieved by the FEM here is in good agreement with the reference results, in both interval wear scars and the final wear scar. This means that the FEM employed here could simulate fretting wear stably.

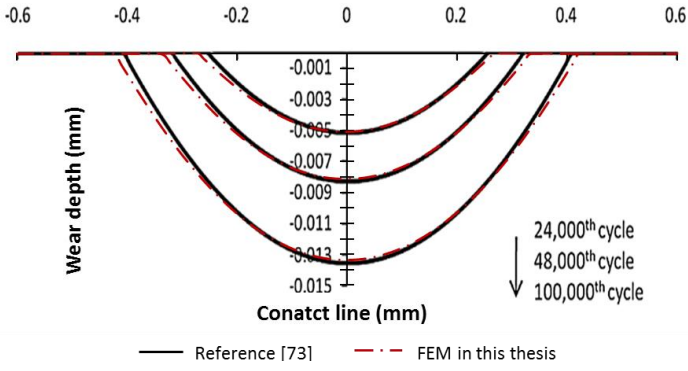

Figure 4-5. Comparison of wear scars with reference [80]. P = 500 N, D = 40 μm, μ = 0.9, K_E =1.12 × 10^{-8}MPa^{-1}.

4.4 Singularity in fretting wear simulation

Although results of the FE contact model is in agreement with Herztain solution, the mesh sensitivity study for the FE fretting contact should also be considered. As the contact status is different in partial slip regime and gross sliding regime, mesh sensitivity may also be various. Therefore, the range of partial slip and gross sliding in a given condition, *i.e.* P = 400 N and μ = 0.8, is studied.

The variations of the relative slip and shear stress under different displacement amplitudes of the first loading history type are shown in Figure 4-6 (a) and (b), respectively. It can be seen that partial slip occurs when the displacement amplitude is less than 7 µm, where the relative slip exists at the contact edges while first bodies are stuck at the contact centre. With increasing the amplitude from 4 µm to 15 µm, the sticking area gradually decreases to vanish, and gross sliding takes place along the entire contact surface. Correspondingly, in the partial slip regime, the shear stress distribution along the contact surface changes depending on the displacement amplitude due to the evolution of ratio between stick area and slip area. However, in the gross sliding condition, the whole contact area is in sliding mode. Therefore the shear stress obeys Coulomb's friction law, which is proportional to the contact pressure and independent of the applied displacement amplitude, as shown in Figure 4-6 (b). This is why the displacement amplitude has no influence on the value of the peak shear stress in the gross sliding condition.

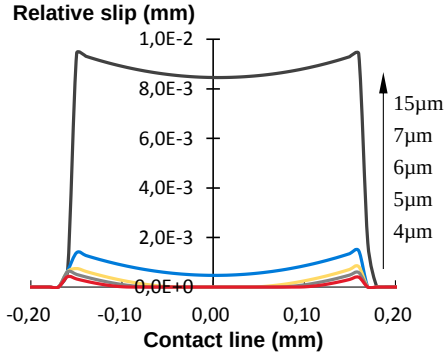

(a)

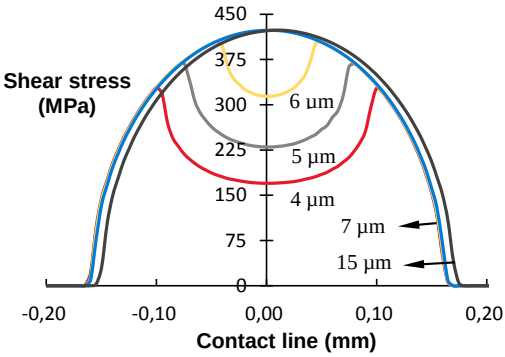

(b)

Figure 4-6. Evolutions of relative slip and shear stress for different displacement amplitudes: (a) relative slip distributions and (b) shear stress distributions

After identifying different fretting regimes, the mesh sensitivity investigation in fretting condition is presented in the following section.

4.4.1 **Effects of the applied displacement amplitude**

Firstly, effects of the applied displacement amplitude on stress singularity are investigated, when CoF is 0.8. The maximum value of the normal stress along *x*-direction of the contact surface $|\sigma_{xx}|_{max}$, and the peak shear stress at different mesh sizes and displacement amplitudes are studied. The normal stress mentioned here is the magnitude of the normal stress, *i.e.* its direction is ignored, since the divergence of peak normal stress values is considered instead of its direction.

Location of peak stresses:

The locations of $|\sigma_{xx}|_{max}$ are near the contact edge of the leading edge zone, measured the distance from the original contact centre, both in partial slip and gross sliding conditions. The location of the case with the mesh size 5 µm and D = 15 µm is shown in Figure 4-7. Complete location values of simulations are listed in Table 4-1. The result also indicates that the mesh size has little influence on the location of the contact width.

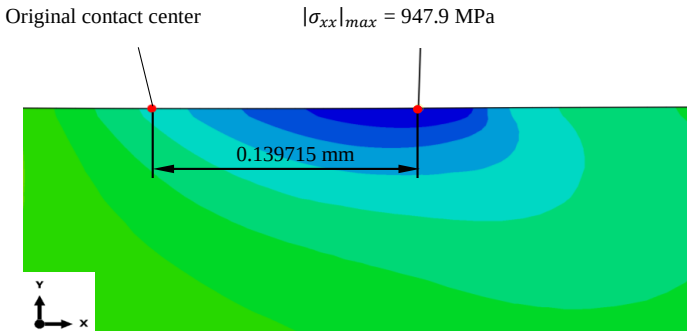

Figure 4-7. Location of the $|\sigma_{xx}|_{max}$ when the mesh size is 5 μm and D = 15 μm

Table 4-1: Location [mm] of $|\sigma_{xx}|_{max}$ in different applied displacement amplitudes and mesh sizes

***D* [μm]**	**Mesh size [μm]**		
	5	**10**	**20**
4	0.144715	0.13973	0.14129
5	0.139715	0.13973	0.14129
6	0.134725	0.12974	0.12138
7	0.134725	0.12974	0.12138
15	0.139715	0.13974	0.14129

Locations of the peak shear stress are near the transition point from stick to slip in partial slip regime, which means that the locations are different depending on the applied displacement amplitudes. While in gross sliding regime, friction follows the Coulomb's friction law, the peak shear stress is in the centre of contact line as shown in Table 4-2.

Table 4-2: Location [mm] of the peak shear stress in different applied displacements and mesh sizes

***D* [µm]**	**Mesh size [µm]**		
	5	**10**	**20**
4	-0.09979	-0.09978	0.10145
5	-0.07484	-0.07982	-0.07862
6	-0.0449	-0.04988	-0.03847
7	0	0	0.0016
15	0.009975	0.00998	0.0016

Trends of stresses as the mesh size increases:

Figure 4-8 shows the variation of stresses versus the mesh size. From Figure 4-8 (a) presenting the evolution of $|\sigma_{xx}|_{max}$, two points might be concluded: (a) the $|\sigma_{xx}|_{max}$ decreases with increasing the mesh size for a given applied displacement amplitude, no matter the magnitude of it presented herein, and (b) the $|\sigma_{xx}|_{max}$ is greater at larger displacement amplitude if using the same mesh size in partial slip condition, while the $|\sigma_{xx}|_{max}$ is constant at gross sliding condition. This is because both the shear stress and the contact pressure have influence on σ_{xx}. While in partial slip condition, the peak shear stress is changing with the applied displacement amplitude.

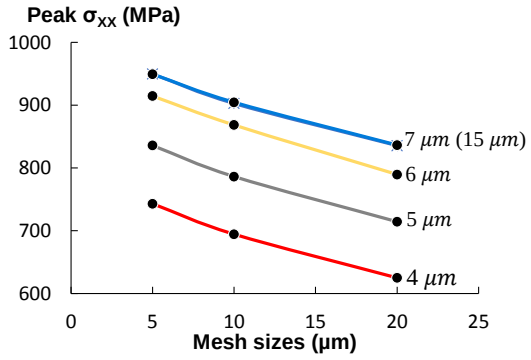

(a)

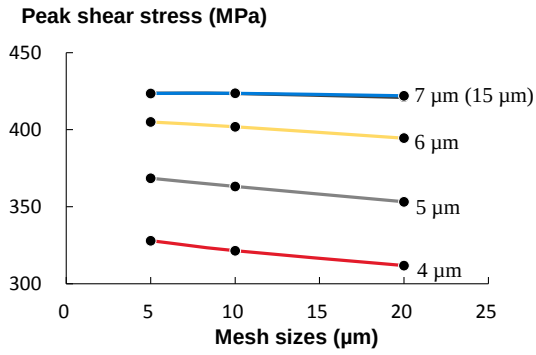

(b)

Figure 4-8. Peak stress variations under different displacement amplitudes with mesh sizes: (a) $|\sigma_{xx}|_{max}$ and (b) the shear stress

In order to study the sensitivity of $|\sigma_{xx}|_{max}$ and the peak shear stress to mesh sizes, differences of these stress values in mesh size 5 μm and 10 μm comparing to values of mesh size 20 μm are calculated, as shown in Figure 4-9 (a) and (b), respectively. It is found that the difference of $|\sigma_{xx}|_{max}$ is apparently higher than the difference of the peak shear stress for the same applied displacement amplitude. The maximum difference of $|\sigma_{xx}|_{max}$ between mesh size 5 μm and 20 μm is 18.9%, while the maximum difference of peak shear stress is only 5.2%, both of which happen when the applied displacement amplitude is 4 μm. Moreover, this difference decreases with increasing applied displacement amplitude in partial slip regime, while this difference is limited in the gross sliding regime.

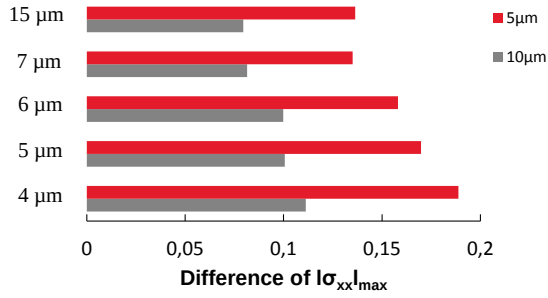

(a)

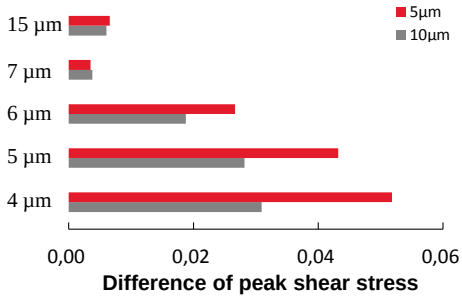

(b)

Figure 4-9. Difference of $|\sigma_{xx}|_{max}$ and the peak shear stress compared to values of mesh size 20 µm, with various displacement amplitudes

Singularity signature

Since the $|\sigma_{xx}|_{max}$ is more sensitive to mesh sizes, $|\sigma_{xx}|_{max}$ at mesh size 5 µm, 10 µm and 20 µm are taken into Equation (3-13) and Equation (3-16) to identify the type of singularity. Table 4-3 shows the calculated singularity signatures, all results are higher than 0.1, therefore there is no singularity for this situation.

Table 4-3: Results of singularity signature of the $|\sigma_{xx}|_{max}$ at different displacement amplitudes

Signature	**Displacement**		
	4 µm	**7 µm**	**15 µm**
Power σ_{xx}	0.43	0.47	0.97
Log σ_{xx}	0.35	0.41	0.94

4.4.2 **Effect of CoF**

CoF is a kind of system property. It depends on not only material properties, but also system variables, such as roughness of the interface, temperature and humidity. In fretting wear, CoF is an important factor since it has an effect on the fretting regime. In this section, stress distribution for lower CoF, *i.e.* 0.6, 0.8, 1 and higher CoF, *i.e.* 1.5, 2, 2.5 are studied. For lower CoF, applied displacement amplitudes are 7 µm and 15 µm (Larger Displacement Case, LDC), while only displacement amplitude of 4 µm (Small Displacement Case, SDC) was applied for the higher CoF cases.

Tendency of stress along the mesh size in LDC condition:

Figure 4-10 (a) shows the distribution of $|\sigma_{xx}|_{max}$ and the peak shear stress, respectively, when the applied displacement amplitude is 7 μm for different CoF cases. Again, the finer mesh shows higher $|\sigma_{xx}|_{max}$ in the same CoF case. Meanwhile, higher CoF induces higher $|\sigma_{xx}|_{max}$ due to the increased peak shear stress. Figure 4-10 (b) displays the evolution of the peak shear stress depending on various CoFs. It is also found that the $|\sigma_{xx}|_{max}$ is more sensitive to the mesh size than the shear stress.

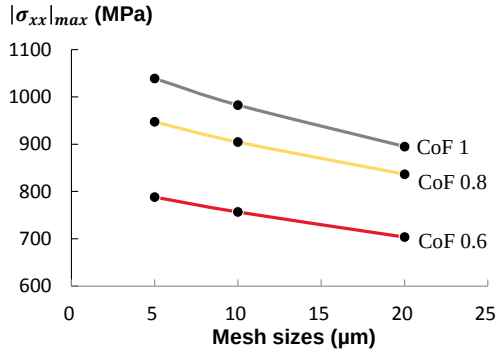

(a)

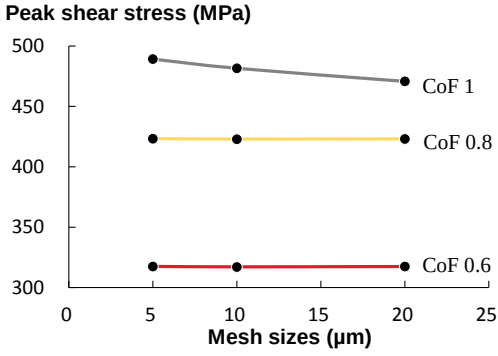

(b)

Figure 4-10. Peak stress variations at different CoF with different mesh sizes, D = 7 μm, (a) $|\sigma_{xx}|_{max}$, (b) shear stress

Differences of $|\sigma_{xx}|_{max}$ and peak shear stress in mesh size 5 μm and 10 μm compared to values of mesh size 20 μm are shown in Figure 4-11. When increasing the CoF from 0.6 to 1, the difference of $|\sigma_{xx}|_{max}$ in fine mesh (5 μm) is increasing from 12% to

16%. Meanwhile the difference of the peak shear stress of mesh size 5 μm jumps to 3% from 0.02% when CoF is increased from 0.6 to 0.8. That is because there is a transition from gross sliding to partial slip. When CoF is 0.8, gross sliding regime occurs, while partial slip occurs when CoF is 1. The higher peak shear stress is obtained in finer mesh in the latter situation.

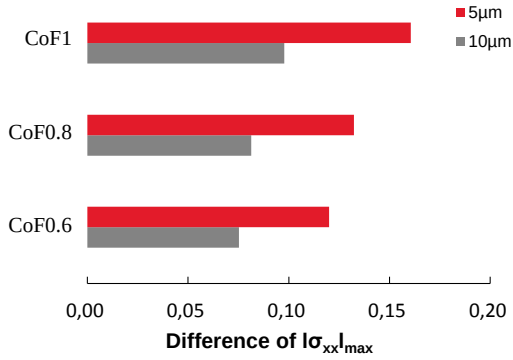

(a)

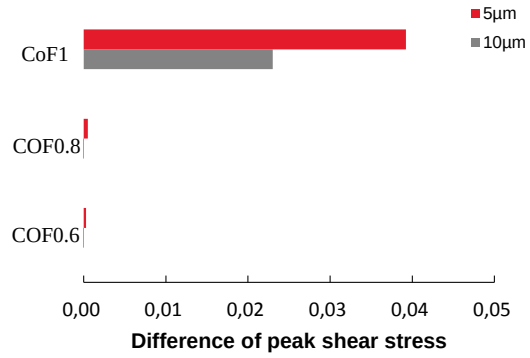

(b)

Figure 4-11. Difference of $|\sigma_{xx}|_{max}$ and the peak shear stress compared to value of mesh size 20 μm, D = 7 μm, with various CoF

When the applied displacement amplitude is increased to 15 μm, the tendency of $|\sigma_{xx}|_{max}$ with the mesh size is same as for displacement amplitude case of 7 μm, as shown in Figure 4-12 (a). Figure 4-12 (b) illustrates that the peak shear stress is constant in this mesh sequence, which means that gross sliding occurs under all three lower CoFs' conditions. In this case, difference of $|\sigma_{xx}|_{max}$ changes from 12% to 14% (Figure 4-13 (a)), and difference of the peak shear stress changes from 0.44% to 0.31%

based on the change of CoF when the mesh size is 5 µm (Figure 4-13 (b)). Both of them are less than the difference when the applied displacement is 7 µm. This means that in gross sliding regime, CoF does not affect the differences of stress significantly due to the mesh refinement.

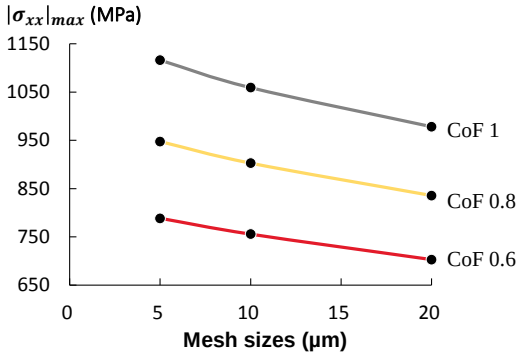

(a)

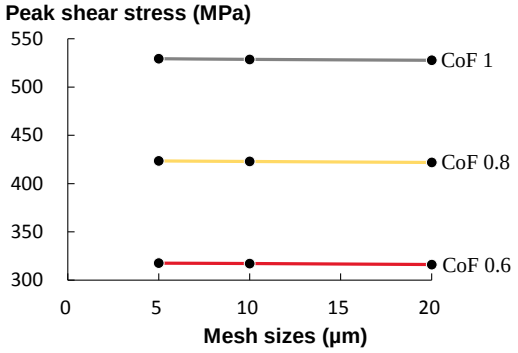

(b)

Figure 4-12. Peak stress variations at different CoF's with different mesh sizes, D = 15 µm, (a) $|\sigma_{xx}|_{max}$, (b) shear stress, with various CoFs

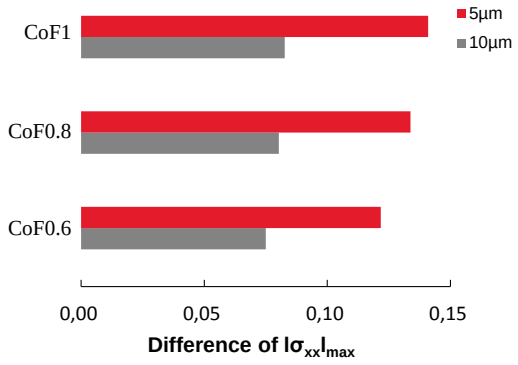

(a)

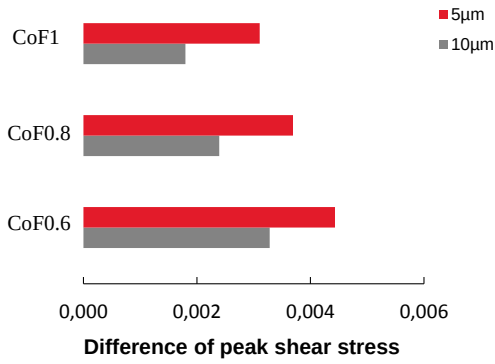

(b)

Figure 4-13. Differences of $|\sigma_{xx}|_{max}$ and the peak shear stress compared to value of mesh size 20 µm, D = 15 µm

Tendency of stress along the mesh size in SDC condition:

When decreasing the displacement amplitude to 4 µm and increasing the CoF, *i.e.* higher than 1, partial slip takes place. It could be imagined that when CoF is high enough, stick could happen in the whole contact interface. Under this condition, there should be stress singularity when applying tangential displacement in the contact interface. Therefore, CoFs are defined as 1.5, 2, 2.5 to study stress singularity in partial slip regime. The simulated results shown in Figure 4-14. $|\sigma_{xx}|_{max}$ of finest mesh is much higher than that of coarsest mesh as shown in Figure 4-14 (a). Particularly, in the case of CoF equalling to 2.5, the difference is up to 56.21% as depicted from Figure 4-14 (b). Another point should be mentioned herein: values of $|\sigma_{xx}|_{max}$ are almost same in all three CoF cases, when the mesh size is 10 µm and 20 µm, while when the

mesh size is 5 μm, the value of $|\sigma_{xx}|_{max}$ is slightly different in all three CoF's considered in this paper. This may be because a higher CoF causes little relative slip, and almost all contact points along the contact line are in stick regime.

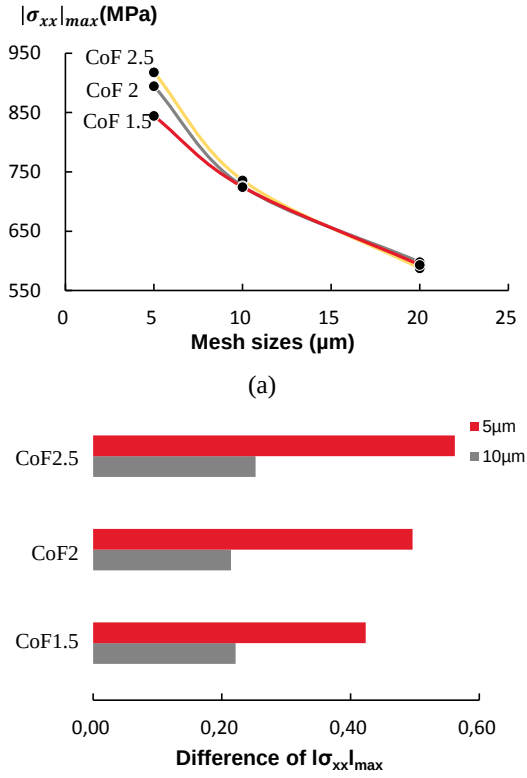

Figure 4-14. Information of $|\sigma_{xx}|_{max}$ when *D* is 4 μm at higher CoF: (a) Variations of $|\sigma_{xx}|_{max}$ with mesh sizes and (b) The differences $|\sigma_{xx}|_{max}$ compared to value of mesh size 20 μm

Singularity signature:

Table 4-4 shows the calculated singularity signature of $|\sigma_{xx}|_{max}$ for higher CoF. When the applied displacement amplitude is 4 μm, logarithmic singularity exists when CoF is 1.5, and power singularity exists when CoF is 2 and 2.5. From Figure 4-15, we could see that the power stress singularity signature is decreasing with increasing CoF, which

may indicate that, in partial slip condition, the stress is more sensitive to mesh size than in gross sliding condition.

Table 4-4: Results of the singularity signature of the $|\sigma_{xx}|_{max}$ at higher CoF

Signature	CoF		
	1.5	**2**	**2.5**
Power σ_{xx}	0.2660	0.0725	0.0171
Log σ_{xx}	0.0917	0.2725	0.2050

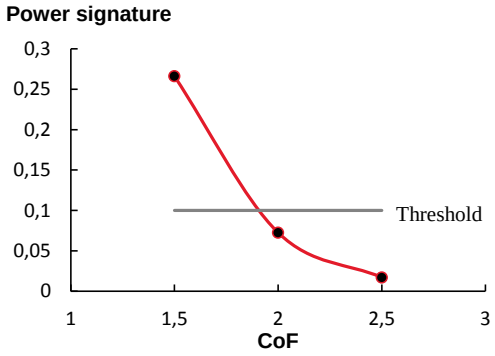

Figure 4-15. Signature evolution of power singularity at higher CoF

4.4.3 **Effect of wear cycles**

In order to study the influence of fretting wear on stress singularity, using energy concept as the wear model, applied displacement amplitude is defined as 4 μm and 15 μm to simulate fretting wear in partial slip and gross sliding conditions, respectively. The total number of fretting wear cycles is 20,000.

Figure 4-16 shows surface profiles after 20,000 cycles in partial slip and gross sliding conditions, respectively. In partial slip condition, damage caused by wear occurs at the slip-zone, and no damage is generated at the centre of the contact due to no relative slip. However, significant wear takes place along the contact surface under gross sliding condition. This confirms that fretting wear plays an important role at gross sliding condition. Due to the great damage of the contact surface after 20,000 cycles

under gross sliding condition, magnitudes of maximum tensile and compressive normal stresses decrease. While for the case of partial slip regime, little difference of normal stress distribution could be found between the 2,000th cycle and the 20,000th cycle, as presented in Figure 4-17.

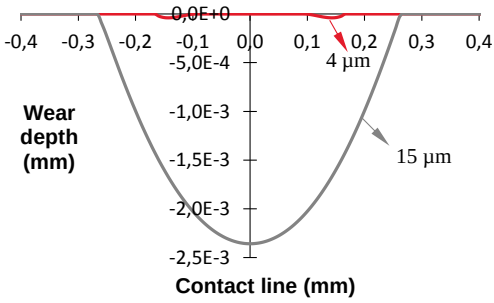

Figure 4-16. Wear profiles when D is 4 µm and 15 µm, mesh size 5 µm, N = 20,000 cycles

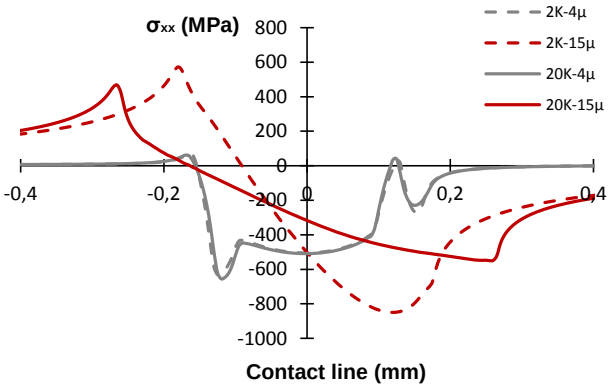

Figure 4-17. Normal stress distributions after the 2,000th cycle and the 20,000th cycle, D = 4 µm and 15 µm

Figure 4-18 shows the evolution of $|\sigma_{xx}|_{max}$ and the peak shear stress after 20000 cycles. At partial slip regime, the $|\sigma_{xx}|_{max}$ has similar tendency to the one observed before wear. While for gross sliding regime, the evolutions of $|\sigma_{xx}|_{max}$ with different mesh sizes become flatten. For the peak shear stress, almost the same evolution as Figure 4-8 (b) takes place as shown in Figure 4-18 (b).

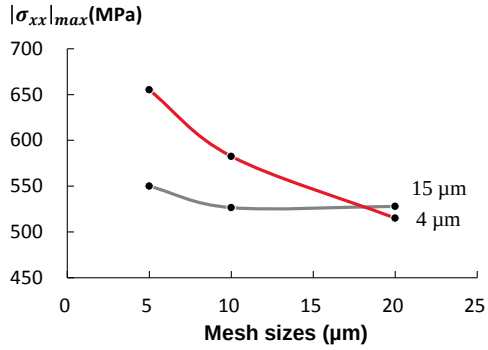

(a)

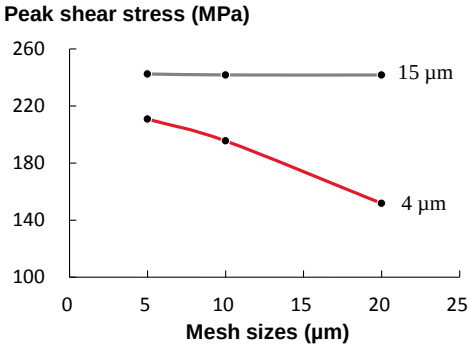

(b)

Figure 4-18. Peak stress variations with different mesh sizes, after 20,000: (a) $|\sigma_{xx}|_{max}$, (b) shear stress

The singularity signature of $|\sigma_{xx}|_{max}$ after wear is calculated and listed in Table 4-5. It can be seen that both power singularity and logarithmic singularity exist for partial slip regime. The occurring of singularity after fretting wear in partial slip condition is also confirmed by the asymptotic analysis reported in [109]. On the contrary, there is no singularity in gross sliding.

Table 4-5: The results of singularity signature of the $|\sigma_{xx}|_{max}$ after 20000 cycles

Signature	Displacement	
	4 µm	**15 µm**
Power σ_{xx}	0.0493	2.2496
Log σ_{xx}	0.0708	2.2442

Table 4-6 illustrates the comparison of stress singularity signature for $|\sigma_{xx}|_{max}$ at partial slip before and after fretting wear. Both power and logarithmic stress singularity signature are decreased significantly.

Table 4-6: Comparison of singularity signature between after ¼ cycles and after 20,000 cycles for partial slip regime (D = 4 µm)

Signature	¼ cycle	20000 cycles
Power σ_{xx}	0.5921	0.0493
Log σ_{xx}	0.4405	0.0708

4.5 Influence of a variable CoF on fretting wear

4.5.1 Constant versus variable CoF after 18,000 cycles

After 18,000 cycles, comparison between results of the wear depth and wear width obtained using variable and constant CoF are shown in Figure 4-19. When the normal load is 185 N, the FE model with a variable CoF gives lower predicted wear damage in wear width and wear depth, comparing with the basic model. However, the differences are very small. When normal load increases to 500 N, both wear width and depth for the variable CoF model are almost the same as for basic model. It could be concluded that CoF plays little role in the fretting wear profile if considering the full time scale of fretting wear cycles, *i.e.* more than tens of thousands of cycles.

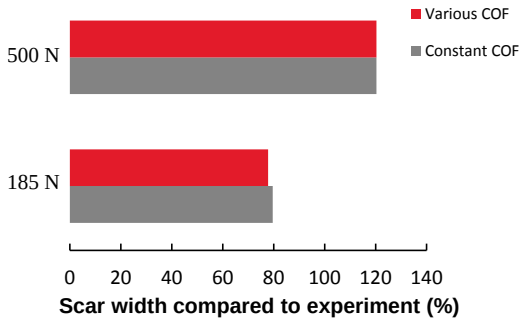

(a)

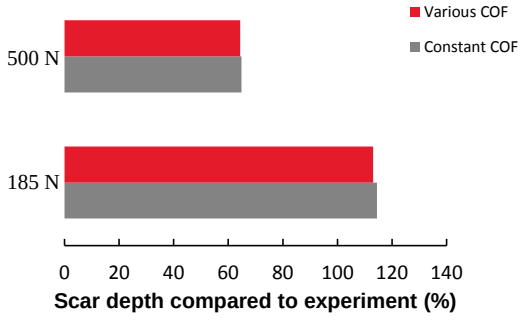

(b)

Figure 4-19. Comparison of the wear scar between cylinder/flat FE model and experiments, P = 185 N and 500 N, respectively. R=6 mm, D= 25 μm, (a) the scar width, (b) the scar depth

4.5.2 **Constant versus variable CoF in the running – in stage**

Next, the effects of CoF in the running-in stage are studied. Figure 4-20 shows the wear scar after 2,500 cycles in both CoF models. It is reasonable that the prediction of constant CoF model attains greater wear scar. This is because the constant CoF is larger than that in variable CoF model used. Higher CoF means more frictional work generated is dissipated for wear process. Thus, energy wear model brings more practical explanation for wear simulation than Archard model.

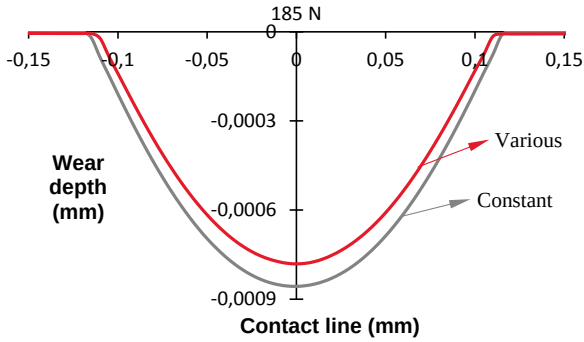

(a)

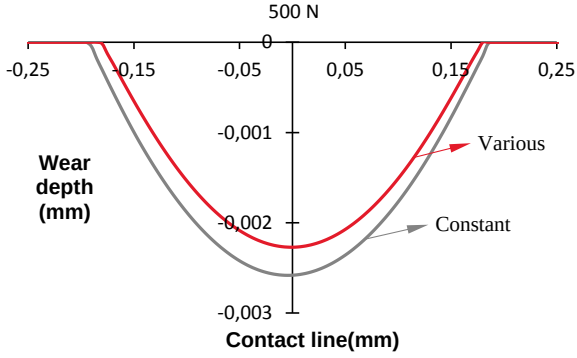

(b)

Figure 4-20. Wear scar comparisons between variable CoFs and constant CoFs cylinder/flat models after the first 2,500 cycles: (a) P = 185 N and (b) P = 500 N

Figure 4-21 presents the evolution of wear depth, wear width and peak contact pressure during the first 2,500 cycles, when P = 185 N. The wear depth and wear width of both constant and variable CoF models are increasing linearly with similar speed. Considering the peak contact pressure, both them are decreases following a power law. They are reduced significantly during the first 1,000 cycles and gradually slowing down. The same tendency is observed for the case of 500 N, which is shown in Figure 4-22.

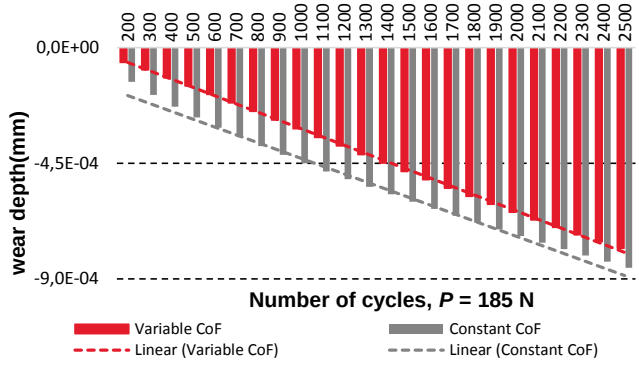

(a)

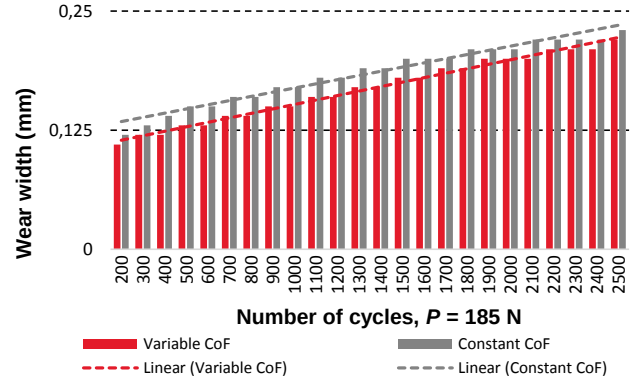

(b)

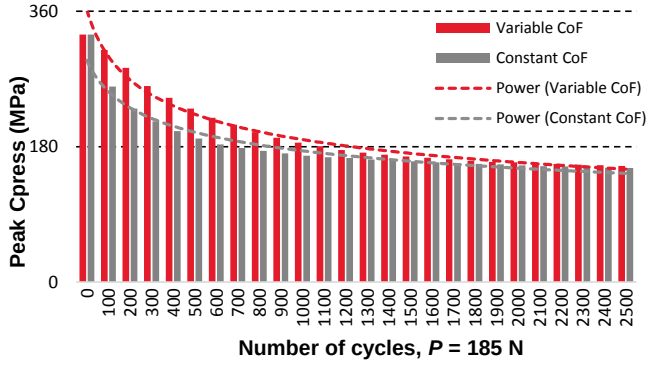

(c)

Figure 4-21. Comparison of the wear depth, wear width and peak contact pressure between variable and constant CoF models, *P*=185 N

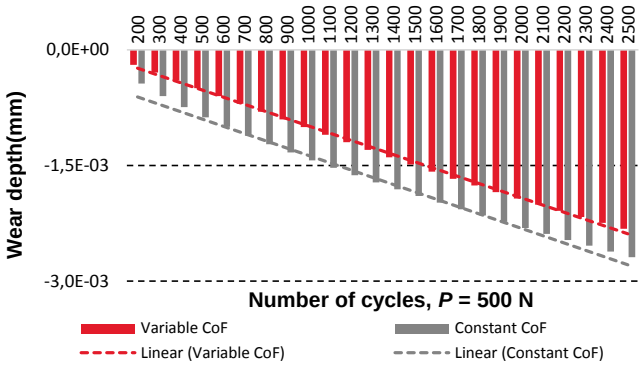

(a)

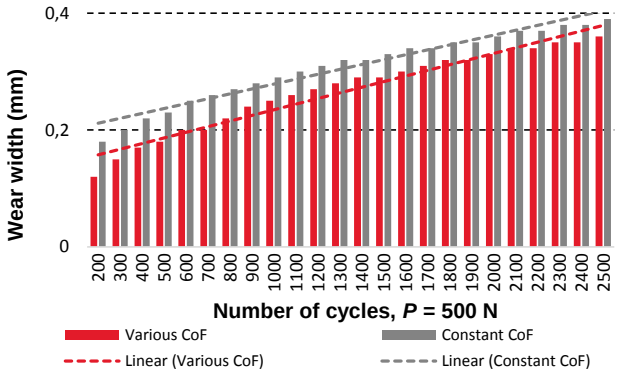

(b)

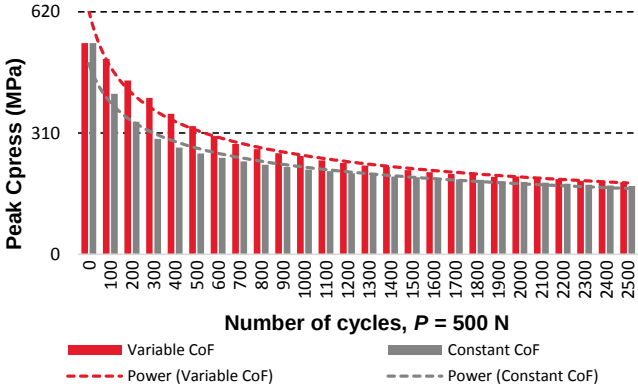

(c)

Figure 4-22. Comparison of the wear depth, wear width and peak contact pressure between variable CoF and constant CoF, *P*=500 N

The specific changes in differences of the wear scar and peak contact pressure with number of cycles are shown in Figure 4-23. For both normal load conditions, differences in wear depth, wear scar and peak contact pressure exhibit similar tendency: with increasing number of cycles, the differences between variable and constant CoF models decrease. Particularly, the difference of wear depth decreases smoothly from approximately 55% after 200 cycles to approximately 10% after 2,500 cycles. These changes could be described by a polynomial formula as:

when normal load is 185 N,

$$difference = 8 \times 10^{-6}N^2 - 0.0421N + 64.391, \quad R^2 = 0.9993 \qquad (4\text{-}5)$$

when normal load is 500 N,

$$difference = 8 \times 10^{-6}N^2 - 0.0384N + 60.886, \quad R^2 = 0.9978 \qquad (4\text{-}6)$$

Thus, the wear depth up to 2,500 cycles could be calculated by the best fitting curve instead of fretting wear simulation. However, the other three variables are oscillated with number of cycles. The reasons for this oscillation of the wear width are the numerical errors related to the mesh size, which would be further studied in future work.

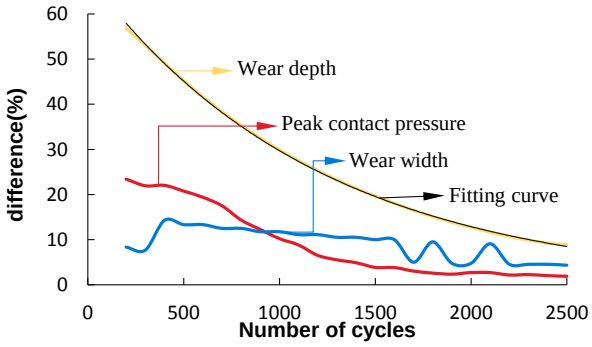

(a)

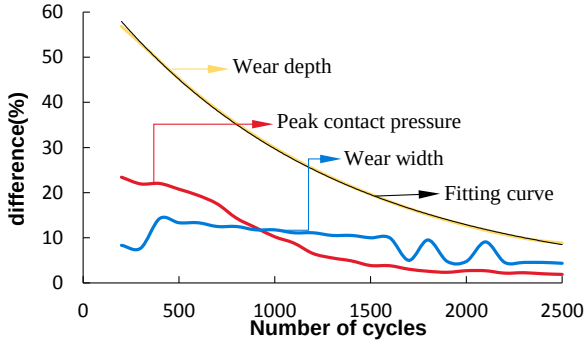

(b)

Figure 4-23. Influence of a variable CoF in the wear depth, peak contact pressure and wear width in the first 2,500 cycles: (a) P = 185 N, and (b) P = 500 N

4.6 Debris layer

4.6.1 **Contact pressure distribution before fretting wear process**

Before applying the wear calculation on the debris layer model, the influences of debris layer Young's modulus E and the thickness of a debris layer t on the contact pressure are studied. In this case, only the normal loading step is considered to study the contact pressure in the Top interface and Bottom interface. The FE model with E = 360 GPa, ν = 0.12 and t = 5 µm is defined as a reference case. E varies as 280, 200 and 120 GPa and t varies as 5, 10 and 20 µm. Figure 4-24 shows that little difference of the contact pressure distribution could be found in the Top and Bottom interfaces, considering various *Es* using a constant debris layer thickness. Therefore, we can conclude that E has little influence on the contact pressure distribution when the thickness of the debris layer is kept constant, *i.e.* 5 µm.

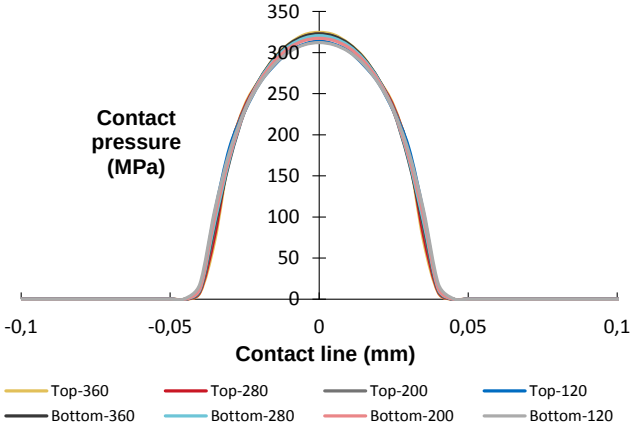

Figure 4-24. Contact pressure distributions of the Top and Bottom interfaces in different E of the debris layer, t = 5 μm

Next, the effects of the debris layer thickness are studied. As shown in Figure 4-25, by increasing the thickness of the debris layer, little difference exists in the contact pressure distribution of the Top interface. For the Bottom interface (Figure 4-26), however, the peak contact pressure decreases and the contact width increases by increasing the thicknesses of the debris layer.

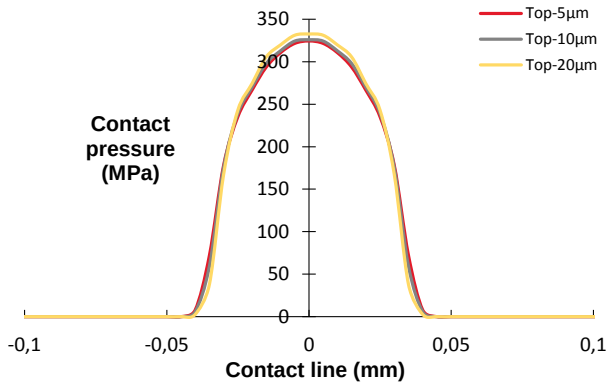

Figure 4-25. Contact pressure distributions of the Top interface in different thicknesses of the debris layer, E = 360 GPa

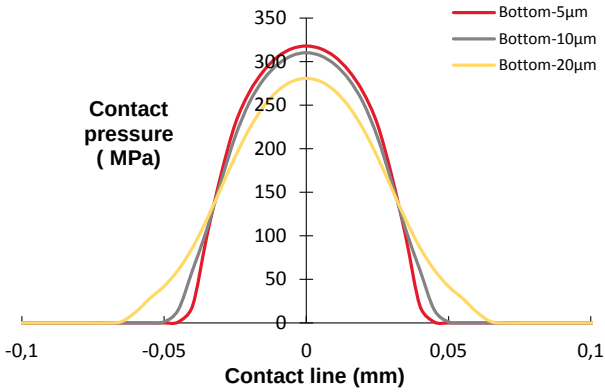

Figure 4-26. Contact pressure distributions of the Bottom interface in different thicknesses of the debris layer, E = 360 GPa

Based on the contact pressure distributions, it could be concluded that the thickness of the debris layer is an important factor for the Bottom interface of the debris layer model. As assuming fretting wear occurs at this interface, in the following analysis, only the effects of the thickness of the debris layer are considered.

4.6.2 **Contact pressure distribution during fretting wear process**

The influence of the debris layer on the contact pressure distribution is investigated in this section. The contact pressures of Bottom interface after different numbers of cycles are presented in Figure 4-27 - Figure 4-29, for different thicknesses of the debris layer. For all three importing time cases, similar tendency of the contact pressure with layer thicknesses are observed. It is found that: after the same number of cycles, *i.e.* after 500 cycles, 1,500 cycles and 2,500 cycles, the contact pressure at the centre of the specimen is reduced by increasing the thickness of the debris layer. However, the contact pressure at the wear scar edge shows the opposite trend. The contact pressure dramatically increases at the wear scar edge due to the stress concentration at the debris layer edge. This is the significant difference from the contact pressure distribution of the model without a debris layer, in which the contact pressure decreases to zero at the contact edge.

With increasing the number of cycles, the contact pressure reduces and contact width increases, which is a similar trend as in the case of the fretting wear model without debris layer. This is because of the continuously changing of contact surface. In addition, the location of the peak contact pressure is shifted to the debris layer edge

after 500 cycles for all three thicknesses. After 1500 cycles, however, the maximum contact pressure is shifted to the central point of the contact surface in the lower thickness cases, *i.e.* t = 5 µm and 10 µm. For the case of t = 20 µm, the contact pressure at the debris layer edge also reduces dramatically, to a value similar to that of central point.

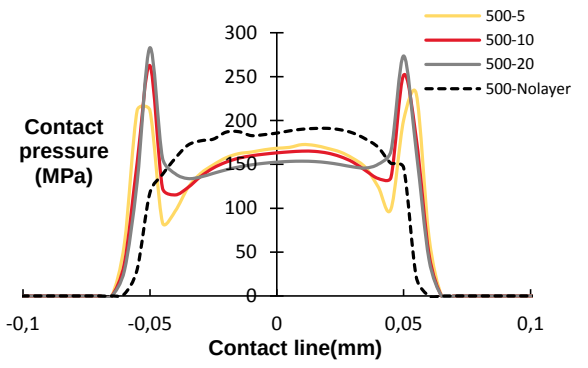

Figure 4-27. Contact pressure distribution for different debris layer thicknesses and number of cycles: layer thickness = 5 µm, 10 µm, 20 µm and without debris layer after 500 cycles

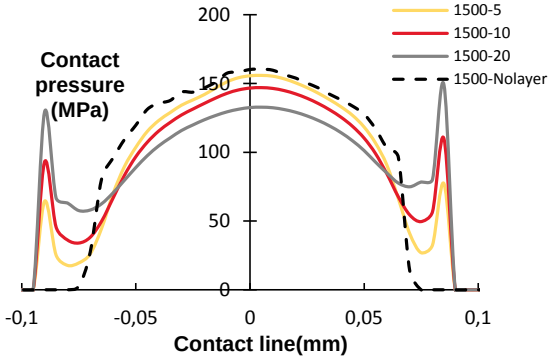

Figure 4-28. Contact pressure distribution for different debris layer thicknesses and number of cycles: layer thickness = 5 µm, 10 µm, 20 µm and without debris layer after 1,500 cycles

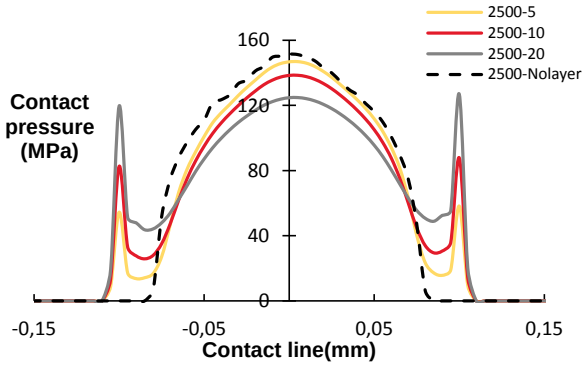

Figure 4-29. Contact pressure distribution for different debris layer thicknesses and number of cycles: layer thickness = 5 µm, 10 µm, 20 µm and without layer, after 2,500 cycles

Based on Figure 4-27 - Figure 4-29, it is clearly seen that the debris layer significantly affects the distribution of the contact pressure as well as its magnitude.

Results of other models also showed similar tendency. Figure 4-30 illustrates the contact pressure with/without considering effects of debris layer after different wear cycles. The peak contact pressure shifts to the contact edge when considering debris layer.

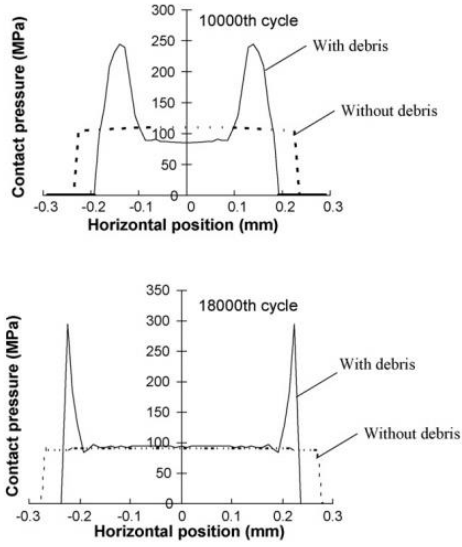

Figure 4-30. Comparison of contact pressure distributions [83]

Debris of fretting wear is also modelled as particles as presented in reference [110]. Figure 4-31 (a) shows the Hertzian contact distribution. And Figure 4-31 (b) depicts the contact pressure distribution with debris particles under the same loading condition. In this case, one debris particle is located at each edge of contact. Due to the small size of particles, peak contact stress occurs at the contact edge.

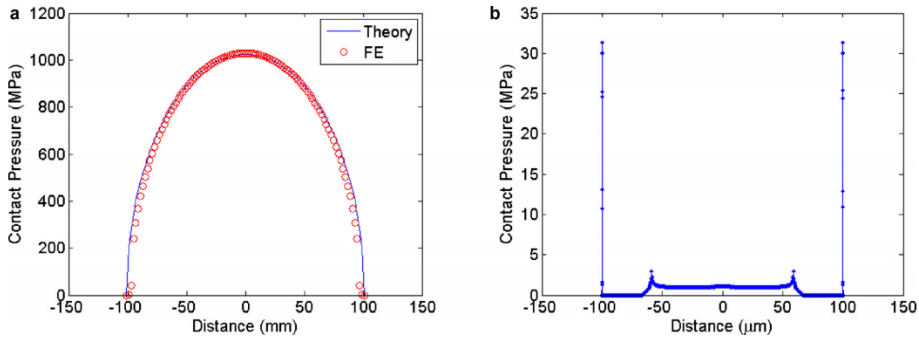

Figure 4-31. Contact pressure distribution: (a) without debris and (b) with debris particles at the contact edge [110]

Therefore, the appearance of stress concentration at the contact edges is support by reference [83] and [110].

Generally, the debris layer carries a portion of the load. Both the thickness of the debris layer and the wear width of the substrate are the predominant factors. However, they interact with each other. This interaction has not been studied in this model.

4.6.3 **Wear scar comparison after importing debris layer for 500 cycles**

In order to study the effects of the debris layer on wear scar, firstly, the wear scars after importing debris layer by 500 cycles of fretting are compared. Figure 4-32 shows wear scars of the debris layer model in the case of importing time 500th cycle, which is 500 + 500 =1,000 cycles. It is found that wear scars are almost same in all three thickness cases. Thus, the effect of thickness is little on the wear scar. In addition, comparing to the model without debris layer, both wear width and wear depth calculated by debris layer model reduce 5% and 15%, respectively.

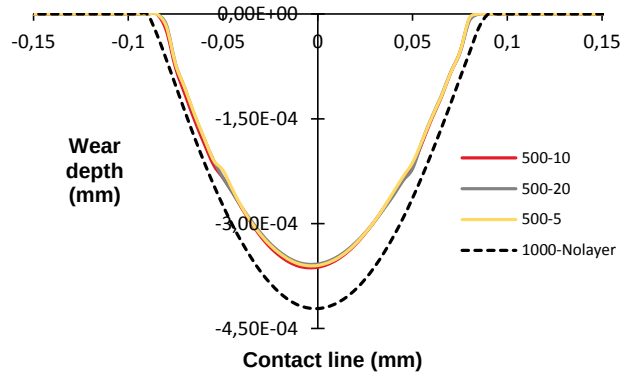

Figure 4-32. Wear scars after 1,000 cycles

However, in the cases: importing time = 1,500 and 2,500 cycles, it shows the opposite tendency, as presented in Figure 4-33. More wear damage is generated in both cases. For the wear depth, it increases 8% and 6%, after 2,000 cycles and 3,000 cycles, respectively. For the wear width, it is 4.8% and 4.1% after 2,000 cycles and 3,000 cycles, respectively.

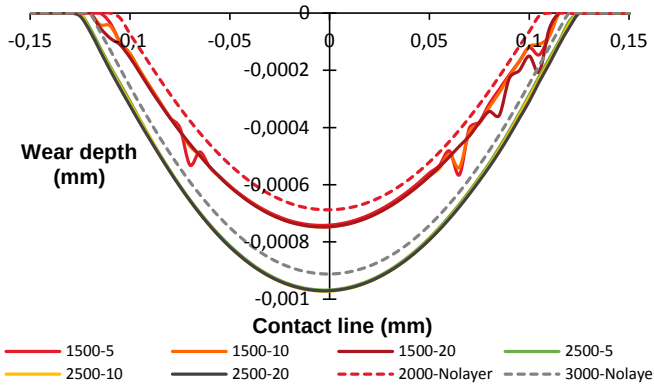

Figure 4-33. Wear scars after 2,000 cycles and 3,000 cycles

4.6.4 **Wear scar after running-in stage**

The wear scars after the running-in stage: 3,000 cycles are compared in Figure 4-34 - Figure 4-35. Figure 4-34 shows different wear scars when the importing time is 500th cycle. The influence of thickness is minor on the wear scar, and approximately similar as the condition without the debris layer.

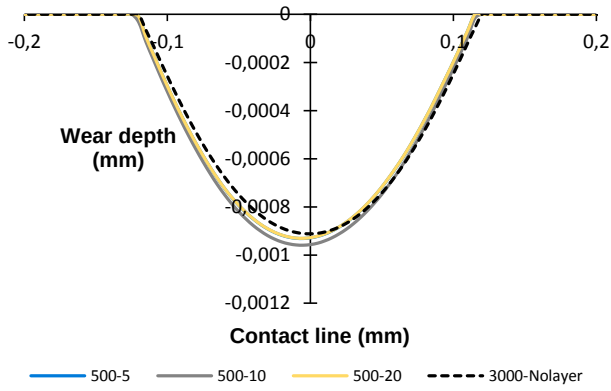

Figure 4-34. Wear scar after 3,000 cycles of the debris layer model, imported time = 500th cycles

When importing of the debris layer in later cycles, *i.e.* 1,500th and 2,500th cycles, the difference between wear scars obtained from models with/without debris layer still could be seen, as shown in Figure 4-35 and Figure 4-36. However, these differences on the wear depth and wear width are decreased comparing to it after 2,000 and 3,000 cycles, respectively.

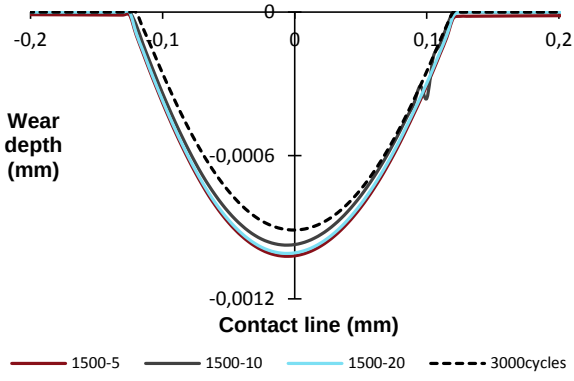

Figure 4-35. Wear scar after 3,000 cycles of the debris layer model, importing time = 1,500th cycle

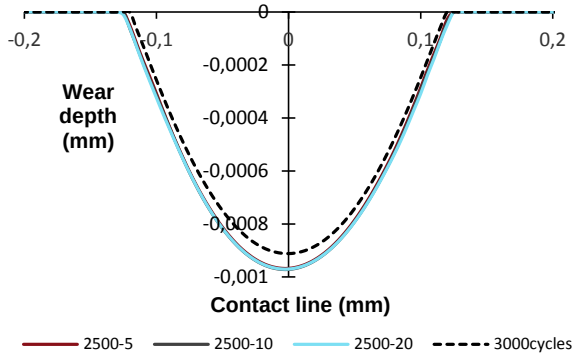

Figure 4-36. Wear scar after 3,000 cycles of the debris layer model, importing time = 2,500th cycle

4.6.5 **Final wear scar**

The final wear scars are presented in Figure 4-37. Minor differences are observed among FE results of different debris layer models.

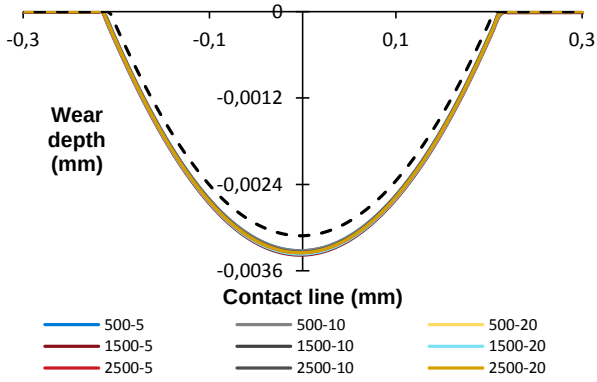

Figure 4-37. Wear scar after 18,000 cycles, based on the debris layer model

4.6.6 **Discussion**

This research is focus on the role of debris playing during the fretting wear process. In this study, debris is assumed as the layer structure of $\alpha - Fe_2O_3$ with three thicknesses: 5 µm, 10 µm and 20 µm. These debris layers are imported after different cycles, *i.e.* 500th cycles, 1,500th cycles and 2500th cycles, in the running-in stage. Based on this

debris layer model, the wear volume after importing debris for 500 cycles, after running-in stage and the final cycle are compared.

For three importing time cases, as listed in Figure 4-38, the wear volume after 500 cycles, when the importing time is 500th cycle, is underestimated by approximated 18% comparing to the model without debris layer. As explained in section 4.6.2 , with the introduction of the debris layer, the contact pressure distribution is changed that the stress concentration also exists at the contact edge of debris and substrate surface, besides the contact centre. Thus, followed the Coulomb's friction law, the shear stress distribution also shifts. In addition, after 500 cycles, the contact widths between the models with/without the debris layer are similar since the micro wear volume. In this case, the reduction of shear stress causes the decreasing of wear volume in 1,000 cycles. In contrast, the wear volume after 500 cycles for cases importing time = 1,500th cycle and 2,500th cycles, are all higher than cases without debris layer. This could be explained by the effects of the combination of the contact pressure and the contact width. With increasing the number of fretting cycles, the wear width is relative larger so as the length of the debris layer. The contact width enlarges to the edge of debris layer, which is much wider than the case without debris layer. Hence, although the shear stress is still less than the case without debris layer, the wear volume is severer according to the calculation based on the energy concept.

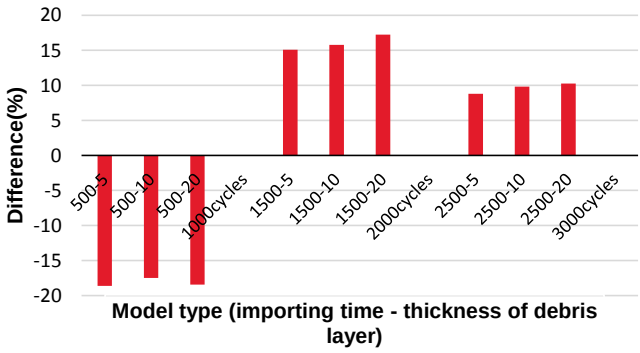

Figure 4-38. Difference of the wear volume comparing to the same case without layer, 500 cycles after importing debris layer. 500th cycle: 1,000 cycles; 1,500th cycle: 2,000 cycles; 2,500th cycles: 3,000 cycles

After the running-in stage, *i.e.* 3,000 cycles, more wear volume happens in most cases of debris layer model, shown in Figure 4-39.

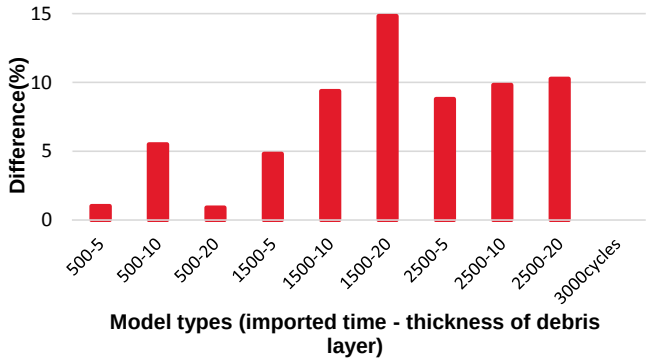

Figure 4-39. Difference of the wear volume comparing to the same case without layer, after 3,000 cycles

For the final cycles, the appearance of debris layer brings more wear volume by 10% to 13.6% depending on the importing time and the thickness of the debris layer. However, as Figure 4-40 shown, differences among importing time, thicknesses of the debris layer to wear volume are similar.

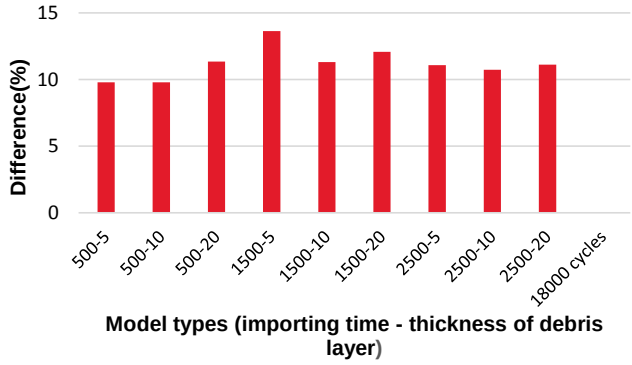

Figure 4-40. Difference of wear volume comparing to the same case without layer, after 18,000 cycles

Based on the evolution of wear volume, it can be found that the debris layer is a protection of the first bodies at the beginning of fretting wear. With increasing number of cycles, the wear volume grows quickly due to the enlarged contact area, and more wear volume occurs comparing to the model without debris layer. However, in the study of J. Ding [83], the introduction of debris layer induced smaller scar width and slightly deeper wear depth. In addition, the wear volume predicted by debris model was less than the case without debris layer and underestimated more comparing to the

experiment results. Due to the complicity of debris, more parameters should be considered in the modelling of debris material.

Meanwhile, the effect of thickness of the debris layer on wear volume is very slight, the possible reasons for these minor differences are:

1. Only 500 cycles with debris layer effects are considered. Although the wear scar generated during these 500 cycles is assumed as the effects of debris layer for sequent fretting wear process, the influence of debris layer on contact pressure is ignored in the remaining fretting wear cycles.
2. Only 500^{th}, $1{,}500^{th}$ and $2{,}500^{th}$ cycle are defined as the importing time. Although after the running-in time, which is 3,000 cycles in the loading case: P=185 N and D=25 μm, it is steady period of fretting wear process, the interfaces of the debris layer and wear scar are continuously changing. Therefore, more importing time should be taken into account.
3. The thickness of the debris layer assumed here is comparatively larger than the one measured in experiments, which is around 2 μm. Although the effects of thickness show little influence on the final wear scar based the FE results FE, fretting wear model with thinner layer should be studied. In order to avoid convergence problems, multiscale analysis may be a suitable technique, which could predict the evolution of debris in micro scale and fretting wear in the macro scale.
4. In addition, the evolution of the thickness of the debris layer is difficult to assume. As shown in [101], the thickness did not increase monotonically with number of cycles. More experiments should be done to study the debris layer behaviour in the fretting wear process.

4.7 Concluding remarks

In this chapter, FE results of different models are presented and analysed. Through the presented numerical results, the following main conclusions can be drawn:

1. Stress singularity exists in the partial slip condition with higher CoF. The sensitivity of the element size at the contact surfaces is very significant, and therefore the mesh sizes required for a converged solution need to be

determined. Furthermore, the results indicate that these mesh sizes depend on the fretting regimes.

2. CoF has little influence in the final wear scar for the given fretting couples studied here. However, up to the running-in stage, CoF plays significant role in the wear depth, wear width and the value of the peak contact pressure. The differences in these variables between constant CoF model and variable CoF model are decreased with the number of cycles. Specifically, the difference in the wear depth is reduced smoothly.

3. In a debris layer fretting wear model, Young's modulus of the debris layer has little influence on the contact pressure in both Top and Bottom interfaces. However, the thickness of the debris layer plays an important role at the bottom interface. The location of the maximum contact pressure changes from central point of contact surface to the layer edge when importing the debris layer after 500 cycles. Furthermore, the contact pressure decreases sharply with number of cycles, especially the contact pressure at the debris layer edge. However, comparing the final wear scar after 18,000 cycles, little difference could be found among these FE models with the debris layer. The possible reasons are listed at the end of this section. At the beginning of fretting wear, debris layer protects the contact surface and reduces wear volume comparing to results from the model without the debris layer. While after 18,000 cycles, more wear volume occurs when considering the effects of debris layer. In addition, the thickness of the debris layers has slight influence on the wear volume.

Chapter 5

Practical application: fretting wear in wires

5.1 Overview

In this chapter, we investigated the influence of material property on fretting wear of wire ropes. The remainder of this chapter is organized as follows. In section 5.2, the FE model used for the fretted wire is described, including the geometry information and the calculation of the wear coefficient. After that, the FE results are verified with analytical solution and validated with experimental results. The fretting loops in elastic and elastic-perfectly-plastic conditions are analysed. Finally, the conclusion is summarized.

5.2 FE model in wires

Indeed, in wire rope systems, the crossing angle of wires range is usually 5° to 45° [111]. However, in order to validate FE results with experimental results presented in [94], a crossing angle of 90° is used in this study. The diameter of wires in FE model is 1 mm and is made of cold drawn, high-quality carbon structure steel. The CoF between contact surfaces is kept constant as 0.12, when the normal load applied P is 9 N and the displacement amplitude D is 5 μm. The material property is shown in Table 5-1. In this study, elastic and elastic-perfectly-plastic conditions are used to compare results with experimental data.

Table 5-1: Material properties of wires used in FE model, taken from [94]

Material	**Young's modulus E [GPa]**	**Poisson ratio υ**	**Yield strength [GPa]**
Steel wire	203	0.3	0.64

The configuration of two cylindrical wires with same material and radii crossed at 90° is generated in the commercial FE software ABAQUS/STANDARD, as shown in Figure 5-1. The contact interaction between two wires is defined by surface to surface with finite sliding contact pair algorithm, in which master–slave algorithm is used to search for the contact pair. Herein, the surface of upper wire is master surface and the surface of the other wire is slave surface. Lagrange multiplier algorithm is chosen to solve the contact problem in order to obtain more accurate relative slip than in case of penalty method.

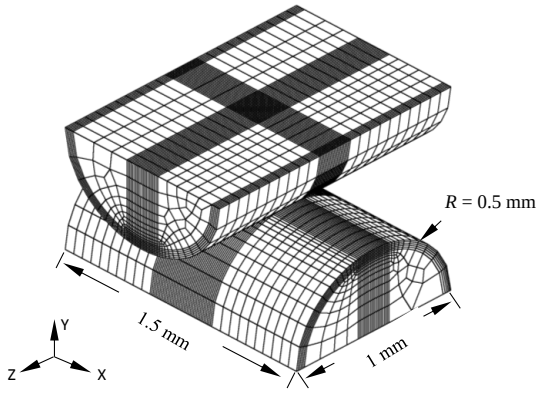

Figure 5-1. Geometry and dimensions for the wires contact

The constant normal load and boundary conditions allowing vertical movement are applied on the top wire by kinematic coupling to define rigid motion in a reference point during the whole simulation [112]. In addition, for the bottom wire, the reciprocating displacement in x direction is imposed after applying the normal load. The loading history here is the same as in [113] and is shown in Figure 3-4. The 8-node linear brick element C3D8 is chosen in the elastic model. For the elastic-perfectly-plastic model, the 8-node linear reduced integration with hourglass control brick element C3D8R is used. The mesh size in contact zone is $10 \times 10 \times 10$ μm in the elastic model and $5 \times 10 \times 10$ μm in the elastic-perfectly-plastic based on convergence study, respectively. The total number of cycles is 13,000, and the jump cycle is chosen as 1,000 for balancing accuracy and efficiency. Energy model for calculating fretting wear is used, and the procedure of that can be found in section 3.3.

5.3 Wear coefficient calculation

Owning to lacking the Archard wear coefficient K_A in [94], K_A is calculated based on Archard model of fretting wear as follows [98, 100]:

For the two equal elastic cylinders with Young's modulus E and radius R crossed at right angle, the function of wear scar radius a with number of cycles N, applied normal load P and stroke $2D$, is:

$$a = \sqrt[4]{a_0^4 + \frac{8K_A\, RP\Delta xN}{\pi}} \quad (5\text{-}1)$$

where a_0 is the Hertzian contact radius,

$$a_0 = 0.909\sqrt[3]{\frac{PR}{E}} \quad (5\text{-}2)$$

And the relation between fretting wear depth h and a is given by:

$$h = \frac{a^2 - a_0^2}{2R} \quad (5\text{-}3)$$

Therefore, the Archard wear coefficient K_A could be obtained by:

$$K_A = \frac{[(2Rh + a_0^2)^2 - a_0^4]\pi}{16RPDN} \quad (5\text{-}4)$$

Thus, energy wear coefficient K_E, based on Coulomb's friction law, is obtained as:

$$K_E = \frac{[(2Rh + a_0^2)^2 - a_0^4]\pi}{16RPDN\mu} \quad (5\text{-}5)$$

Therefore, K_E could be calculated based on h measured from experiments. When $P = 9\ \mathrm{N}, 2D = 10\ \mu\mathrm{m}$, $h = 1.89\ \mu\mathrm{m}$ from [94]. It should be mentioned that the plastic deformation occurs in this loading condition, even only indentation, according to FE results calculated based on material properties listed in Table 5-1. Figure 5-2 shows that the maximum indentation displacement is 0.7 μm due to the plastic deformation. However, in experiments, it is difficult to separate the plastic deformation from the wear depth measurement. Therefore, in experiments, h is measured as the summation of the wear depth and the plastic deformation, where the depth due to the plastic deformation is 37.6% of h under this loading condition. Thus, K_E calculated by h is larger than the real situation. Considering this point, four conditions are simulated listed in Table 5-2. $K_E = 4.04 \times 10^{-8}\ \mathrm{MPa}^{-1}$, is calculated by h, while $K_E = 2.09 \times 10^{-8}\ \mathrm{MPa}^{-1}$ is obtained by the subtraction of the plastic displacement from h. Due to the convergence problem in the plastic deformation of the whole period of fretting wear, fretting wear of the first 1,000 cycles is studied here.

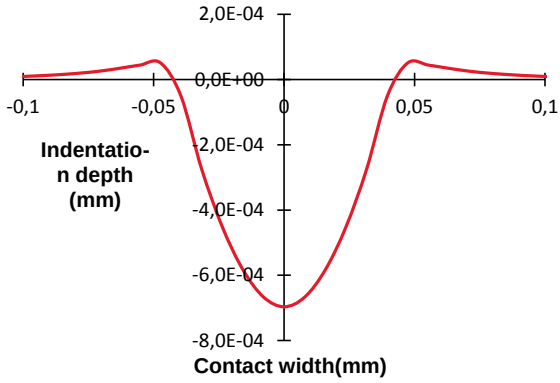

Figure 5-2. The indentation depth of the specimen surface in the vertical direction from FEM, $P = 9$ N, $R = 0.5$ mm

Table 5-2: Key parameters on this elastoplastic behaviour study

No. of the simulation	Number of cycles	K_E [MPa^{-1}]	Material behaviour
1	13,000	4.04×10^{-8}	Elastic
2	13,000	2.09×10^{-8}	Elastic
3	1,000	4.04×10^{-8}	Elastic-perfectly-plastic
4	1,000	2.09×10^{-8}	Elastic-perfectly-plastic

5.4 FE results

5.4.1 **Verification with Hertzian point contact formula**

Analytical formula in Hertzian contact for two equal cylinders with right angle is [23]:

Maximum contact pressure: $P_{max} = \sqrt[3]{\frac{6PE^2}{\pi^3 R^2}}$

The comparison of FEA results and Hertzian solution is shown in Table 5-3. Both differences of P_{max} and contact radius are less than 5%, which are in good agreement with each other.

Table 5-3: Comparison of FEA results and analytical solutions in P_{max} and a_0

Contact variables	**Hertzian solution**	**FE results**	**Difference* (%)**
P_{max} [MPa]	4454.54	4395	1.34
a_0 [mm]	0.0031	0.0029	4.8

*: Difference= (FE results – Hertzian solution) / Hertzian solution

5.4.2 **Validation with experimental results**

The first comparison of FEM and experimental results is wear depth after 13,000 cycles. Table 5-4 lists the range of wear depth from experiments. According to [114], about 66.67% of the data points should be in the range of mean ± 1 Standard Deviation (SD), namely 1.5~2.3 μm, and about 95% of the data points will be within 2 SD of the mean that is 1.1~2.7 μm.

Table 5-4: Wear depth range based on [94]

Unit/ μm	Mean	Max(1SD)	Min(1SD)	Max(2SD)	Min(2SD)
Maximum wear depth	1.9	2.3	1.5	2.7	1.1

The wear depth of the bottom wire of simulation 1 and 2 are depicted in Figure 5-3. It is found that: in both cases, the distributions of the wear depth along *x* and *z* directions are same as each other due to the micro displacement amplitude. When $K_E = 4.04 \times 10^{-8}$ MPa^{-1}, the wear depth is 2.7 μm and it is 1.77 μm with $K_E = 2.09 \times 10^{-8}$ MPa^{-1}. Although both the wear depths predicted are in the range of 2 SD, the $K_E = 2.09 \times 10^{-8}$ MPa^{-1} case is more reliable comparing the case of $K_E = 4.04 \times 10^{-8}$ MPa^{-1} in the upper bound of the 2SD range.

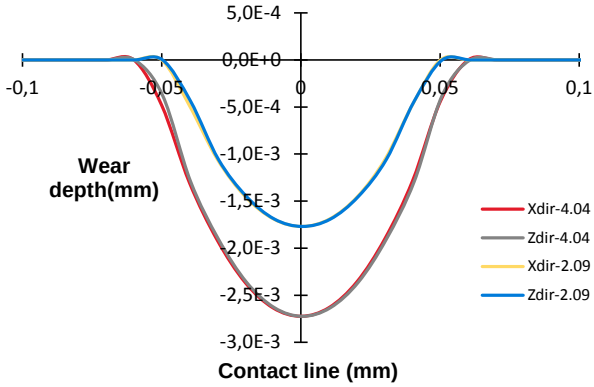

Figure 5-3. Wear depth distributions of 13,000 cycles along *x* and *z* direction, $K_E = 4.04 \times 10^{-8}$ MPa^{-1}, 2.09×10^{-8} MPa^{-1}, respectively

It is also found that the wear damage occurs in the central of contact in Figure 5-3, which is rather a characteristic of fretting behaviour under the gross sliding condition than a morphology of annularity as described in [94] as in partial slip situation. Due to this disagreement, firstly the onset displacement $\delta_{sliding}$ of gross sliding in elastic condition is calculated as [99]:

$$\delta_{sliding} = 2 \times \frac{3\mu P(2-\nu)}{16 a_0 G} \quad (5\text{-}6)$$

where $G = \frac{E}{2(1+\upsilon)}$.

Thus, the calculated threshold of displacement in the case is 0.294 µm. It means that in the elastic condition, gross sliding occurs when the applied displacement is greater than 0.294 µm. The applied displacement amplitude here is 5 µm that is 34 times larger than this threshold and gross sliding occurs. This is the case of the FE results predicting.

Next, fretting loops are compared. In Figure 5-4 (a) from experiment of [94], the fretting loop displays a typical quasi-closed line, which indicates only the adhesion occurs in the centre of the contact surface. This micro displacement only leads to the elastic deformation of the contact surface. However, fretting loops of Figure 5-4 (b) based on the FEM results after both 1,000 and 13,000 cycles show quasi-rectangular shapes revealing that the entire bulk is sliding with each, *i.e.* it is under gross sliding condition. Meanwhile, with increasing number of cycles, the dissipated energy

increases. This tendency is also found in fretting wear of aluminium alloy reported in [115] .

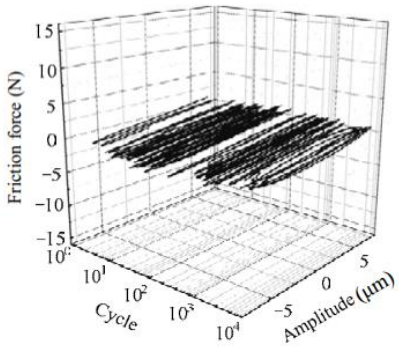

(a)

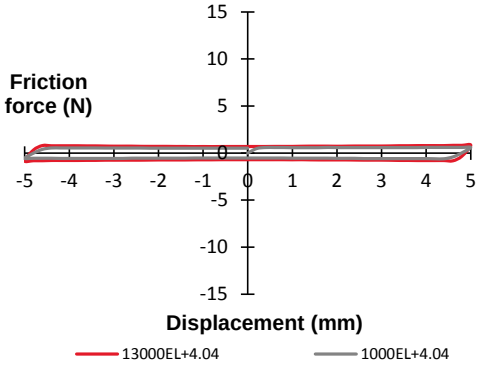

(b)

Figure 5-4. Fretting loops: (a) experimental results [94], (b) fretting loops after 1,000 cycles and 13,000 cycles in elastic condition based on FE results, $K_E = 4.04 \times 10^{-8}\ \mathrm{MPa}^{-1}$

5.4.3 **Comparison between the elastic model and elastic-perfectly-plastic model**

The comparison of fretting loops after 1,000 cycles in the elastic model and the elastic-perfectly-plastic model is plotted in Figure 5-5. All these loops present the quasi-rectangular shape. In both K_E cases, the friction forces under elastic-perfectly-plastic condition are greater comparing to results calculated in elastic condition, with little changes in the displacement. Therefore, the dissipated energy, the area of the fretting

loop, in the plastic condition is 16.54×10^{-6} J and the elastic case is 11.07×10^{-6} J. Meanwhile, the friction force and the dissipated energy are independent of the wear coefficient.

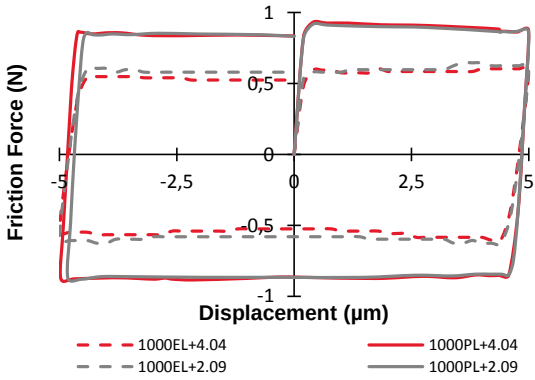

Figure 5-5. Fretting loops of 1,000 cycles in elastic and elastic-perfectly-plastic conditions

Since part of the dissipated energy is consumed for wear, the wear depths predicted with different material behaviours are compared in Figure 5-6. In the plastic deformation condition, the wear depth is obtained by subtraction of the plastic deformation due to indentation (shown in Figure 5-2), which is the displacement of the contact surface in the bottom wire along *y* direction after the normal loading step. It could be found that increasing wear coefficient from 2.09×10^{-8} MPa^{-1} to 4.04×10^{-8} MPa^{-1}, wear depth of central point is growing by 66.5% in elastic condition while it is only 15.1% with consideration of plastic deformation. Therefore, the wear coefficient has more influence on the wear depth in elastic case other than plastic case. Meanwhile, in the lower wear coefficient case, the maximum wear depth of plastic case is larger than the elastic one. However, when the wear coefficient increases, the wear of elastic case gets more serious than the plastic one, especially at the centre of contact. In addition, profiles of wear scars are different in these two material behaviour conditions. The maximum wear depth in elastic model is in the centre of contact surface and decreased gradually to the contact edge, as 'U' shape. In plastic condition, however, the maximum depth is at the contact edge and flattens in the centre of the contact surface, as 'W'. This wear profile is similar to the wear scar shape of partial slip condition. In this condition, maximum wear damage is in the edge of contact and

less damage happens at the contact centre. The ploughing effect presents in the edge of wear scar due to the plastic deformation, which was also reported in [42, 75].

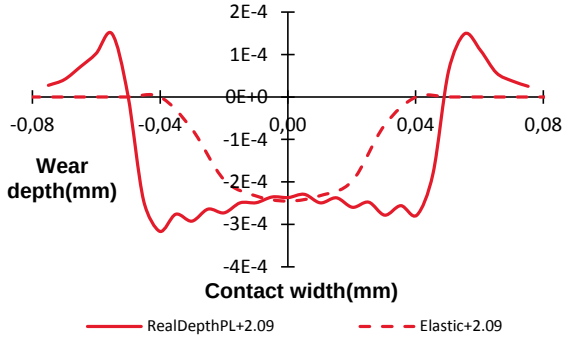

(a)

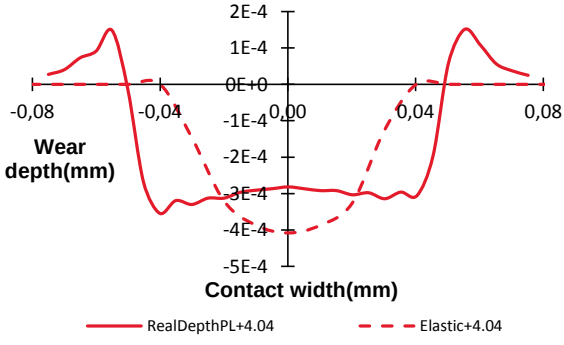

(b)

Figure 5-6. Wear depth of 1,000 cycles in elastic and elastic-perfectly-plastic conditions, along *x* direction: (a) $K_E = 2.09 \times 10^{-8}$ MPa^{-1} and (b) $K_E = 4.04 \times 10^{-8}$ MPa^{-1}

At the end, the wear scar including plastic deformation is displayed in Figure 5-7. The shape of wear scars in both material cases are the same as 'U', but the plastic deformation brings more scar depth and width. Again, the wear coefficient in elastic condition plays a more important role on the wear depth than in the plastic case. It should be mentioned that the wear scar displayed in the plastic case is much larger than the elastic case. In this case, the wear coefficient calculated by plastic deformed wear volume would be much higher than the real case.

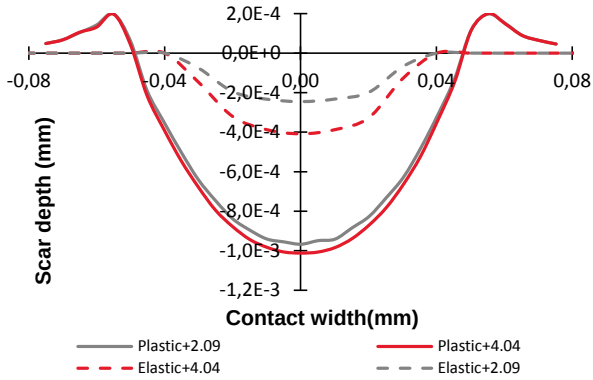

Figure 5-7. Wear scars after 1,000 cycles in elastic and elastic-perfectly-plastic conditions, along *x* direction

5.5 Concluding remarks

In this chapter, the application of fretting wear simulations on fretted wires is presented. To validate the fretting wear model, and investigate the influence of the material behaviour, the fretting wear model of wires crossed in right angle is constructed. The present study shows that:

1. For the fretting wear model with elastic behaviour, the contact pressure and contact radius are in good agreement with the Hertzian analytical solution. The wear depth of 13,000 cycles simulated is in the range of experimental results. However, the shape of fretting loop is a quasi-rectangular shape, which means that gross sliding happens rather than the partial slip reported in the experiments, though these FEA results are in accordance with analytical solution.
2. Given to plastic deformation, the fretting loop also presents gross sliding characteristic, but with higher dissipated energy. Meanwhile, the maximum wear depth distribution is a circle in the plastic model instead of one point in the elastic one. In this chapter, wear scar of only 1,000 cycles is simulated and the future work will be the FE modelling of the whole period of fretting wear in plastic condition.

Chapter 6

Conclusions and recommendations

6.1 Conclusions

In this thesis, the FE models of fretting wear based on energy model have been developed to predict the evolution of wear scar and stress distribution during fretting wear. Five FE models stemmed from Hertzian contact configuration are presented for investigating different problems in FE fretting wear simulations:

1. The FE Hertzian line contact model is the elemental model to verify the FE results with Hertzian solution. This is the first step for simulating fretting wear.
2. The basic fretting wear model is the main tool for validating wear scar with experimental results, and predicting the changes of contact variables during fretting wear process. In addition, the fretting wear model considering variable CoF is implemented based on this model.
3. The FE model for singularity problem is created for the study of mesh size sensitivity considering various parameters, *i.e.* applied displacement amplitude, CoF and the number of cycles in fretting wear. Singularity signature is utilized to identify if stress singularity exists.
4. The FE model with a debris layer is for studying the effect of debris on fretting wear process. In this model, the thickness and the material property of the debris layer are considered. Furthermore, the time of importing the debris layer is also a parameter in this model.
5. Besides the FE fretting wear model in line contact configuration, the fretting wear model for fretted wires is also generated. In this model, the material behaviour of contact bodies in fretting wear is considered based on the experiment results.

Through the presented FE models and results, the following main conclusions can be made:

1. Results of FE contact model have good agreement with Hertzian contact solution in both line contact configuration and 3D crossed cylinder with right angle configuration.
2. FE fretting wear basic model could predict fretting wear process. Choosing variable CoF or not in fretting wear has little influence on the final wear scar under gross sliding condition. However, at the running-in stage, the contact variables: *i.e.* the wear depth, wear width and the peak contact pressure are less

than the results from constant CoF model. The difference between these results of variable CoF model and constant CoF model deceases with the number of cycles. However, the diversities exist between FE results and experimental results.

3. Based on simulation results of singularity study, three points could be concluded. Firstly, σ_{xx} is more sensitive to mesh size than shear stress. Even in gross sliding case, $|\sigma_{xx}|_{max}$ increases with reducing mesh size, while peak shear stress keeps constant. Secondly, there is no stress singularity neither in partial slip nor in gross sliding regime after one fourth of a fretting wear cycle at lower CoF. However, it exists at higher CoF situation in partial slip, in which case the contact interface is almost stick with each other. Furthermore, after 20000 fretting wear cycles, $|\sigma_{xx}|_{max}$ becomes less sensitive to mesh size than before fretting wear in gross sliding condition, due to the great evolution of contact surfaces. While for partial slip, $|\sigma_{xx}|_{max}$ of fine mesh is much different from the case of coarse mesh. Stress singularity exits in partial slip condition after 20000 cycles, which means that fretting wear plays an important role in stress singularity in partial slip. Results reveal that more attention should be paid to the mesh size at contact interface, when the fretting condition is under partial slip regime.

4. In the FE debris layer model, two contact surfaces are generated: cylinder/debris layer and debris layer/specimen contact surfaces. The Young's modulus of a given thickness debris layer has minor effects on the contact pressure distribution in these contact interfaces. In contrast, the thickness of the given material layer does have influences on the contact distribution of the contact surface between debris layer/specimen, where usually the fretting wear happens. By increasing the thickness of the debris layer, the maximum contact pressure reduces and the contact width increases. Comparing results from models with or without debris layer, the contact pressure distribution after certain fretting wear cycles changes significantly. The first change is that the location of the peak contact pressure moves to the debris layer edge because of the stress concentration. Besides, the contact width is also enlarged to the width of the debris layer comparing to the contact width without the debris layer. In addition, timing for importing debris layer to the fretting wear model is also a key factor for the contact pressure distribution. The attendance of the debris layer could change the shape and dimensions of wear scar greatly in the

running-in time. However, little difference could be found for the wear scar after 18000 cycles.

5. Based on FE results of fretted wires model, it is found that the material behaviour of contact bodies has influence on fretting wear calculation in FE models. The wear scar considering plastic deformation is much larger than the one of elastic deformation model.

Finally, these findings enhance the understanding of fretting wear simulation in both fretting couple related knowledge, such as CoF effects, debris layer effects and material behaviour effects, and also the numerical aspect, *i.e.* singularity problem in fretting wear simulation. However, there are still some limitations of the present work, which could be summarized as follows:

1. Only the wear damage of the specimen is considered.
2. Wear coefficients calculated are not accurate. For 2D model, the relative slip in the experiment between contact surfaces is measured from the points of first bodies, which are far from the contact surfaces. For 3D model, the model for wear coefficient calculation is based on the assumptions of no friction and elastic deformation. Both wear coefficients of 2D and 3D are not the local wear coefficients at the contact surface.
3. The high cycles of fretting wear in the debris layer model of line contact configuration and plastic deformation model in fretted wires are not considered.

6.2 Recommendations for future works

Fretting wear is a complex material damage due to micro relative slip occurring at the contact interfaces. Inevitably, several assumptions are made to simplify the practical problems and to accelerate the computing time in the FE calculations presented in this thesis. Therefore, many aspects should be considered for the future works. Relevant topics are discussed in the following points:

1. Singularity signature could be extended to 3D analysis of fretting wear. Applying the proposed singularity analysis to 3D FE wear models will help in identifying the location of stress singularity and hence adjusting mesh sizes. This would save a large amount of computational time.

2. Multiscale analysis could be used for simulation of fretting wear with debris.
3. Wear coefficient models could be improved.
4. Wire rope in reality creates many contact surfaces. Due to different materials, contact geometries and loading conditions, the global wire ropes model for fretting wear simulations should be developed.
5. Friction plays an important role in fretting wear calculation. However, Coulomb's friction law is not always observed during fretting wear experiments. Thus, other friction laws may also be considered in fretting wear FE model in future.

Reference

[1] Budinski KG. Guide to friction, wear and erosion testing: ASTM International; 2007.

[2] Neale MJ, Gee M. Chapter 2 - Industrial wear problems. A Guide to Wear Problems and Testing for Industry. Suffolk, UK: William Andrew Publishing; 2001. p. 3-III.

[3] ASTM International. Standard Terminology Relating to Wear and Erosion. West Conshohocken2013.

[4] Anandavel K, Prakash RV. Effect of three-dimensional loading on macroscopic fretting aspects of an aero-engine blade–disc dovetail interface. Tribology International. 2011;44:1544-55.

[5] Gallego L, Fulleringer B, Deyber S, Nélias D. Multiscale computation of fretting wear at the blade/disk interface. Tribology International. 2010;43:708-18.

[6] Miyoshi K, Lerch BA, Draper SL. Fretting wear of Ti-48Al-2Cr-2Nb. Tribology International. 2003;36:145-53.

[7] Fouvry S, Paulin C, Deyber S. Impact of contact size and complex gross–partial slip conditions on Ti–6Al–4V/Ti–6Al–4V fretting wear. Tribology International. 2009;42:461-74.

[8] Cruzado A, Urchegui MA, Gómez X. Finite element modeling and experimental validation of fretting wear scars in thin steel wires. Wear. 2012;289:26-38.

[9] Short TA. Electric power distribution handbook: CRC press; 2014.

[10] Azevedo CRF, Cescon T. Failure analysis of aluminum cable steel reinforced (ACSR) conductor of the transmission line crossing the Paraná River. Engineering Failure Analysis. 2002;9:645-64.

[11] Chen G, Wang X, Wang J, Liu J, Zhang T, Tang W. Damage investigation of the aged aluminium cable steel reinforced (ACSR) conductors in a high-voltage transmission line. Engineering Failure Analysis. 2012;19:13-21.

[12] Hannel S, Fouvry S, Kapsa P, Vincent L. The fretting sliding transition as a criterion for electrical contact performance. Wear. 2001;249:761-70.

[13] Fouvry S, Jedrzejczyk P, Chalandon P. Introduction of an exponential formulation to quantify the electrical endurance of micro-contacts enduring fretting wear: Application to Sn, Ag and Au coatings. Wear. 2011;271:1524-34.

[14] Li L, Fanslau E, Talke F. An experimental study of the dimple/gimbal interface in a hard disk drive. Microsystem Technologies. 2011;17:863-8.

[15] Raeymaekers B, Helm S, Brunner R, Fanslau EB, Talke FE. Investigation of fretting wear at the dimple/gimbal interface in a hard disk drive suspension. Wear. 2010;268:1347-53.

[16] M.D. SSL. What is Hip Replacement? A Review of Total Hip Arthroplasty. http://www.orthop.washington.edu/?q=patient-care/articles/hip/what-is-hip-replacement-a-review-of-total-hip-arthroplasty.html. Access date: 12/10. 2015.

[17] Mattei L, Di Puccio F, Piccigallo B, Ciulli E. Lubrication and wear modelling of artificial hip joints: A review. Tribology International. 2011;44:532-49.

[18] WANG Cheng-tao JZ-m, LIAO Guang-shan,MAO Yuan-qing, ZHAO Qing-hui, ZHU Zhen-an, WANG Jin-wu, YAO Tian-ping. Wear analysis and diagnostic reasoning on clinical failure of artificial hip joints. Journal of Medical Biomechanics. 2012;27:361-8.

[19] Woodhead M. Hip implant recalled. http://www.6minutes.com.au/news/latest-news/hip-implant-recalled. Access date: 12/10. 2015.

[20] Golden PJ, Naboulsi S. Hybrid contact stress analysis of a turbine engine blade to disk attachment. International Journal of Fatigue. 2012;42:296-303.

[21] English R, Ashkanfar A, Rothwell G. A computational approach to fretting wear prediction at the head–stem taper junction of total hip replacements. Wear. 2015;338–339:210-20.

[22] English R, Ashkanfar A, Rothwell G. The effect of different assembly loads on taper junction fretting wear in total hip replacements. Tribology International. 2016;95:199-210.

[23] Popov VL. CONTACT MECHANICS AND FRICTION: Springer-Verlag Berlin Heidelberg; 2010.

[24] Menezes P, Nosonovsky M, Ingole SP, Kailas SV, Lovell MR. Tribology for scientists and engineers: from basics to advanced concepts: Springer Science & Business Media; 2013.

[25] Johnson KL. Contact mechanics: Cambridge university press; 1987.

[26] Cattaneo C. Sul contatto di due corpi elastici: distribuzione locale degli sforzi. Rend Accad Naz Lincei. 1938;27:342-8.

[27] Mindlin R. Compliance of Elastic Bodies in Contact. Journal of Applied Mechanics. 1949;16.

[28] Ovcharenko A, Etsion I. Junction growth and energy dissipation at the very early stage of elastic-plastic spherical contact fretting. Journal of Tribology. 2009;131:031602.

[29] Etsion I. Revisiting the Cattaneo–Mindlin Concept of Interfacial Slip in Tangentially Loaded Compliant Bodies. Journal of Tribology. 2010;132:020801-.

[30] Zhu MH, Zhou ZR. On the mechanisms of various fretting wear modes. Tribology International. 2011;44:1378-88.

[31] Toth L. The investigation of the steady stage of steel fretting. Wear. 1972;20:277-86.

[32] Ohmae N, Tsukizoe T. The effect of slip amplitude on fretting. Wear. 1974;27:281-94.

[33] Vingsbo O, Söderberg S. On fretting maps. Wear. 1988;126:131-47.

[34] Fouvry S, Liskiewicz T, Kapsa P, Hannel S, Sauger E. An energy description of wear mechanisms and its applications to oscillating sliding contacts. Wear. 2003;255:287-98.

[35] Fouvry S, Kapsa P, Vincent L. Quantification of fretting damage. Wear. 1996;200:186-205.

[36] Chen GX, Zhou ZR. Study on transition between fretting and reciprocating sliding wear. Wear. 2001;250:665-72.

[37] Varenberg M, Etsion I, Halperin G. Slip Index: A New Unified Approach to Fretting. Tribology Letters. 2004;17:569-73.

[38] Varenberg M, Etsion I, Altus E. Theoretical substantiation of the slip index approach to fretting. Tribology Letters. 2005;19:263-4.

[39] Pearson SR, Shipway PH. Is the wear coefficient dependent upon slip amplitude in fretting? Vingsbo and Söderberg revisited. Wear. 2015;330–331:93-102.

[40] Braunovic M. Fretting in electrical/electronic connections: a review. IEICE transactions on electronics. 2009;92:982-91.

[41] Waterhouse RB. Fretting corrosion: Pergamon Press; 1972.

[42] Li J, Lu YH. Effects of displacement amplitude on fretting wear behaviors and mechanism of Inconel 600 alloy. Wear. 2013;304:223-30.

[43] Sam Naboulsi JC. FRETTING FATIGUE INVESTIGATION OF DOVETAIL. http://www.gruppofrattura.it/ocs/index.php/ICF/ICF11/paper/viewFile/10391/9754. Access date: 03.19. 2016.

[44] International A. Standard Practice for Fretting Corrosion Testing of Modular Implant Interfaces: Hip Femoral Head-Bore and Cone Taper Interface. West Conshohocken2014.

[45] Santos CTd, Barbosa C, Monteiro MdJ, Abud IdC, Caminha IMV, Roesler CRdM. Fretting corrosion tests on orthopedic plates and screws made of ASTM F138 stainless steel. Research on Biomedical Engineering. 2015;31:169-75.

[46] Vincent L, Berthier Y, Dubourg MC, Godet M. Mechanics and materials in fretting. Wear. 1992;153:135-48.

[47] Stachowiak GW. Wear: materials, mechanisms and practice: John Wiley & Sons; 2006.

[48] Hurricks PL. The mechanism of fretting — A review. Wear. 1970;15:389-409.

[49] Colombié C, Vincent L, Godet M, Berthier Y, Floquet A. Fretting: Load Carrying Capacity of Wear Debris. Journal of Tribology. 1984;106:194-201.

[50] P. Suh N. The delamination theory of wear. Wear. 1973;25:111-24.

[51] Varenberg M, Halperin G, Etsion I. Different aspects of the role of wear debris in fretting wear. Wear. 2002;252:902-10.

[52] Lemm JD, Warmuth AR, Pearson SR, Shipway PH. The influence of surface hardness on the fretting wear of steel pairs—Its role in debris retention in the contact. Tribology International. 2015;81:258-66.

[53] Elleuch K, Fouvry S. Wear analysis of A357 aluminium alloy under fretting. Wear. 2002;253:662-72.

[54] van Peteghem B, Fouvry S, Petit J. Effect of variable normal force and frequency on fretting wear response of Ti–6Al–4V contact. Wear. 2011;271:1535-42.

[55] Waterhouse R, Taylor D. Fretting debris and the delamination theory of wear. Wear. 1974;29:337-44.

[56] Suh NP, Sin H-C. The genesis of friction. Wear. 1981;69:91-114.

[57] Blau PJ. The significance and use of the friction coefficient. Tribology International. 2001;34:585-91.

[58] McColl IR, Ding J, Leen SB. Finite element simulation and experimental validation of fretting wear. Wear. 2004;256:1114-27.

[59] Shen Y, Zhang D, Duan J, Wang D. Fretting wear behaviors of steel wires under friction-increasing grease conditions. Tribology International. 2011;44:1511-7.

[60] Zhang DK, Ge SR, Qiang YH. Research on the fatigue and fracture behavior due to the fretting wear of steel wire in hoisting rope. Wear. 2003;255:1233-7.

[61] Diomidis N, Mischler S. Third body effects on friction and wear during fretting of steel contacts. Tribology International. 2011;44:1452-60.

[62] Meng HC, Ludema KC. Wear models and predictive equations: their form and content. Wear. 1995;181–183, Part 2:443-57.

[63] Archard JF. Contact and Rubbing of Flat Surfaces. Journal of Applied Physics. 1953;24:981.

[64] Archard J, Hirst W. The wear of metals under unlubricated conditions. Proceedings of the Royal Society of London A: Mathematical, Physical and Engineering Sciences: The Royal Society; 1956. p. 397-410.

[65] Hutchings IM. Tribology: friction and wear of engineering materials. 1992.

[66] Matveevsky RM. The Critical Temperature of Oil With Point and Line Contact Machines. Journal of Fluids Engineering. 1965;87:754-9.

[67] Fouvry S, Kapsa P. An energy description of hard coating wear mechanisms. Surface and Coatings technology. 2001;138:141-8.

[68] Sauger E, Fouvry S, Ponsonnet L, Kapsa P, Martin J, Vincent L. Tribologically transformed structure in fretting. Wear. 2000;245:39-52.

[69] Fouvry S, Kapsa P, Vincent L. An elastic–plastic shakedown analysis of fretting wear. Wear. 2001;247:41-54.

[70] Ding J. The effect of slip regime on fretting wear-induced stress evolution. International Journal of Fatigue. 2004;26:521-31.

[71] Paulin C, Fouvry S, Meunier C. Finite element modelling of fretting wear surface evolution: Application to a Ti–6A1–4V contact. Wear. 2008;264:26-36.

[72] Elleuch K, Fouvry S. Experimental and modelling aspects of abrasive wear of a A357 aluminium alloy under gross slip fretting conditions. Wear. 2005;258:40-9.

[73] Dick T, Cailletaud G. Fretting modelling with a crystal plasticity model of Ti6Al4V. Computational Materials Science. 2006;38:113-25.

[74] Dick T, Paulin C, Cailletaud G, Fouvry S. Experimental and numerical analysis of local and global plastic behaviour in fretting wear. Tribology international. 2006;39:1036-44.

[75] Mohd Tobi AL, Ding J, Bandak G, Leen SB, Shipway PH. A study on the interaction between fretting wear and cyclic plasticity for Ti–6Al–4V. Wear. 2009;267:270-82.

[76] Fouvry S, Paulin C, Liskiewicz T. Application of an energy wear approach to quantify fretting contact durability: Introduction of a wear energy capacity concept. Tribology International. 2007;40:1428-40.

[77] Mohd Tobi AL, Shipway PH, Leen SB. Gross slip fretting wear performance of a layered thin W-DLC coating: Damage mechanisms and life modelling. Wear. 2011;271:1572-84.

[78] Madge JJ, Leen SB, McColl IR, Shipway PH. Contact-evolution based prediction of fretting fatigue life: Effect of slip amplitude. Wear. 2007;262:1159-70.

[79] Madge JJ, Leen SB, Shipway PH. The critical role of fretting wear in the analysis of fretting fatigue. Wear. 2007;263:542-51.

[80] Zhang T, McHugh PE, Leen SB. Computational study on the effect of contact geometry on fretting behaviour. Wear. 2011;271:1462-80.

[81] Cheikh M, Quilici S, Cailletaud G. Presentation of KI-COF, a phenomenological model of variable friction in fretting contact. Wear. 2007;262:914-24.

[82] Liu J, Shen HM, Yang YR. Finite element implementation of a varied friction model applied to torsional fretting wear. Wear. 2014;314:220-7.

[83] Ding J, McColl IR, Leen SB, Shipway PH. A finite element based approach to simulating the effects of debris on fretting wear. Wear. 2007;263:481-91.

[84] Shipway PH, Williams EJ, Leen SB, Ding J. A multi-scale model for fretting wear with oxidation-debris effects. Proceedings of the Institution of Mechanical Engineers, Part J: Journal of Engineering Tribology. 2009;223:1019-31.

[85] Basseville S, Héripré E, Cailletaud G. Numerical simulation of the third body in fretting problems. Wear. 2011;270:876-87.

[86] Ghosh A, Wang W, Sadeghi F. An elastic–plastic investigation of third body effects on fretting contact in partial slip. International Journal of Solids and Structures. 2016;81:95-109.

[87] Leonard BD, Ghosh A, Sadeghi F, Shinde S, Mittelbach M. Third body modeling in fretting using the combined finite-discrete element method. International Journal of Solids and Structures. 2014;51:1375-89.

[88] Tang L, Ding S, Xie Y, Huo Y. A multilayer nodes update method in FEM simulation of large depth fretting wear. Wear. 2013;301:483-90.

[89] Carpinteri A, Paggi M. Asymptotic analysis in Linear Elasticity: From the pioneering studies by Wieghardt and Irwin until today. Engineering Fracture Mechanics. 2009;76:1771-84.

[90] Sinclair GB. Stress singularities in classical elasticity—II: Asymptotic identification. Applied Mechanics Reviews. 2004;57:385.

[91] Hills DA, Dini D, Magadu A, Korsunsky AM. A review of asymptotic procedures in stress analysis: Known solutions and their applications. The Journal of Strain Analysis for Engineering Design. 2004;39:553-68.

[92] Sinclair GB, Chi X, Shih TIP. On the pressure and stress singularities induced by steady flows of incompressible viscous fluids. Acta Mech Sin. 2009;25:451-62.

[93] Hills DA, Thaitirarot A, Barber JR, Dini D. Correlation of fretting fatigue experimental results using an asymptotic approach. International Journal of Fatigue. 2012;43:62-75.

[94] Shen Y, Zhang D, Ge S. Effect of fretting amplitudes on fretting wear behavior of steel wires in coal mines. Mining Science and Technology (China). 2010;20:803-8.

[95] Zhang DK, Shen Y, Xu LM, Ge SR. Fretting wear behaviors of steel wires in coal mine under different corrosive mediums. Wear. 2011;271:866-74.

[96] Cruzado A, Leen SB, Urchegui MA, Gómez X. Finite element simulation of fretting wear and fatigue in thin steel wires. International Journal of Fatigue. 2013;55:7-21.

[97] Cruzado A, Urchegui MA, Gómez X. Finite element modeling of fretting wear scars in the thin steel wires: Application in crossed cylinder arrangements. Wear. 2014;318:98-105.

[98] Wang D, Zhang D, Wang S, Ge S. Finite element analysis of hoisting rope and fretting wear evolution and fatigue life estimation of steel wires. Engineering Failure Analysis. 2013;27:173-93.

[99] Giannakopoulos AE, Suresh S. A three-dimensional analysis of fretting fatigue. Acta Materialia. 1998;46:177-92.

[100] Argatov II, Gómez X, Tato W, Urchegui MA. Wear evolution in a stranded rope under cyclic bending: Implications to fatigue life estimation. Wear. 2011;271:2857-67.

[101] Soh HP. Fretting wear studies of aeroengine materials: University of Nottingham; 2006.

[102] Fouvry S, Duó P, Perruchaut P. A quantitative approach of Ti–6Al–4V fretting damage: friction, wear and crack nucleation. Wear. 2004;257:916-29.

[103] Paulin C, Fouvry S, Deyber S. Wear kinetics of Ti–6Al–4V under constant and variable fretting sliding conditions. Wear. 2005;259:292-9.

[104] ABAQUS. 6.11. User's manual. Inc and Dassault systemes. 2011.

[105] Sinclair G, Beisheim J, Sezer S. Practical convergence-divergence checks for stresses from FEA. Proceedings of the 2006 International ANSYS Conference2006.

[106] Comninou M. Stress singularity at a sharp edge in contact problems with friction. Journal of Applied Mathematics and Physics (ZAMP). 1976;27:493-9.

[107] Xushou Z, Chuenhe Z, Chailu Z. Slip amplitude effects and microstructural characteristics of surface layers in fretting wear of carbon steel. Wear. 1989;134:297-309.

[108] Warmuth AR, Pearson SR, Shipway PH, Sun W. The effect of contact geometry on fretting wear rates and mechanisms for a high strengthsteel. Wear. 2013;301:491-500.

[109] Goryacheva IG, Rajeev PT, Farris TN. Wear in Partial Slip Contact. Journal of Tribology. 2000;123:848-56.

[110] Ghosh A, Leonard B, Sadeghi F. A stress based damage mechanics model to simulate fretting wear of Hertzian line contact in partial slip. Wear. 2013;307:87-99.

[111] Urchegui MA, Tato W, Gómez X. Wear Evolution in a Stranded Rope Subjected to Cyclic Bending. Journal of Materials Engineering and Performance. 2008;17:550-60.

[112] Wang D, Magd Abdel Wahab, LL Wang, XW Li, ZC Zhu, DK Zhang, and XB Mao. Finite element analysis of fretting fatigue of fretted wires. In: Wahab MA, editor. 4th International Conference on Fracture Fatigue and Wear. Ghent2015. p. 135-42.

[113] Yue T, Abdel Wahab M. Finite element analysis of stress singularity in partial slip and gross sliding regimes in fretting wear. Wear. 2014;321:53-63.

[114] Cumming G, Fidler F, Vaux DL. Error bars in experimental biology. The Journal of Cell Biology. 2007;177:7-11.

[115] Zhou Z, Fayeulle S, Vincent L. Cracking behaviour of various aluminium alloys during fretting wear. Wear. 1992;155:317-30.

List of publications

A1 - Peer reviewed journal publications included in Science Citation Index

1. **Yue T,** Abdel Wahab M. A Numerical Study on the Effect of Debris Layer on Fretting Wear. Materials. 2016;9:597.

2. **Yue T**, Abdel Wahab M. Finite element analysis of stress singularity in partial slip and gross sliding regimes in fretting wear. Wear. 2014;321:53-63.

3. **Yue T**, Abdel Wahab M. On the effect of variable coefficient of friction on fretting wear under different contact regimes, submitted to Tribology Letters

4. Ferjaoui A, **Yue T**, Abdel Wahab M, Hojjati-Talemi R. Prediction of fretting fatigue crack initiation in double lap bolted joint using Continuum Damage Mechanics. International Journal of Fatigue. 2015;73:66-76.

5. Resende Pereira K. **Yue T**, M. A. Wahab. Multiscale analysis of the effect of roughness on fretting wear, under preparation.

C1: Articles published in proceedings of scientific conferences

1. **Yue T**, Abdel Wahab M. Elastoplastic fretting wear behaviour of contact wires. International Journal of Fracture Fatigue and Wear, Proceedings. 2016. p. 50-57.

2. **Yue T**, Abdel Wahab M. Finite element simulations of the effect of friction coefficient in fretting wear. International Journal of Fracture Fatigue and Wear, Proceedings. 2016. p. 58-63.

3. **Yue T**, Abdel Wahab M. Debris models used for wear simulations. International Journal of Fracture Fatigue and Wear, Proceedings. 2015. p. 227–32
4. **Yue T**, Abdel Wahab M, Hojjati Talemi R, Sadeghi M. Numerical modeling of fretting wear. SUSTAINABLE CONSTRUCTION AND DESIGN. 2013
5. Resende Pereira K de F, **Yue T**, Abdel Wahab M. Multiscale modelling of roughness effect in fretting wear. International Journal of Fracture Fatigue and Wear, Proceedings. 2015. p. 272–8.

6. Hojjati Talemi R, Abdel Wahab M, **Yue T**, D'Alvise L. On fretting fatigue behaviour of single bolted lap joint. International journal of fracture fatigue and wear. Laboratory Soete – Ghent University; 2014. p. 269–74
7. Sadeghi M, Abdel Wahab M, Hojjati Talemi R, **Yue T**. A review of FE on crack initiation in fretting fatigue. SUSTAINABLE CONSTRUCTION & DESIGN. 2013